REPUBLIQUE DU CAMEROUN
Paix-Travail-Patrie
****
UNIVERSITE DE YAOUNDE I
****
CENTRE DE RECHERCHE ET DE FORMATION DOCTORALE EN SCIENCES, TECHNOLOGIES ET GEOSCIENCES
****
UNITE DE RECHERCHE ET DE FORMATION DOCTORALE EN PHYSIQUES ET APPLICATIONS
****
B.P 812 Yaoundé
Email: crfd_stg@uy1.un inet.cm

REPUBLIC OF CAMEROON
Peace-Work-Fatherland
****
THE UNIVERSITY OF YAOUNDE I
****
POSTGRADUATE SCHOOL OF SCIENCES, TECHNOLOGY AND GEOSCIENCES
****
RESEARCH AND POSTGRADUATE TRAINING UNIT FOR PHYSICS AND APPLICATIONS
****
P.O. Box 812 Yaoundé
Email: crfd_stg@uy1.uninet.cm

FACULTY OF SCIENCE
FACULTE DES SCIENCES
DEPARTMENT OF PHYSICS
DEPARTEMENT DE PHYSIQUE

Laboratoire de Mécanique, Matériaux et Structure
Laboratory of Mechanics, Materials and Structure

THEORETICAL AND EXPERIMENTAL STUDY OF THE DYNAMICS OF OPTOELECTRONIC OSCILLATORS WITH A CUBIC NONLINEAR ELECTRICAL COMPONENT.

Thesis submitted and defended for the award of the degree of Doctor of Philosophy (Ph.D.) in Physics,

***Option**: Fundamental mechanics and complex systems*

By
DEUMI KAMAHA Juliette Stévia
Master of Science in Physics
Registration Number : **10W0125**
Under the supervision of
WOAFO Paul
Professor, University of Yaounde I (Cameroon)

Academic year 2023 / 2024

UNIVERSITÉ DE YAOUNDÉ
THE UNIVERSITY OF YAOUNDE I

FACULTÉ DES SCIENCES
FACULTY OF SCIENCES

DÉPARTEMENT DE PHYSIQUE
DEPARTMENT OF PHYSICS

ATTESTATION DE CORRECTION DE LA THÈSE DE DOCTORAT/Ph.D

Nous, Professeur **BODO Bertrand** et Professeur **ESSIMBI ZOBO Bernard**, respectivement Examinateur et Président du jury de la Thèse de Doctorat/PhD de Madame **DEUMI KAMAHA Juliette Stévia**, Matricule **10W0125**, préparée sous la direction du Professeur **WOAFO Paul** (Université de Yaoundé 1) intitulée : « **Theoretical and experimental study of the dynamics of optoelectronic oscillators with a cubic nonlinear electrical component**», soutenue le Mercredi, **17 Janvier 2024**, en vue de l'obtention du grade de Docteur/PhD en Physique, Spécialité **Mécanique, Matériaux et Structures,** option **Mécanique Fondamentale et Systèmes Complexes** attestons que toutes les corrections demandées par le jury de soutenance ont été effectuées.

En foi de quoi, la présente attestation lui est délivrée pour servir et valoir ce que de droit.

Fait à Yaoundé, le 15 FEV 2024

Examinateur	Le Président du jury	Le Chef de Département de Physique
Pr BODO Bertrand	Pr ESSIMBI ZOBO Bernard	Pr NDJAKA Jean-Marie

THEORETICAL AND EXPERIMENTAL STUDY OF THE DYNAMICS OF OPTOELECTRONIC OSCILLATORS WITH A CUBIC NONLINEAR ELECTRICAL COMPONENT.

Thesis Submitted and defended for the award of Doctorat/ PhD in Physics

Speciality: Mechanics, Materials and Structures

By

DEUMI KAMAHA Juliette Stévia

MASTER in Physics

Registration Number: 10W0125

Under the supervision of

WOAFO Paul

Professor

University of Yaoundé 1

Year 2024

Dedications

*... To the **Almighty God**, he without whom this work would not be finished if he had not granted me health.*

*...To my father **Mr. KAMAHA Prospère**, who has always taught me perseverance, endurance and the joy of a job well done.*

*... To my mother **Mrs. NITCHEU Victorine**, who has always provided me with the care and supervision necessary to be emotionally balanced for the completion of this work.*

*... To my son **NGAKE KAMAHA Godwill**, who illuminated my life, giving me the strength to hold out until the end.*

Acknowledgements

The doctorate is a scientific and human adventure rich in emotions. It includes moments of joy, excitement, but also moments of hesitation and doubt. This research work carried out during these three years at the Laboratory of Modelling and Simulation in Engineering, Biomimetics and Prototypes (LAMSEBP) of the University of YaoundÃĭ 1, was possible thanks to exceptional personalities. These personalities who marked my career, providing the necessary impetus to pursue my studies. Now my PhD is coming to an end, and it is time for me to express my thanks to the coaches, colleagues, friends and family members who allowed me to move forward.

✠ I would like to express here my gratitude and profound thankfulness to my PhD supervisor, Professor **Paul Woafo** who held me during these three years of thesis. Professor, from my works of Master up to now, you have grown in me good qualities (humanistic and scientific) which, I hope, will make me a great woman. Beyond the qualities of supervisor that you hold, you have been like a father to me. I cannot describe just in a few lines all the good that I think of you, but know that it was a pleasure to work with you. Thanks once more.

✠ My sincere thanks are intended for the **jury members** for having accept to evaluate my work.

✠ I am also grateful to Professor **Talla Mbé Jimmi Hervé** who has always been available to me. I could not have asked for better assistance, always available, always motivated, always good advice and unparalleled patience. Professor, find here the expression of my perfect gratitude for your advice, the scientific discussions granted to this work. Thank you very much.

✠ I am also grateful to **LAMSEBP** and the Laboratory of Mechanics, Materials and Structures, Laboratories where I did my thesis works.

✠ I want to thank the **Humboldt-Allemagne** foundation for electronic equipment as part of a research project and funded by this foundation up to 20000 euros.

✠ I want to thank **FEMTO-ST Besancon (France)**institute for the optical equipment without which this thesis work would not have been possible.

✠ I would like that the associations such as **The Institute of Electrical and Electronics Engineers** (**IEEE**), **The Optical Society of America** (**OSA**) **Yaoundé 1 Student Chapter**, **The international society for optics and photonic** (**SPIE**)

Cameroon Student Chapter find here all my gratitude, for the experimental materials, the training, the comfort and entertainment tools that they have put in the LAMSEBP,thus helping to progress quickly in our thesis works.

✠ To **The Cameroon Physical Society** (CPS), I express my thanks for having organized on several occasions scientific conferences in which I participated.

✠ My genuine and sincere thanks to the training institute **Sci-Tech-Services Cameroon** directed by Professor Paul Woafo, for opening us its doors so that we can get training in 3D printing and many others. May the Almighty God continue to bless you, Professor, so that many young people and students can enjoy and benefit from your services.

✠ I thank Professor **Ndjaka Jean Marie**, Head of Physics Department of the Faculty of Sciences of the University of Yaoundé 1, for his simplicity and his ability to always react to the problems we ask him.

✠ I thank Professor **Kofané Timoléon Crépin**, previously Head of Department of Physics, for the enlightening teachings and advice he gave me since the Bachelor degree cycle. May this work show my gratitude to you.

✠ I extend my thanks to Professor **Nana Nbendjo Blaise Roméo** for his teaching, encouragement during difficult times and the supervision during my master.

✠ My gratitude here is expressed to all the teachers of the Physics Department of the University of Yaoundé 1, for the teachings received during my academic training.

✠ I express my gratitude to Doctors **Simo Domguia Ulrich**, **Thépi Siéwé Raoul**, for the scientific discussions you gave me each time I came to you.

✠ I would particularly like to express my gratitude to **Dr. Youmbi Dorota** for her availability during my years in PhD, the friendly atmosphere she has always put on the team, and for the many exchanges we have always had.

✠ My gratitude is addressed to the elders of the laboratory. I am thinking of: Doctor **Talla Alain Francis**, Doctor **Nwagoum Tuwa Péguy**, Doctor **Metsebo Jules**, Doctor **Ndemanou Péguy**, **Mr. Chamgoué Chéagé André**, **Mr. Dongmo Eric**, **Mr. Anagué Léonel**, **Mr. Mba Stève**, for their assistance and advice.

✠ To all the PhD students of the LAMSEBP and the Laboratory of Mechanics, Materials and Structures for the edifying exchanges that we had and which allowed me to carry out this work, I thank you and wish you good luck for the future.

✠ I express my thanks to **Mr. Engwé Pierre Roger**, my fiance, for never having hesitated to provide me with his multifaceted help.

✠ To my best friends, you who have always been with me from high school to now, you have always been able to give me encouraging words so that I can finish this work. I am thinking here of: **Mr. Mbarga Nwaha Emmanuel**, **Mrs. NGATCHA Nelly**, **Mr. Kouatcha Mebina Cédric**, **Mrs. Mapa Kamdem Alida**, **Mr. Naha Naha Henri Joél**.

✠ I express my thanks to my friends of University of Dschang **Mr. Liédji**, **Mr.**

Marlone, **Mr. Miemdjim Willy**, **Mrs. Chia**, for never having hesitated to provide me with their multifaceted help.

✠ I express my thanks to **Rev. Fetsine Ghislain**, for the advice you have never stopped giving me, your team spirit. You have always been able to respond, whenever I asked for your help.

✠ I express my thanks to **Mr. Nzali Fammoe Franklin**, **Mrs. Houmkoua Uguette Eveline**, **Mrs. Djampa Noelle**, **Mr. Ngui Marcel Kiki**, **Mr. Effa Guy Parfait Junior**, **Mr. and Mrs. Giogue Tafeukeng**, **Mrs. Petnkeu Simo Inès Michelle** for the encouragement you have never stopped giving me.

✠ These three years have been an adventure for me. I would like to express special thanks to my parents, those also whose names were not mentioned, for their support.

✠ There are a lot of them and they will certainly recognize themselves, the ones who have contributed directly or indirectly for the achievement of this work. I would like to express my gratitude to them.

Contents

Dedications i

Acknowledgements ii

List of Figures xiii

List of Tables xiv

List of Abbreviations xv

Abstract xvi

Résumé xviii

GENERAL INTRODUCTION 1

1 Literature Review 5

1.1 Introduction 6

1.2 Optoelectronic oscillators (OEOs) and its characterization by Normal Form Method. 6

1.2.1 Basic principles of a standard optoelectronic oscillator. 6

1.2.2 Characterization of the bandpass OEO near the primary Hopf bifurcation by the normal form method. 8

1.3 The main applications of Optoelectronic oscillators. 10

1.3.1 OEO-based Chaos Synchronization and Communications. 10

1.3.2 OEO-based Reservoir Computing 12

1.3.3 Narrow-band OEOs for ultrapure microwave generation. 13

1.3.4 Optoelectronic oscillators for measurement. 14

1.3.5 Optoelectronic oscillators as an Acoustic Sensor. 17

1.4 OEOs with nonlinear filter. 18

1.4.1 OEOs with nonlinear filter. 18

1.4.2 OEO with a Colpitts oscillator. 22

1.5 OEOs which use a laser diode for electrical-to-optical conversion. 24

1.5.1 OEO with direct feedback modulation. 24
1.5.2 OEO with modulation through a Van der Pol electrical component. 27
1.6 Problem statement of the work. 30
1.7 Conclusion. 31

2 Methodology **32**
2.1 Introduction 33
2.2 Mathematical formalisms and stability criteria 33
2.2.1 Stability analysis for ordinary differential equations and delay differential equations 33
2.2.2 Characterization by the normal form of integro-differential equations with delay 34
2.2.3 Intensity modulation by using the laser diode in an OEO: the limit of the low pumps of the laser diode 37
2.3 Numerical methods 38
2.3.1 Runge-Kutta Methods 38
2.3.2 Bisection method for solving nonlinear algebraic equations 40
2.4 Presentation of the experimental device 41
2.4.1 Cubic-nonlinear band-pass filter (CNBPF) 42
2.4.2 Stabilized DC power supply and Rigol oscilloscope. 45
2.4.3 Laser diode. 46
2.4.4 Polarization controller 46
2.4.5 Electro-optical modulator. 47
2.4.6 The optical fiber 48
2.4.7 Photodiode 49
2.5 Conclusion 50

3 Results and discussion **51**
3.1 Introduction 52
3.2 Dynamics of an OEO which use the CNBPF 52
3.2.1 Model description and time-delayed model to investigate the complex dynamical behavior 52
3.2.2 Numerical and experimental simulations to approximate the dynamics of CN-OEO 57
3.3 Characterization in term of keys parameters of the system of the CN-OEO 61
3.3.1 Stability analysis of fixed points in term of keys parameters 62
3.3.2 Bifurcation analysis of the CN-OEO: Route to chaos 62
3.3.3 Characterization of limit-cycle oscillation by using the Normal form 65
3.3.4 Effect of the cubic-nonlinear term on oscillation condition of the system. 71

3.4 The simplified benchmark of the CN-OEO 73
3.4.1 System and model of the simplified CN-OEO 73
3.4.2 Stability analysis of the simplified CN-OEO 77
3.4.3 Nonlinear dynamics of the simplified CN-OEO 79

GENERAL CONCLUSION **1**

Bibliography **3**

List of Publications **13**

List of Figures

1.1 Experimental setup of the OEO. PC, polarization controller; MZM, MachZehnder modulator; DL, delay line; PD, photodiode; Amp, RF amplification; MC, microwave coupler [12]. 7

1.2 Time traces of the variable x for different values of the feedback gain β of standard optoelectronic oscillator. $\phi = \frac{-\pi}{4}$ (a) $\beta = 1.5$, (b) $\beta = 2$, (c) $\beta = 3$, and (d) $\beta = 3.5$ [21]. 8

1.3 (a) Variation of the limit-cycle amplitude in case of negative slope with $\phi = \frac{-\pi}{4}$, case of positive slope with $\phi = \frac{\pi}{4}$) as the gain is varied beyond the Hopf bifurcation point γ_H as $\delta \equiv \gamma - \gamma_H$. (b) is the evolution of limit-cycle frequency in case of $\delta = -4 \times 10^2$, and $\delta = 1.5 \times 10^2$ as a function of the normalized delay $\nu = \frac{T_D}{\tau}$. Both in (a) and (c), the analytical result is displayed with a solid line and the numerical with the black circles [12]. . 10

1.4 Field experiment of chaos communication using an Ikeda-based optoelectronic oscillator. (a) Emitter-receiver system. The emitter uses a laser diode (LD), MachZehnder modulator (MZ), an erbium-doped fiber amplifier (EDFA) to boosts the power of the signal to be launched into the transmission line [86]. 11

1.5 The optoelectronic using Synchronization for prediction of high-dimensional chaotic dynamics [87]. 12

1.6 Schematic of an experimental OEO reservoir computer. The reservoir layer is a delay dynamical system in which a Mach-Zehnder (MZM) modulator acts as nonlinearity. The information is mixed to the signal using an arbitrary waveform generator (AWG) [89]. 13

1.7 Basic single-loop OEO architecture for ultrapure microwave generation [90]. 14

1.8 Schematic of the proposed OEO-based temperature sensor with injection locking. PC, polarization controller; DEMZM, dual electrode Mach-Zenhder modulator; SMF, single mode fiber; PD, photodetector; BPF, bandpass filter; EA, electrical amplifier; LO, local oscillator; ADC, analog-to-digital converter [104]. 14

1.9 Classical structure of an opto-electronic oscillator for refractive index measurement [93]. 15
1.10 Configuration of the proposed wideband-tunable OEO for angular velocity measurement (red lines: optical fibers and blue lines: coaxial cables) [92]. . 16
1.11 A schematic diagram of the OEO-based acoustic sensor experiment [94]. . . 17
1.12 Experimental setup to explore the dynamics in multinonlinear electrooptical systems with delayed feedback. (note that bandpass filter stands here for all the bandpass filtering elements of the electric branch) Vdp is Van der pol, OC is Offest Controller [20]. 18
1.13 Birth and evolution of breathers in the time domain for $T_D = 0$, as the laser pump current (I) is increased beyond threshold I_{th}. (a) $I \simeq I_{th} = 27.3mA$, (b) $I = 1.23I_{th}$ (c) $I = 1.49I_{th}$ (d)$I = 1.72I_{th}$ [20]. 19
1.14 Evolution and death of breathers and pulse-package oscillations in the time domain as the laser pump current is increased far above the threshold. (a) $I = 1.81I_{th}$, (b) $I = 2.27I_{th}$ (c) $I = 2.77I_{th}$ (d) $I = 2.93I_{th}$ [20]. 20
1.15 Evolution and death of breathers and pulse-package oscillations in the phase space as the laser pump current is increased far above the threshold ($T_D = 0$). Theses figures correspond to the time traces displayed Fig. 1.14. (a) $I = 1.81I_{th}$, (b) $I = 2.27I_{th}$ (c) $I = 2.77I_{th}$ (d) $I = 2.93I_{th}$ [20]. 20
1.16 Breathers, pulse-package oscillations, and fully developed hyperchaos as the laser pump current is increased far above the threshold in the presence of delay ($T = 0.5\mu s$). (a) $I = 1.28I_{th}$, (b) $I = 1.64I_{th}$ (c) $I = 2.46I_{th}$ (d) $I = 3.34I_{th}$ [20]. 21
1.17 Evidence of the three-timescale behavior of the system in the pulse-package regime. (Left) pulse packages for the system without delay and with $I = 2.27I_{th}$ [see Figure 1.14(b)]. The fastest oscillations are periodic. (Right) pulse packages with delay and with $I = 2.46I_{th}$ [see Figure 1.16(c)]. The fastest oscillations are periodic [20]. 21
1.18 Experimental set-up of the OEO-Colpitts oscillator. MC= microwave coupler [58]. 22
1.19 A picture of the Colpitts circuit in the laboratory [58]. 22
1.20 Multiperiodic, (b) chaotic bursting, (c) periodic bursting, and (d) pulsepackage oscillation in the time domain as the polarization voltage is increased beyond the threshold ($T_D = 0$) (a) $V_{pol} = 1.29V_{th}$; (b) $V_{pol} = 1.34V_{th}$; (c) $V_{pol} = 1.4V_{th}$; (d) $V_{pol} = 1.6V_{th}$ [58]. 23
1.21 (a) Multi-periodic, (b) slow-fast dynamics, and (d) chaotic bursting oscillation in the time domain as the polarization voltage is increased beyond the threshold ($T_D = 0.2\mu s$). (a) $V_{pol} = 1.09V_{th}$; (b) $V_{pol} = 1.24V_{th}$; (d) $V_{pol} = 1.54V_{th}$; (c) is the enlargement of one package of (b) [58]. 24

1.22 Experimental setup of direct modulation of the OEO. LD: laser diode, PD: photodiode, BPF: band pass filter, G: voltage variable attenuator [66]. . . . 25
1.23 Numerical bifurcation diagram of the simplest OEO where the variable x, is plot as the gain β is increased [66]. 26
1.24 Experimental (left column) and numerical (right column) timetraces of the simplest OEO. $\vartheta = -0.5$, $\beta = 1.29$, $\beta = 1.37$, $\beta = 1.6$ [66]. 26
1.25 (a) The experimental setup of Van der Pol-optoelectronic oscillator and (b) experimental setup of the Van der Pol oscillator [57]. 27
1.26 Experimental (left column) $V_{th} - V_{pol} = 1.314V$, $R = 10k\Omega$, $C = 10nF$, $T_D = 0.21\mu s$ and numerical (right column) timetraces of the simplest OEO. $\alpha = 0.1$, d for $\beta = 1.2$, e for $\beta = 2.2$, f for $\beta = 2.2$ [57]. 28
1.27 (a) Numerical bifurcation diagram of the simplified OEO where the variable x (maxima), (b) Lyapunov exponent of the system for $T_D = 4$ and $\vartheta = 0.1$. The label (a)-(f) indicate the dynamical regimes corresponding to the phase portraits of the Fig. 1.28. 29
1.28 Numerical simulations of the dimensionless VdP-OEO for $T_D = 4$ and $\vartheta = 0.1$, for various gain values β in the space. (a) $\beta = 0.2$: quasi-sinusoidal oscillations with low amplitude. (b) $\beta = 0.405$: quasi-sinusoidal oscillations with high amplitude. (c) $\beta = 1.01$: Non-sinusoidal oscillations with high amplitude. (d) $\beta = 1.4$ period-two oscillations. (e) $\beta = 1.55$: period-four oscillations. (f) $\beta = 1.7$: chaos. 30

2.1 Experimental setup of direct modulation of the OEO. LD: laser diode, PD: photodiode, BPF: band pass filter, G: voltage variable attenuato [66]. . . . 37
2.2 (a) Experimental setup of cubic-nonlinear optoelectronic oscillator. (b) Inner structure of the nonlinear capacitor [68, 69]. PC: Polarization Controller; MZM: MachZehnder Modulator; V_B is the offset phase control voltage; PD: Photodiode; CNBPF: Cubic-Nonlinear Band-Pass Filter; VS: Voltage Subtractor; Amp: RF amplifier; MC: Microwave Coupler.$L = 0.1\,m$H, $r = 300\,\Omega$, $C_1 = 270\,p$F, $C_2 = 9.15\,n$F 41
2.3 Experimental devices in the laboratory. One can identify different components cited in the text. 42
2.4 Operational amplifier LF356N. 42
2.5 Electronic diagram of an OPAMP. 43
2.6 Some basic operations using OPAMP: (a) integrator; (b) inverter amplifier; (c) summator; (d) subtractor. 43
2.7 (a) Resistors and (b) Capacitors. 44
2.8 (a) Coils and (b) diodes. 45
2.9 Some additional materials used: (a) DC power supply; (b) Rigol oscilloscope. 45

2.10 Distributed feedback laser diode 46
2.11 The current-power characteristics of the laser. 46
2.12 Polarization controller. 47
2.13 (a) Electro-optical modulator integrating phase modulation, (b) MachZehnder image. 48
2.14 The structure of the optical fiber 48
2.15 Optical fibers used to constitute CN-OEO. 49
2.16 Optical fibers used to constitute CN-OEO. 50

3.1 Experimental setup of cubic-nonlinear optoelectronic oscillator [**?**]. (b) inner structure of the nonlinear capacitor [68, 69]. PC: Polarization Controller; MZM: Mach-Zehnder Modulator; V_{B} is the offset phase control voltage; PD: Photodiode; CNBPF: Cubic-Nonlinear Band-Pass Filter; VS: Voltage Subtractor; Amp: RF amplifier; MC: Microwave Coupler. $L = 0.1\,m\mathrm{H}$, $r = 300\,\Omega$, $C_1 = 270\,p\mathrm{F}$, $C_2 = 9.15\,n\mathrm{F}$. 53
3.2 Experimental devices in the laboratory. One can identify different component cited in the text. 54
3.3 (Color online) (a) Bifurcation diagram depicting the Hopf bifurcation routes to chaos. (b) Largest Lyapunov exponent Λ. 57
3.4 (Color online) Projections in the (x–y) plane of the trajectories (solid red (or black)) of: (a) the standard OEO (i.e. without cubic-term in equation. (3.9)) and (b) the cubic-nonlinear OEO. The time trace of Figure 3.4 (b) is given in Figure 3.6 (d). The dashed and solid greys are the instable and stable branches of the invariant critical manifold, respectively. The invariant critical manifolds are plotted for $\sigma \to 0$ [12]. In both figures, $|\gamma| = 1.9$ and $\phi = -\pi/4$. 59
3.5 (Color online) Timetraces of the amplitude of the cubic-nonlinear OEO (blue or black) versus the standard OEO (grey). $|\gamma| = 1.01$ and $\phi = -\pi/4$. A noticeable effect of the nonlinearity is to increase the frequency of the limit-cycle induced by the primary Hopf bifurcation.. 60
3.6 (Color online) Experimental and numerical timetraces demonstrating the dynamical evolutions of the system as the gain increases. $\phi = -\pi/4$. From top to bottom: - for experimental curves, P_{in} is progressively 6.51 mW, 7 mW, and 7.8 mW; - for the numerical ones, β is equal to 1.1, 1.9, and 3. 61
3.7 (a) A point-by-point recorded of the experimental bifurcation diagram. (b) the numerical bifurcation diagram and (c) the corresponding maximum Lyapunov exponent. One can note the qualitative agreement between the experimental and numerical curves. The value of η calculated using the experimental values of components is $\eta = 9.809 \times 10^{-5}$, $\phi = \frac{-\pi}{4}$ 63

3.8 (Observation of one step of the bifurcation curve when $\beta = 1.379$. 64
3.9 (Time traces and phase portraits (for $\phi = \frac{-\pi}{4}$, and $\eta = 9.809360 \times 10^{-5}$) of the system at different levels of the bifurcation diagram.$|\gamma| = 1.1$ (a) and (d), $|\gamma| = 2.5$ (b) and (e), and $|\gamma| = 3.0$ (c) and (f). 65
3.10 Variation of the amplitude versus the effective feedback gain $|\gamma|$. The analytical curve (solid line) is obtained from equation (3.64), while the numerical curve (black circles) is plotted using equations (3.22) and (3.23). $\phi = -\frac{\pi}{4}$, $y_{st} = 14.6$, $\eta = 9.809360 \times 10^{-5}$, and $\phi = \frac{-\pi}{4}$. 70
3.11 Evolution of the effective frequency as a function of the normalized time-delay ν. For the solid line (upper curve), $\eta \neq 0$ and for the dots line (bottom curve), $\eta = 0$. $y_{st} = 14.6$, $\phi = -\frac{\pi}{4}$ and $\delta = -0.02$. 71
3.12 Analytical bifurcation map showing the transition between supercritical and subcritical Hopf bifurcation when $\eta = 0$ (the left curve). The horizontal line marks the frontier. For this results, we have focused on the negative slope. On the right we have, for standard-OEO, the analytical bifurcation map which shows the supercritical Hopf bifurcation when $\eta \neq 0$ 72
3.13 Below the border, from bottom to top, these are supercritical curves for η ($\eta = 7.80936 \times 10^{-5}$,$\eta = 5.80936 \times 10^{-5}$,$\eta = 3.80936 \times 10^{-5}$,$\eta = 2.80936 \times 10^{-5}$). The mixed curves are those obtained for $\eta = 1.80936 \times 10^{-5}$,and $\eta = 0.580936 \times 10^{-5}$ 72
3.14 (Color online)(a) Experimental setup of OEO featuring both the laser and the filter nonlinearities and (b) Nonlinear Capacitor (NC). The laser used is a DFB telecom laser diode ($\sim 1.55\ \mu m$) with a threshold injection current $I_{\text{th}} = 15.2$ mA. The 656 m optical fiber induces a time-delay of $T_D = 3.28\ \mu$s. PD is Photodiode, I_{pol} is polarization current; I_{RF} is the current from feedback loop. CNBPF refers to Cubic-Nonlinear Band-pass Filter, VS is the voltage subtractor. 75
3.15 Analytical plot of the fixed point y_{st} as a function of the feedback gain β ($\mu = 0.21$, and $\vartheta = -0.12$) (see equation (3.83)). 78
3.16 Numerical plot of the bifurcation diagram for the variable x of the system as a function of ϑ for $\nu = 53.14$ and $\beta = 1.08$. 79
3.17 (a) Numerical plot of the bifurcation diagram for the variable x. (b) Lyapunov exponent Λ of the system $\nu = 53.14$ and $\alpha = -0.12$. 80
3.18 (a) Numerical plot of the bifurcation diagram for the variable x. (b) Lyapunov exponent Λ of the system $\nu = 53.14$ and $\alpha = -0.12$. 81
3.19 Timetraces of the signal around the jump amplitude. The dashed line is the timetrace of the signal for $\beta = 1.35$ (i.e. just before the jump point), and the red one is the timetrace of the signal for $\beta = 1.36$ (i.e. just after the jump point). 81

3.20 Numerical simulations of the CN-OEO-LASER for $\nu = 53.14$ and $\alpha = -0.12$, when β is varied. (a) is quasi sinusoidal oscillations for $\beta = 1.08$, and (b) is slow-fast oscillations for $\beta = 1.5$. 83
3.21 Time traces of the simplified CN-OEO. Left column [(a), and (b)]: corresponding numerical simulations from Eqs. (3.76) and (3.77) for $\nu = 53.14$ and $\alpha = -0.12$, when β is varied. (a) is x for $\beta = 1.08$, and (b) is x for $\beta = 1.5$. Right column [(c),and (d)] experimental measurements for $R = 2.5\,k\Omega$, $r = 300\,\Omega$, $C_1 = 270\,pF$, $C_2 = 9.15\,nF$, $T_D = 3.28\mu s$, and $V_{th} - V_{pol} = 1.314\,V$. 84
3.22 Time traces of the experimental and numerical results when the feedback gain become large ($\beta = 2.5$). Other parameters are the same as in Figure 3.21. 84

List of Tables

List of Abbreviations

AC: *Alternative Current*
Amp: *Amplifier*
BPF: *Band Pass Filter*
CN: *Cubic Nonlinear*
CNBPF: *Cubic Nonlinear Band Pass Filter*
CN-OEO: *Cubic Nonlinear Optoelectronic Oscillator*
DC: *Direct Current*
DET: *Differential Equation with Time-delay*
DFB: *Distributed Feedback*
DL: *Delay Line*
Fortran: *Mathematical Formula Translating System*
Hz: *Hertz*
kHz: *KiloHertz*
LDC: *Laser Diode Controller*
LED: *Light-Emitting Diode*
MATLAB: *Matrix Laboratory*
MC: *Microwave Coupler*
MZM: *Mach-Zehnder Modulator*
NC: *Not connected*
OC: *Offset Controller*
ODE: *Ordinary Differential Equation*
OEO: *Optoelectronic oscillator*
OPAMP: *Operational Amplifier*
PC: *Polarization controller*
PD: *Photodiode*
RK4: *Fourth-Order Runge-Kutta*
RF: *Radio Frequency*
V: *Volt*
VdP: *Van der Pol*
VdP-OEO: *Van der Pol Optoelectronic Oscillator*
VS: *Voltage Subtractor*

Abstract

This thesis is oriented along two lines of research: the study of the dynamics of an optoelectronic oscillator whose electronic part is made of a nonlinear filter that we have called cubic nonlinear optoelectronic oscillator and the study of the dynamics of an optoelectronic oscillator which exhibits two nonlinearities, that of the laser and that of the nonlinear cubic band-pass filter.

First, a theoretical approach to the dynamics of the cubic nonlinear optoelectronic oscillator shows that this new architecture induces an additional timescale to those already existing in the standard optoelectronic oscillator. This additional timescale is the basis of a multi-scales dynamics which begins with a limit-cycle oscillations and evolves into chaos through crenelated oscillations as the feedback gain increases. This optoelectronic oscillator made with cubic nonlinear band-pass filter can operate equally well in narrow-band or wide-band configuration. It can generate breathers when adjusting certain parameters of the system. This could be useful in applications where breathers are required or not. The optoelectronic oscillator has a time-delay which gives it an infinite dimension. We use the normal form theory to transform this infinite-dimensional system into a two-dimensional (amplitude and phase) differential system. This reduction makes it possible to analytically determine the expressions of the amplitude and the frequency of the limit-cycle oscillations as a function of other parameters of the system such as the time-delay and the feedback gain. This allows us to analytically confirm that this new architecture produces limit-cycle oscillations whose frequencies are higher than those of the classical optoelectronic oscillator. The experimental study is made and confirms the theoretical results.

Secondly, we present the theoretical and experimental study of the dynamics of the cubic nonlinear optoelectronic oscillator in which the electrical-to-optical conversion is performed by the laser diode. This allows us to observe that the system oscillates only for an appropriate and negative value of the bias voltage. The frequency of the oscillations increases with the feedback gain, and the cubic nonlinear parameter and decreases with the normalized time-delay parameter. An experimental study confirms that the dynamics of this oscillator is dominated by the limit-cycle oscillations which provides quasi-sinusoidal and the slow-fast oscillations as the feedback gain increases. We thus obtain an optoelectronic oscillator whose cost is reduced and which, thanks to its slow-fast dynamics, can be

exploited in several biological, chemical, mechanical, electronic, optical, and engineering systems.

Keywords: Optoelectronic oscillator, cubic nonlinear pass-band filter, cubic-nonlinear Optoelectronic oscillator, slows-fast Oscillation, crenellated oscillations, chaos.

Résumé

Cette thèse est orientée suivant deux axes de recherche: l'étude de la dynamique d'un oscillateur optoélectronique dont la partie électronique est faite d'un filtre non linéaire que nous appelons oscillateur optoélectronique cubique non linéaire et l'étude de la dynamique d'un oscillateur optoélectronique qui présente à la fois les non linéarités du laser et du filtre passe-bande cubique non linéaire.

Dans un premier temps, une approche théorique de la dynamique de l'oscillateur optoélectronique cubique non linéaire montre que cette nouvelle architecture induit une échelle de temps multiple supplémentaire à aux trois échelles de temps de l'oscillateur optoélectronique standard. Cette augmentation est à la base d'une dynamique multi-échelle qui commence par un cycle limite et évolue vers le chaos en passant par un signal en créneaux au fur et à mesure que le gain de la rétroaction augmente. Cet oscillateur peut aussi bien fonctionner en configuration bande-étroite ou bande-large. Il peut présenter le phénomène de battement dit " breathers " lorsqu'on ajuste certains paramètres du système. Ceci pourrait être utile dans les applications necessitant les breathers. L'oscillateur optoélectronique possède un retard temporel, qui lui confère une dimension infinie. Nous utilisons la théorie de la forme normale pour transformer ce système de dimension infinie en un système différentiel à deux dimensions (amplitude et phase). Cette réduction permet de déterminer analytiquement les expressions de l'amplitude et de la fréquence des oscillations de cycle limite en fonction des autres paramètres du système tels que le retard et le gain de la rétroaction. Cette demarche nous permet de confirmer analytiquement que cette nouvelle architecture produit un cycle limite dont les fréquences sont plus élevées que celles de l'architecture de l'oscillateur optoélectronique classique. L'étude expérimentale est faite et confirme les résultats théoriques et analytiques.

Dans un deuxième temps, nous présentons l'étude théorique et expérimentale de l'oscillateur optoélectronique cubique non linéaire dans lequel la conversion électrique optique est réalisée par la diode laser. Cela nous permet de constater que non seulement le système n'oscille que pour une valeur appropriée et négative de la partie continue de l'alimentation du laser, mais aussi que la fréquence des oscillations augmente avec le gain de la rétroaction et le paramètre cubique non linéaire, mais décroit avec le paramètre du retard normalisé. Une étude expérimentale permet de confirmer que la dynamique de cet oscillateur est dominée par le cycle limite qui fournit des oscillations lentes et rapides au

fur et à mesure que le gain de la rétroaction croit. Nous obtenons ainsi un oscillateur optoélectronique dont le coût est réduit et qui grâce à sa dynamique lente-rapide, peut être exploité dans plusieurs systèmes biologiques, chimiques, mécaniques, électroniques, optiques et d'ingénierie.

Mots-clés: Oscillateur optoélectronique, filtre passe-bande cubique non linéaire, oscillateur optoélectronique cubique non linéaire, oscillations lentes-rapides, oscillations crenelées, chaos.

GENERAL INTRODUCTION

Optoelectronic Oscillators (OEOs) are self-sustaining systems made up of two blocks: an optical block and an electronic block. They are the basis for the generation of both optical and electrical signals. Initially, their main fields of application were telecommunications. Therefore, they make it possible not only to generate ultra-pure signals for detection but also complex signals for chaos communication. Nowadays, their applications are becoming more and more numerous; they are also used in neuroscience and high precision metrology.

OEOs are autonomous systems in which the signal, in a closed loop configuration, is alternately converted into the optical and electrical domains. Initially, a laser diode produces a light beam which will be phase or amplitude modulated by suitable nonlinear device which is fed by an electrical signal. The signal coming from this phase or amplitude modulator is delayed during its progression in an optical fiber where it will undergo a series of reflections. The modulated and delayed optical signal will then be photodetected by a photodiode which will convert this optical signal into an electrical signal. The electrical signal thus produced will feed the electronic part which can be a band-pass-filter. This filter will give an output signal which will be amplified and feedback into the light modulator [1–4]. OEOs are made from ultra-fast optical and electronic devices, which allow them to have multiple timescales. Compared to other, the dynamics of optoelectronic oscillators (OEOs) can extend over several orders of magnitude and generate signals of very high frequencies [5–7]. In recent decades, several OEOs architectures have emerged and have given rise to several applications in basic and applied sciences.

The OEOs are ideal for studying the nonlinear dynamics of autonomous systems. After the pioneering work of Neyer and Voges, these oscillators have been widely studied from the point of view of fundamental sciences [8–22]. These studies have generated many technological applications. They were used to generate ultra-pure microwave signals [23–34], for neuromorphic computers [35–42], for metrology and detection [43–45], chaotic cryptography [46–49], and several other technological applications [50–54]. Recently, several studies have demonstrated the possibility of implementing these oscillators on chips [**?**, 55, 56].

The richness and varied applications of the OEO are at the origin of the search of new architectures. Indeed, it has been observed that the nature of the filters influences the dynamics of the optoelectronic oscillator. This means that the dynamics of OEOs strongly depends on the electronic part. For example, in the Ikeda model, the dynamics of low-pass filtering are quite different from those of OEOs with band-pass filters. With band-pass OEOs, the dynamics still depends critically on the nature of the filter. Generally, the electrical part consists of a linear response filter. However, nonlinear response filters have already been shown to be effective in studying complex dynamics such as antimonotonicity and some bursting-like oscillations not encountered in the standard OEO [57, 58]. It is therefore interesting to study a OEO architecture which has a nonlinear response filter.

Regarding the nonlinear filters, some have already been used in the field of optics like for example the Chua, Colpitts, and Van der Pol oscillator [59–66]. Some of these filters have been introduced in optoelectronic oscillators and have generated useful signals for several OEO applications. These are particularly Van der Pol and Colpitts oscillators. Faced with the complexity associated with the implementation of nonlinear response filters in optoelectronic oscillators, one wonders if it would not be possible to propose a new nonlinear filter whose implementation and mathematical modeling would be simple than those known until now? The search for a simple nonlinear filter to implement in optoelectronic oscillators and whose mathematical model would be just as simple led us to create a filter that we called a cubic nonlinear band-pass filter (CNBPF). It is a nonlinear RLC circuit made with a nonlinear capacitor. Nonlinear capacitors are made up of single junction diodes. They are important components in electronic systems, both from the point of view of fundamental sciences and from the point of view of technology [67–71]. The choice of the nonlinear capacitor here is justified by the fact that they are used in snubber circuits for power electronics, and can operate at high frequencies. The new architecture of OEO which use a CNBPF is more versatile than the standard OEO because it allows to generate breathers or not by tuning some parameters, displays high frequencies and amplitudes in the limit-cycle oscillations. The transition between the limit-cycle oscillations and chaos is made through crenelated oscillations. This architecture can be operated either in narrow-band or wide-band configuration. The experimental results are compatible with the theoretical ones mentioned above.

The cubic-nonlinear optoelectronic oscillator (CN-OEO), having an infinite dimension, one wonders what would be the method to adopt in order to make an analytical study of the frequency and the amplitude of the signal generated by this circuit. Faced with this concern we use the normal form theory. It makes it possible to characterize an infinite dimensional system into a two-dimensional differential system. It allows us to study in depth in an analytical way the amplitude and the frequency of the limit-cycle oscillations through the key parameters of the system such as the time-delay, and the feedback gain. This method has already been used for the standard OEO [12].

Despite the richness and many applications of OEOs, other objectives are to meet the strict requirements of the future communications, radar, navigation, and satellite systems. For this purpose, compact OEOs have been considered in which a laser is directly connected to a filter such as the Van der Pol oscillator, a band-pass filter, and the Colpitts oscillator [57, 66, 67]. With this architecture, the intensity modulation is performed through the piecewise-linear (that is, nonlinear) power- intensity transfer function of the laser-diode. Looping an OEO on the laser reduces the price, the number of components, and the electrical energy consumption. Hence, the name of simplified OEO is employed. However, the drawback of this method is the reduction in the bandwidth imposed by the laser relaxation oscillations of the laser itself compared to the OEO bandwidth using a

phase or amplitude modulator. It is in this logic that we have also proposed a study of the dynamics of the CN-OEO whose CNBPF is directly connected to the laser which plays the role of electrical-to-optical converter.

A simplified analysis of CN-OEO makes it possible to realize the quasi-sinusoidal dynamics and the slow-fast dynamics of the oscillations. It is important to highlight that the slow-fast dynamics are responsible for canard explosions which are observed in many biological, chemical, mechanical, electronic, optical, and engineering systems [72–84].

The present work is divided in three chapters.

Chapter one is devoted to the literature review on the evolution of work on the optoelectronic oscillator by describing the standard OEO first, some OEOs that have a nonlinear filter, and those which use a laser diode to do the electrical-to-optical conversion. This part will end with the problems that this thesis solves.

Chapter two will explain the methodology used. It will highlight the mathematical methods used to describe the optoelectronic oscillators, the techniques for solving the equations generated by these oscillators, the digital methods used to explain their dynamics and the experimental method.

Chapter three will present the results obtained and we will end the thesis by a general conclusion and perspectives.

Chapter 1

LITERATURE REVIEW

1.1 Introduction

The study of optoelectronic oscillators controlled by various filters is a very interesting subject. These filters are electronic oscillators. These electronic oscillators are autonomous and can generate special signals, including pulse, slow-fast oscillation, bursting signals, and chaos when they are used as filter in OEO [?,?,57,66,67]. In general the electric branch of OEOs is considered to be linear. However, nonlinear electrical response can be an ideal benchmark to investigate the complex dynamics in OEOs. The nonlinear filters are implemented and can operate in high frequency signals. Another preoccupation is to reduce the number of components and energy consumption. In this chapter, we will first present the applications of the optoelectronics oscillators. Secondly we will briefly describe the basic principles of an optoelectronic oscillator and then present its characterization by using a normal form method. Thirdly, we will present a literature review on the OEOs which use a nonlinear filter. Fourthly, we will present some architectures of OEOs which use a laser diode for optical-to-electrical conversion. The problems to be solved in the thesis will be presented in the last but one section. Conclusion is given in the last section

1.2 Optoelectronic oscillators (OEOs) and its characterization by Normal Form Method.

This section is divided in two main parts. The first one briefly describes the basic principles of a standard optoelectronic oscillator and the second one presents the characterization of that standard OEO near the primary Hopf bifurcation in term of key parameters of the system by using a normal form method.

1.2.1 Basic principles of a standard optoelectronic oscillator.

Optoelectronic oscillators are looped autonomous systems in which an electronic part loops over the optical part. The electronic part consists of a filter which imposes the frequency and an amplifier which amplifies the power of the signal. The optical part is made of a laser emitting a continuous wave, an electro-optical modulator (seat of the optical nonlinearity), a roll of optical fiber or an optical resonator which creates a time delay in the loop, and a photodiode which ensures the optical-to-electrical conversion (see Figure1.1).

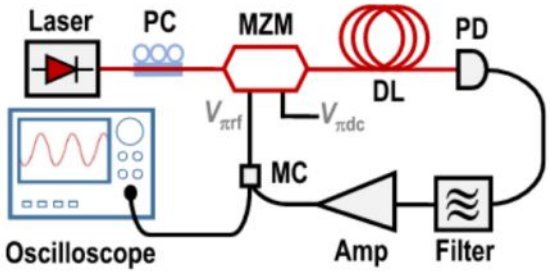

Figure 1.1: Experimental setup of the OEO. PC, polarization controller; MZM, MachZehnder modulator; DL, delay line; PD, photodiode; Amp, RF amplification; MC, microwave coupler [12].

The experimental setup of the standard optoelectronic oscillator (OEO) is presented in Figure 1.1 and described as follows [21]: A polarized light of power Pin delivered by a telecommunication continuous-wave laser diode is modulated with a Mach-Zehnder modulator (MZM) whose half-wave voltages are $V_{\pi RF}$ and $V_{\pi DC}$. The modulated light coming from the MZM is retarded into an optical delay line resulting in a time-delay equal to T_D, before being converted to an electrical signal with a photodiode (PD) of responsivity S. The electrical signal generated by the photodiode V_{in} passes through a Radio Frequency filter (RF) with outputs V_{out} and in turn is suggested to an amplification before being re-injected into the RF electrode of the MZM.

These architectures makes it possible to achieve an approximative performance of electronic oscillators in tern of few GHz operating frequency and spectral purity (phase noise of -160dBc/Hz at 10GHz carrier). This system is described by an integro-differential delay equation of the Ikeda type [21]:

$$x + \tau\frac{dx}{dt} + \frac{1}{\theta}\int_{t_0}^{t} x(s)ds = \beta\cos^2[x(t - T_D) + \phi]\,, \tag{1.1}$$

where β is the normalized feedback gain which is proportional to the power of laser diode, ϕ is the phase corresponding to the half-wave voltage of the bias and the variable $x(t)$ represents the normalized voltage crossing of the circuit. The integral term is in the base of many dynamics in the system such as breathers, pulse package. The dynamics observed in the standard OEO are the phenomenon of relaxation, breathers, and chaos presented in Figure 1.2. To perform the OEO for many other applications, the electronic part was revised in order to have new dynamics, operating in many bandwidths, with high purity, and high frequency.

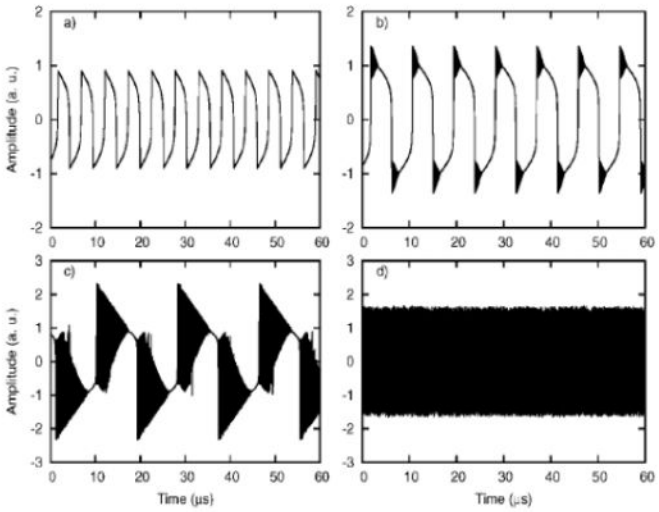

Figure 1.2: Time traces of the variable x for different values of the feedback gain β of standard optoelectronic oscillator. $\phi = \frac{-\pi}{4}$ (a) $\beta = 1.5$, (b) $\beta = 2$, (c) $\beta = 3$, and (d) $\beta = 3.5$ [21].

1.2.2 Characterization of the bandpass OEO near the primary Hopf bifurcation by the normal form method.

In 2019, TALLA Mbé *et al.*, proposed an experimental and theoretical study of a normal form method for the determination of the oscillations characteristic near the primary Hopf bifurcation in standard optoelectronic oscillator [12]. Principally, the amplitude and the frequency of the Hopf limit-cycles as a time-delay function and other parameters was determined. The dynamics of the OEO strongly depends on the parameters of the system namely, the time-delay, the feedback gain, and the nonlinear transfer function. TALLA Mbé *et al.* here obtained the expressions of the frequency and the amplitude as the function of the key parameters without neglecting the time-delay as it is usually the case. This was confirmed experimentally. The dimensionless form of the equation 1.1 is given by:

$$\frac{dx_1}{dt} = -x_1 - \sigma x_2 + \beta[\cos^2(x_{1\nu} + \phi) - \cos^2\phi] \tag{1.2}$$

$$\frac{dx_2}{dt} = x_1 \tag{1.3}$$

where $x_1 \equiv x$ and $x_2 = \frac{1}{\tau}\tau\int_{t_0}^{t} x(s)ds$. The parameter $\sigma = \frac{\tau}{\theta}$ is the ratio between the low and the high cut frequencies, and $\nu = \frac{T_D}{\tau}$ represents the normalized time-delay. Before computing the normal form, it is convenient to separate the above equations into a linear and nonlinear part. By using the Taylor expansion in the neighborhood of the Hopf bifurcation point and around the equilibrium point of the system, after some calculations

(details on the calculations will be given in chapter two), the complex normal form of the system is given by [12]:

$$\dot{z} = i\omega_c z - \delta\bar{b}\rho + \bar{b}\gamma_c\rho^2\bar{\rho}[2 - 4i\omega_c\gamma_c\zeta^2\Gamma e^{-2i\omega_c\nu}]z^2\bar{z} \tag{1.4}$$

where $\delta = \gamma - \gamma_H$ is the relative effective feedback gain. The "overline" stands for the complex conjugation. In the first approximation, the variable z is related to the complex amplitude of limit-cycle oscillation by $z(t) = A(t)e^{i\omega_c t}$ which, replaced in equation 1.4 leads to the complex normal form of the amplitude:

$$\dot{A} = -\delta\Lambda_1 A + \Lambda_2 A^2\bar{A}\,, \tag{1.5}$$

where the coefficients Λ_1 and Λ_2 have the following expressions:

$$\Lambda_1 = \frac{i\omega_c e^{-i\omega_c\nu}}{[1+2i\omega_c+\gamma_c(1-i\omega_c\nu)e^{-i\omega_H\nu}} \quad , \tag{1.6}$$

$$\Lambda_2 = 2\gamma_c\omega_c^2\Lambda_1[1 - 2i\omega_c\gamma_c\zeta^2\Gamma e^{-2i\omega_c\nu}] \tag{1.7}$$

Equation (1.5) is a complex equation. To study the evolution of the amplitude and the frequency around the Hopf bifurcation, it is required to do the following approximation $A = a(t)e^{i\varphi(t)}$. After investigating the stability of the equilibrium point, it can be shown that the amplitude and the frequency of the limit-cycle can be explicitly defined as a function of $\delta = \gamma - \gamma_H$ following:

$$a = 2\omega_H\sqrt{(\gamma - \gamma_H)\frac{\Re[\Lambda_1]}{\Re[\Lambda_2]}} \tag{1.8}$$

$$\omega_{eff} = \omega_H + (\gamma - \gamma_H)\frac{\Re\Lambda_1\Im\Lambda_2 - \Im\Lambda_1\Re\Lambda_2^2}{\Re\Lambda_2} \tag{1.9}$$

where the symbols $\Re$ and $\Im$ stand for the real and the imaginary parts of their arguments respectively.

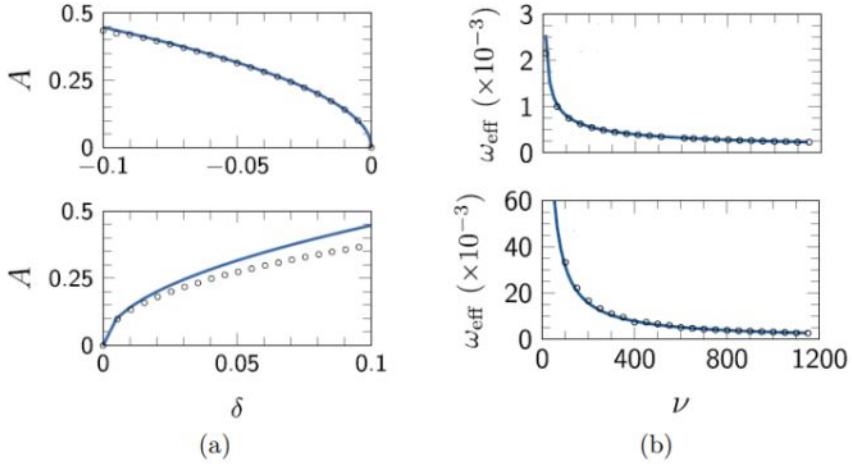

Figure 1.3: (a) Variation of the limit-cycle amplitude in case of negative slope with $\phi = \frac{-\pi}{4}$, case of positive slope with $\phi = \frac{\pi}{4}$) as the gain is varied beyond the Hopf bifurcation point γ_H as $\delta \equiv \gamma - \gamma_H$. (b) is the evolution of limit-cycle frequency in case of $\delta = -4 \times 10^2$, and $\delta = 1.5 \times 10^2$ as a function of the normalized delay $\nu = \frac{T_D}{\tau}$. Both in (a) and (c), the analytical result is displayed with a solid line and the numerical with the black circles [12].

From Figure 1.3 it is confirmed that the value of the normalized time-delay affects the characteristic of frequency. The limit-cycle amplitude shows the numerical curve and the analytical curve obtained through characterization by normal form are almost symmetric to zero, confirming that the negative slope is only defined for $\delta < 0$, and positive slope requires $\delta > 0$.

1.3 The main applications of Optoelectronic oscillators.

Optics, undoubtedly one of the oldest sciences, has undergone spectacular upheavals over the last decades. It was first the advent of optical fibers, semiconductor lasers, and then new architectures of the optoelectronic oscillators. These discoveries have initiated the move from traditional optoelectronics to miniaturization and low cost assemblies. In this section, we will highlight some applications of optoelectronic oscillators.

1.3.1 OEO-based Chaos Synchronization and Communications.

The search for confidentiality during the transport of information is the basis for the creation of several optical architectures. OEO architectures are used to provide privacy in optical networks. Information is transmitted through a chaotic optical carrier and retrieved via chaos synchronization.

Goedgebuer *et al.* in 1998 (see [85]), proposed an Ikeda OEO system for chaos communications. With this architecture, they managed to transmit a hidden audio signal in a chaotic carrier. After this pioneering work, several architectures have been proposed in order to improve chaotic communication. The architecture presented in Figure 1.4 is from the work of Chembo in 2019 [86].

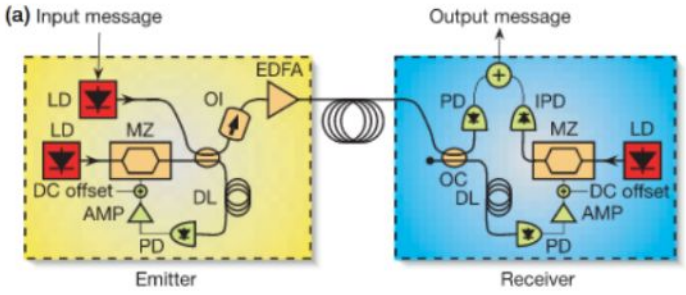

Figure 1.4: Field experiment of chaos communication using an Ikeda-based optoelectronic oscillator. (a) Emitter-receiver system. The emitter uses a laser diode (LD), MachZehnder modulator (MZ), an erbium-doped fiber amplifier (EDFA) to boosts the power of the signal to be launched into the transmission line [86].

The signal to be masked is added to the laser electrode while controlling its emission wavelength. The chaotic carrier is an OEO of well-defined bandwidth. An optical fiber will then transport the information from the transmitter to the receiver. The receiver is also an optoelectronic oscillator from which the information which has been masked can be extracted. Goedgebuer et al carried out a successful chaos communication experiment with a pseudorandom binary signal at $100Mbit/s$, over a $50 - km - long$ optical fiber channel.

From this basic architecture, several architectures have been developed insofar as the transmitter and the receiver designed based on the OEO have undergone improvements. One of the most active lines of research related to optical chaos communications is the improvement of both the performance and security of the existing systems. For this purpose, in 2008, Cohen et al. proposed and experimentally observed the nonlinear dynamics of an optoelectronic time-delayed feedback loop designed for chaotic communication using commercial optical fiber links [87]. Their optoelectronic system shown in Figure 1.5 can be used as a transmitter and receiver for a high-speed chaotic communication demonstration over a commercial optic fiber channel. Their architecture is presented in Figure 1.5.

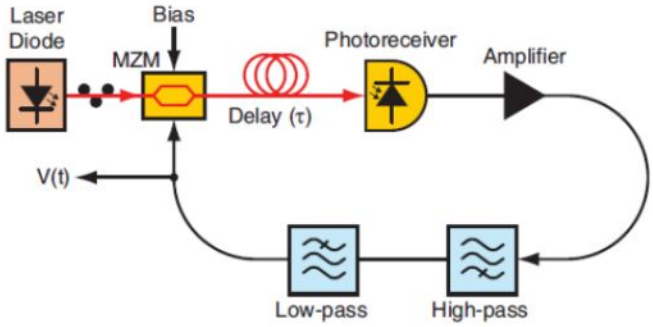

Figure 1.5: The optoelectronic using Synchronization for prediction of high-dimensional chaotic dynamics [87].

1.3.2 OEO-based Reservoir Computing

Designing materials inspired by the human brain is a constant challenge. In the same way that we train the human brain to retain information, we train machines to retain information and restore it. Training a neural network for a given task typically consists of finding the optimal connectivity between the neurons. However, this procedure can be particularly difficult, time consuming, and computationally expensive, most notably when the number of neurons is large. The first implementation of reservoir computing with time-delayed systems was proposed by Appeltant et al. in 2011, using an electronic circuit modeling the Mackey-Glass dynamics [88].

In recent years, broadband OEOs have gradually established themselves as a powerful technology platform for analog computing machine learning. The operation of the neural network highlights the use of key properties for the analog calculation. These features can be emulated in OEOs, with the ability to process information with ultra-high bandwidth. The neurons are generally nonlinear nodes, while the coupling among themselves, also called connectivity, can at the same time be variable, random, and sparse. An example of OEO-based reservoir computing is displayed in Figure 1.6

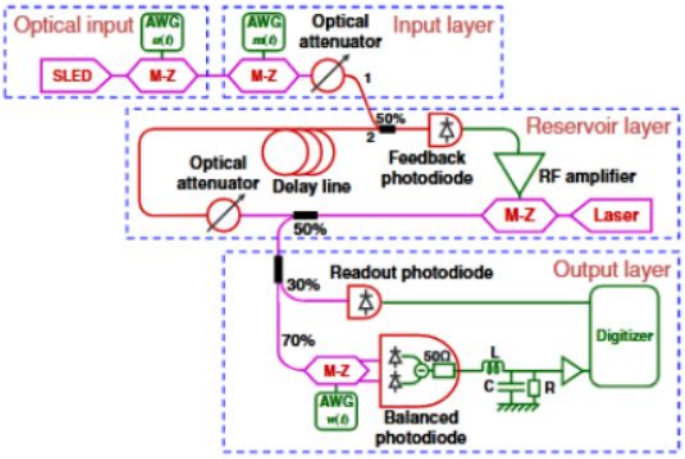

Figure 1.6: Schematic of an experimental OEO reservoir computer. The reservoir layer is a delay dynamical system in which a Mach-Zehnder (MZM) modulator acts as nonlinearity. The information is mixed to the signal using an arbitrary waveform generator (AWG) [89].

In Figure 1.6, the input layer is used to drive the reservoir computer which is an optoelectronic oscillator (reservoir layer). The output layer is a circuit that decodes the output signal. An input signal is fed into the reservoir, which is considered a "black box". A reading mechanism is placed at the output of this reservoir to read the output signal. Just like the human brain, this reservoir needs to be trained in order to memorize information and return it when requested.

1.3.3 Narrow-band OEOs for ultrapure microwave generation.

A narrow bandpass OEO is mainly characterized by a feedback loop that is highly frequency selective in the radio frequency spectral domain. The optimization parameters that influence the dynamics of such systems are mainly the RF phase shifter, optical bias controller and modulator bias voltage. In this system, it is the RF filter that allows the selection of optical modes and operation at precise frequencies of the mode-locked laser. The system is then optimized to generate a comb wide and therefore a narrow optical pulse. The initial architecture is presented in Figure 1.7. It was developed by Yao *et al.* [90]:

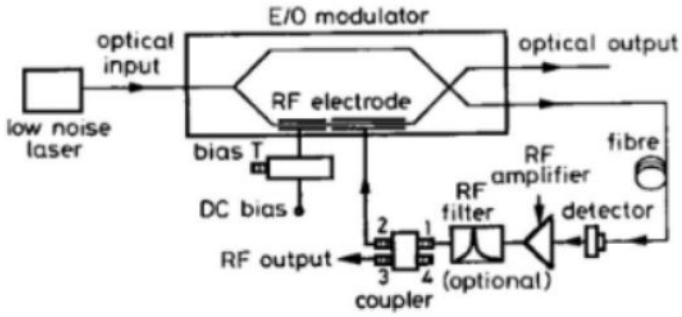

Figure 1.7: Basic single-loop OEO architecture for ultrapure microwave generation [90].

In most studies, the filter has a multi-GHz center frequency and a bandwidth of the order of a few tens of MHz. However, these values can vary largely depending on the bandwidth of the various elements of the feedback loop and thereby provide a large frequency versatility for the OEO. Note that a long-delay line improves phase noise performance and determines the microwave signal amplitude as a function of the feedback gain when it is increased beyond the normalized oscillation threshold of 1. It can be said that it is possible to drastic reduces noise in the signal generates by OEOs.

1.3.4 Optoelectronic oscillators for measurement.

Optoelectronic oscillators can be used to perform very high precision measurements. In 2014, Yanhong *et al.* [104] proposed and experimentally demonstrated a high sensitivity temperature sensor based on an optoelectronic oscillator (OEO). The idea is to highlight the application of the OEO to perform the sensing of temperature. Their OEO-based temperature sensor is presented in Figure 1.8.

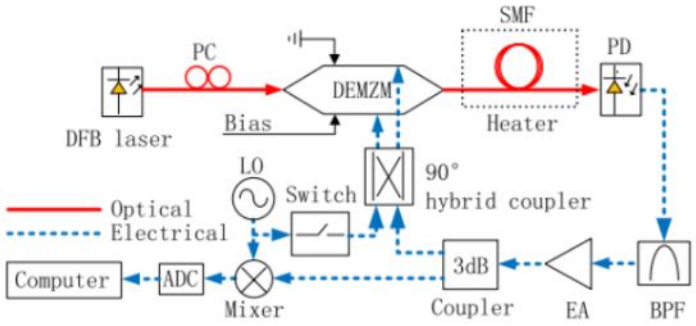

Figure 1.8: Schematic of the proposed OEO-based temperature sensor with injection locking. PC, polarization controller; DEMZM, dual electrode Mach-Zenhder modulator; SMF, single mode fiber; PD, photodetector; BPF, bandpass filter; EA, electrical amplifier; LO, local oscillator; ADC, analog-to-digital converter [104].

The DBF laser produces a light wave which is injected into a double electrode MachZenhder modulator (DEMZM) after passing through polarization controller (PC). This wave passes through a single-mode section optical fiber (SMF), which is used as the sensor head. The photodiode will convert the signal and send it to the filter. The filter selects the frequency of oscillation. A hybrid coupler is used to produce two quadratic electrical signals to drive the DEMZM for single-sideband modulation. A 3 dB directional coupler in the radio frequency (RF) link splits the oscillation signal in two parts, one part connected to the hybrid coupler input port and the other mixed with a local oscillator signal in an RF mixer. The local oscillator makes it possible to obtain the mode of oscillation locked to a preset frequency. The computer permits to monitor the dynamics.

The Single-Mode Fiber is the temperature sensor. This fiber is subjected to different temperatures. The variations of temperature consequently modifies the total time-delay τ of the OEO. The total time-delay is the sum of the time-delay of SMF and the time-delay of the OEO's loop. The total time-delay will impact the frequency of the signal. Knowing that the length of the optical fiber is affected when it is introduced into hot or cold substance. The variation of the length is recorded in terms of variation of the oscillations frequency which is itself a function of the total time-delay.

In 2014, Toan *et al.* proposed an architecture for refractive index sensing using an OEO [93]. Their architecture is presented in Figure 1.9.

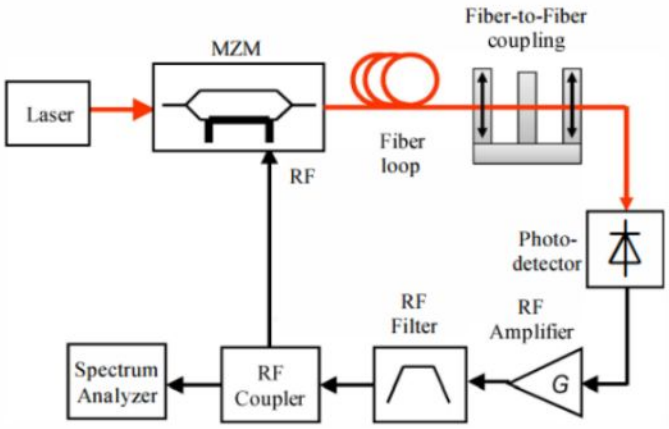

Figure 1.9: Classical structure of an opto-electronic oscillator for refractive index measurement [93].

Indeed, an optical fiber-to-fiber coupling is introduced in an OEO, just after the optical fiber. The extra time-delay due to the fiber-to-fiber coupling will cause a variation of the frequency of signal recorded on the oscilloscope. The optical time-delay takes into account the total length of the optical delay line, the length of free space, the length of substance, and the refractive index of each part. Knowing that the length of the optical fiber is affected when an optical fiber to fiber coupling is introduced, the variation of the length

is recorded in terms of the variation of the frequency oscillations which is itself a function of the total time-delay. We recall that the time-delay depends on the refractive index of the optical fiber-to-fiber coupling.

With suitable mathematical tools, it will be possible to establish the variation of the frequency according to the frequency of the signal of system. A graph will make it possible to appreciate the variation of the refractive index according to the key parameters of the system.

In 2021 Jing Zhang *et al.* in [92] proposed a technique to efficiently measure a angular velocity with improved scale factor based on a wideband-tunable optoelectronic oscillator. The circuit is proposed in Figure 1.10.

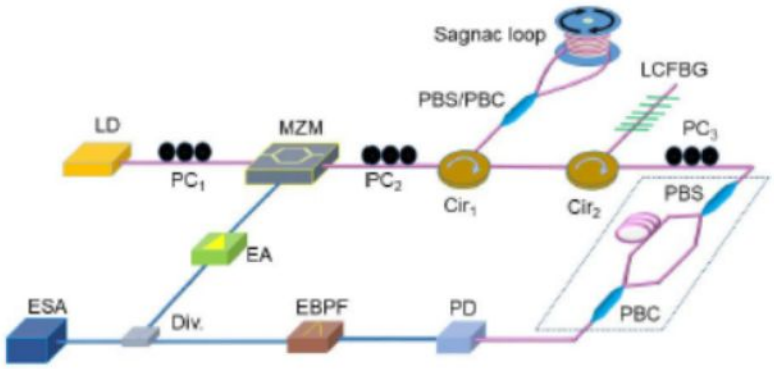

Figure 1.10: Configuration of the proposed wideband-tunable OEO for angular velocity measurement (red lines: optical fibers and blue lines: coaxial cables) [92].

The OEO consists of two cascaded Microwave Photonic Filters (MPFs), namely, a dispersion induced MPF for mainly determining the OEO's oscillating frequency and a two-tap MPF for the fine selection of the oscillating frequency. With proper control of polarization of the optical signal, the angular velocity is first mapped into the central frequency shift of the dispersion-induced MPF, which will then cause an oscillating frequency shift of the frequency. This approach ensures a large-scale factor for the angular velocity measurement due to the fact that a small phase change in the optical domain causes a large frequency shift in the electrical domain. In the circuit of Figure 1.10, MPF is a microwave photonic filters, OC is the optical carrier, PC is polarization controller, LD is laser diode, MZM is Mach-Zehnder Moulator, EBPF is an electrical, PBS is a polarization beam splitter, PBC is a polarization beam combiner, PD is polarization diode, Cir is optical circulator, EA is an Erbium amplifier, and ESA is an electrical spectrum analyser.

An OC at an angular frequency is sent to a MZM through a polarization controller (PC1). This signal will impose the polarization direction in the MZM. The transfer

function of the MZM will therefore be dependent on the angular velocity.

1.3.5 Optoelectronic oscillators as an Acoustic Sensor.

In [94], Okusaga *et al.* proposed the OEO as an acoustic sensor. Their circuit is shown in Figure 1.11.

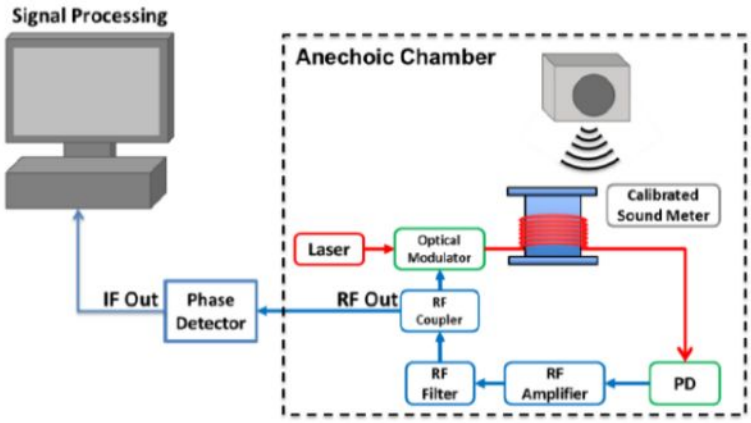

Figure 1.11: A schematic diagram of the OEO-based acoustic sensor experiment [94].

An acoustic wave is emitted so as to create a disturbance or noise in the signal which crosses the optical fiber. They used a delay-line phase-noise measurement system. They measure the phase noise which will be the sum of that of the OEO and that acoustic wave. Base on the fact that the OEO utilizes lengths of the optical fiber in ring resonator to create low-phase-noise signal, they have proposed a novel fiber-optic sensor. They demonstrated this novel fiber by measuring the modulation sidebands induced on the OEO's RF signal by an acoustic tone impinging on the fiber spool in the OEO. The narrow linewidth and high oscillating frequency of the OEO results in a sensor with both high signal-to-noise ratios and high spectral resolution.

In Figure 1.11 they placed an OEO in an anechoic chamber. They played a 1 kHz tone from a speaker approximately 3 m away from the fiber spool in order to determine the sound level at the spool. To measure the induced phase modulation sidebands, they used a delay-line phase noise measurement system. In the case of optical interferometer, they measured the induced modulation directly from the output of the photodetector in the interferometer. They used the same laser, and photodetector. They plot the noise curves of both the OEO and the optical interferometer around 1 kHz. It yields that the OEO has a comparable signal-to-noise ratios to those of the optical interferometer. This work showed that the OEO can potentially be used as a high-spectral-resolution acoustic sensor without sacrificing sensitivity.

1.4 OEOs with nonlinear filter.

The numerous applications of the OEOs encourage the search for new architectures of the OEOs which can lead to more precise simultaneous measurements, transmission of signals of higher frequencies, then to improve the already existing applications. It is noteworthy that in the most case of OEOs, the only nonlinearity of the system is the sinusoidal transfer function of the MZM. The electric branch of the feedback loop is usually linear. Several researchers have thought that introducing a nonlinear electronic feedback instead of a linear one can permit to increase significantly the complexity of the oscillator and emulates new functionalities.

1.4.1 OEOs with nonlinear filter.

In 2016, A. Talla *et al.* obtained breathers and pulse-package dynamics in multinonlinear electrooptical systems with delayed feedback [20]. They inserted a self-sustained Van der Pol oscillator in the loop and investigated the various dynamical states generated when the system is in the oscillatory regime. The schematic architecture of their electro-optic oscillator with delayed feedback is giving in Figure 1.12.

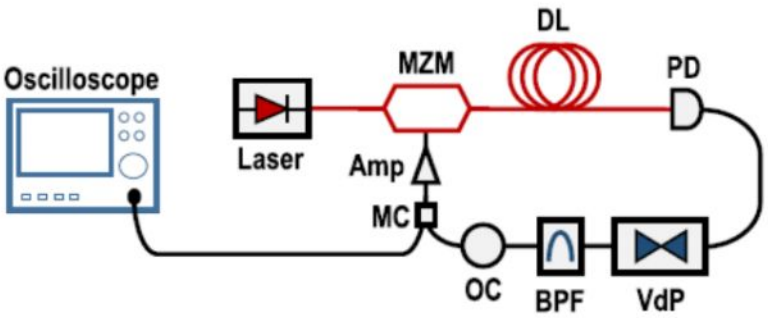

Figure 1.12: Experimental setup to explore the dynamics in multinonlinear electrooptical systems with delayed feedback. (note that bandpass filter stands here for all the bandpass filtering elements of the electric branch) Vdp is Van der pol, OC is Offest Controller [20].

The nonlinear transfer function of the MZM is known to be

$$P_{out} = P\cos^2\left[\frac{\pi u(t)}{2V_\pi} + \frac{\pi V_B}{2V_\pi}\right],$$

where P is the power of the laser, V_B is a bias voltage and V_π is the half-wave voltage of the electrode where the signal $u(t)$ is coupled. The dimensionless voltage of the Van der Pol circuit obeys to the well known equation:

$$\ddot{x} + \omega_0^2 x - \epsilon(1 - x^2)\dot{x} = 0,$$

where ω_0 is the pulsation and ϵ the nonlinear coefficient. To explore the dynamics of this novel architecture, they have first considered the case where the time-delay is set to be zero and the laser pump current increases.

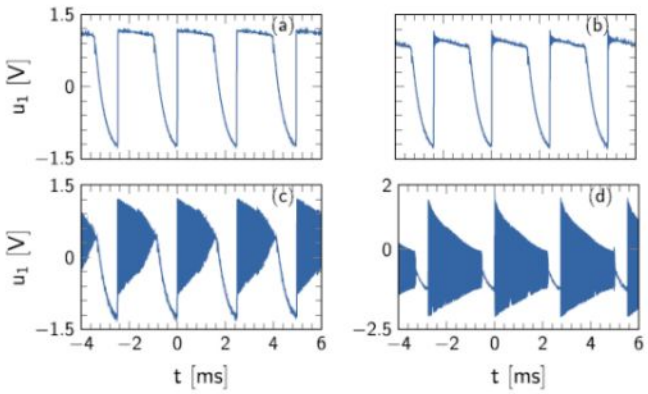

Figure 1.13: Birth and evolution of breathers in the time domain for $T_D = 0$, as the laser pump current (I) is increased beyond threshold I_{th}. (a) $I \simeq I_{th} = 27.3mA$, (b) $I = 1.23I_{th}$ (c) $I = 1.49I_{th}$ (d)$I = 1.72I_{th}$ [20].

As the pump current I is increased, quasi-square wave in Figure 1.13(a) emerges at the sharp rising edge of relaxation oscillations in Figure 1.13(b) but, they are rapidly damped shortly after their birth. As the laser power is increased, we observe that a fast-scale dynamics is superimposed onto a slow-scale limit-cycle as displayed in Figure 1.13 (c) and in Figure 1.13(d).

Still the time-delay sets to zero, when the pump current is still increasing, they obtained complex dynamics such as chaotic breathers and chaotic pulse-package oscillations (Figure 1.14).

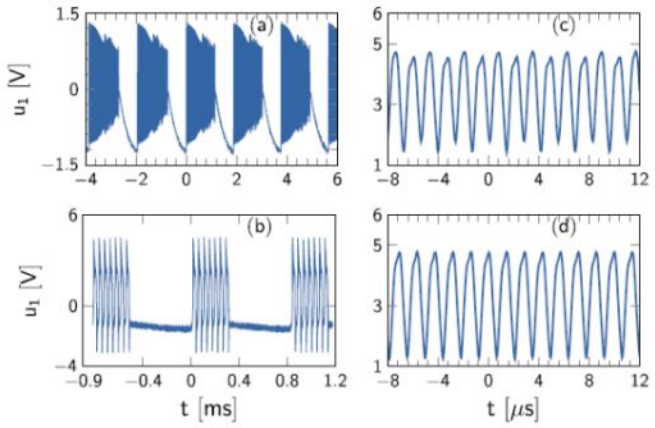

Figure 1.14: Evolution and death of breathers and pulse-package oscillations in the time domain as the laser pump current is increased far above the threshold. (a) $I = 1.81I_{th}$, (b) $I = 2.27I_{th}$ (c) $I = 2.77I_{th}$ (d) $I = 2.93I_{th}$ [20].

In Figure 1.14 (a), we observe the first chaotic breathers, characterized by a chaotic fast-scale oscillation superimposed onto a periodic slow-scale oscillation. After, as the pump current increases, a chaotic pulse-package oscillations rises Figure 1.14 (b). In Figure 1.14 (c) and Figure 1.14 (d), the further increase of pump current leads to reverse bifurcation where the system becomes bi-periodic and the periodic.

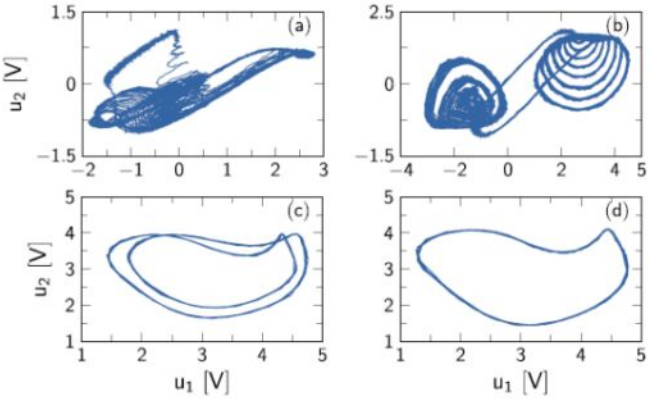

Figure 1.15: Evolution and death of breathers and pulse-package oscillations in the phase space as the laser pump current is increased far above the threshold ($T_D = 0$). Theses figures correspond to the time traces displayed Fig. 1.14. (a) $I = 1.81I_{th}$, (b) $I = 2.27I_{th}$ (c) $I = 2.77I_{th}$ (d) $I = 2.93I_{th}$ [20].

The phase portraits permit the better understanding of the time traces displayed in Figure 1.14. Figure 1.15(a) shows the inherent slow-fast structure of the chaotic attractor, Figure 1.15(b) features an asymmetric double-scroll structure. Figure 1.15(c) and Figure

1.15(d) evidences the periodic nature of the temporal output signal from Figure 1.14(c) and Figure 1.14(d).

When the time-delay is accounted, the system becomes infinite-dimensional and it has the potential to feature other complex behaviors namely relaxation oscillations.

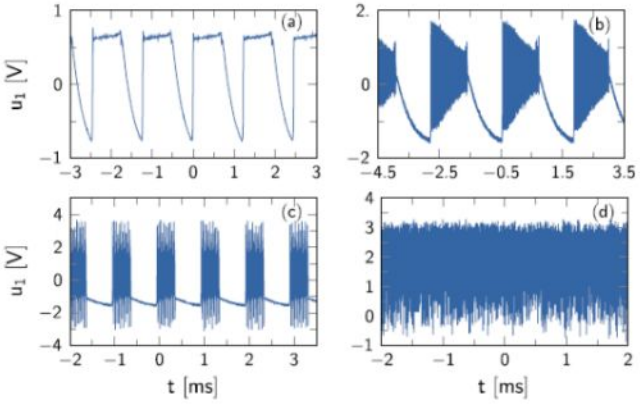

Figure 1.16: Breathers, pulse-package oscillations, and fully developed hyperchaos as the laser pump current is increased far above the threshold in the presence of delay ($T = 0.5\mu s$). (a) $I = 1.28I_{th}$, (b) $I = 1.64I_{th}$ (c) $I = 2.46I_{th}$ (d) $I = 3.34I_{th}$ [20].

When the laser is pumped just above the threshold, one obtains relaxation oscillations and breathers comparable to those obtained with zero delay which evolve towards chaos. In Figure 1.16 (a), we observe a relaxation. The first chaotic breather appears in Figure 1.16 (b), characterized by a chaotic fast-scale oscillation superimposed onto a periodic slow-scale oscillation. After, as the pump current increases, a chaotic pulse-package oscillations appears Figure 1.16 (c). In Figure 1.16 (d), the further increase of the pump current leads to chaotic signals.

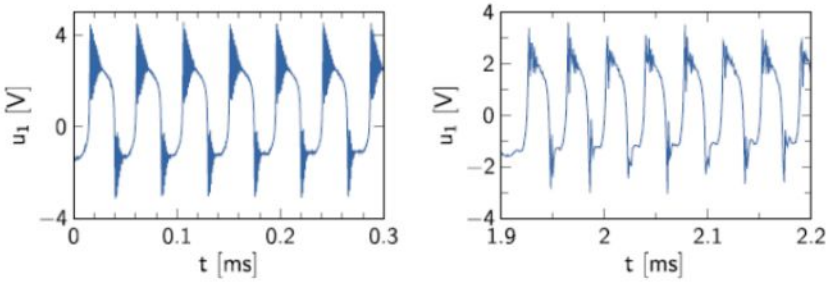

Figure 1.17: Evidence of the three-timescale behavior of the system in the pulse-package regime. (Left) pulse packages for the system without delay and with $I = 2.27I_{th}$ [see Figure 1.14(b)]. The fastest oscillations are periodic. (Right) pulse packages with delay and with $I = 2.46I_{th}$ [see Figure 1.16(c)]. The fastest oscillations are periodic [20].

1.4.2 OEO with a Colpitts oscillator.

In 2020, in Optical and Quantum Electronics journal, Mboyo *et al.*, obtained bursting oscillations in Colpitts oscillator and applied in optoelectronics for the generation of complex optical signals [58]. The setup of this architecture is presented in Figure 1.18. In this architecture, the filter is a Colpitts oscillator. The optical signal provided by distributed Feedback (DFB) laser diode then is delayed passing through an optical fiber. The delayed optical signal is detected by a fast photodiode which is an optical/electrical convertor. The output signal of the photodiode is the input signal of the Colpitts oscillator.

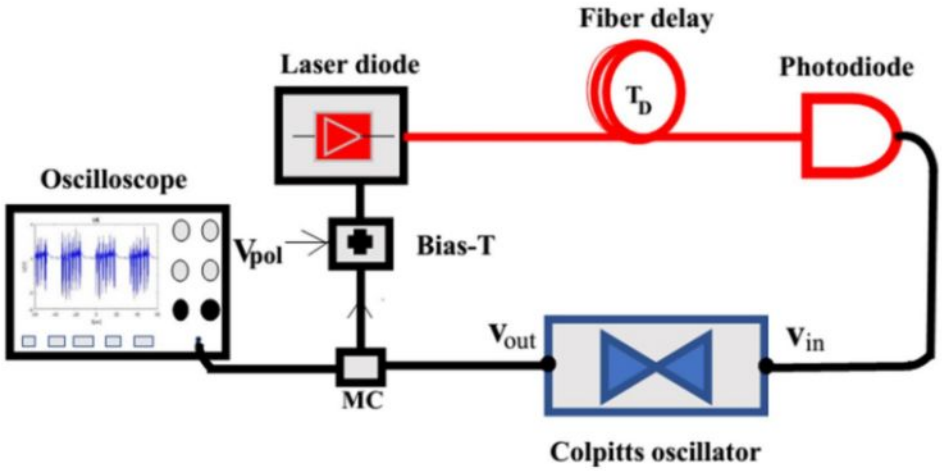

Figure 1.18: Experimental set-up of the OEO-Colpitts oscillator. MC= microwave coupler [58].

The design of the Colpitts oscillator is shown in Figure 1.19. The Colpitts oscillator is made up of four resistors, five capacitors, a coil, and a transistor. Among the resistors, one is a potentiometer and its variation modifies the dynamics of the signal emitted by the Colpitts oscillator. When the value of the potentiometer increases, the dynamics of the system passes through a steady-state, limit-cycle, and bursting oscillations.

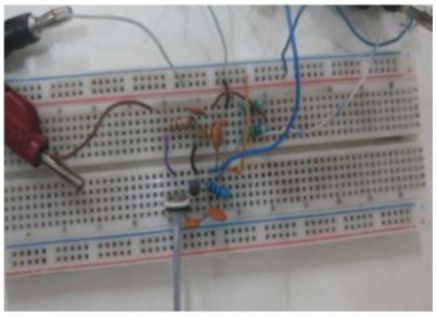

Figure 1.19: A picture of the Colpitts circuit in the laboratory [58].

A study of the dynamics of the OEO-Colpitts was carried out as a function of key parameters such as the potentiometer of the Colpitts oscillator, the laser power and the length of the optical fiber. At first, they consider the delay as being to zero (the delay line is removed: $T_D = 0$). Multiperiodic oscillations, chaotic bursting oscillations, periodic bursting and pulse-packages oscillations were obtained when the polarization voltage as the polarization increases (figure 1.20).

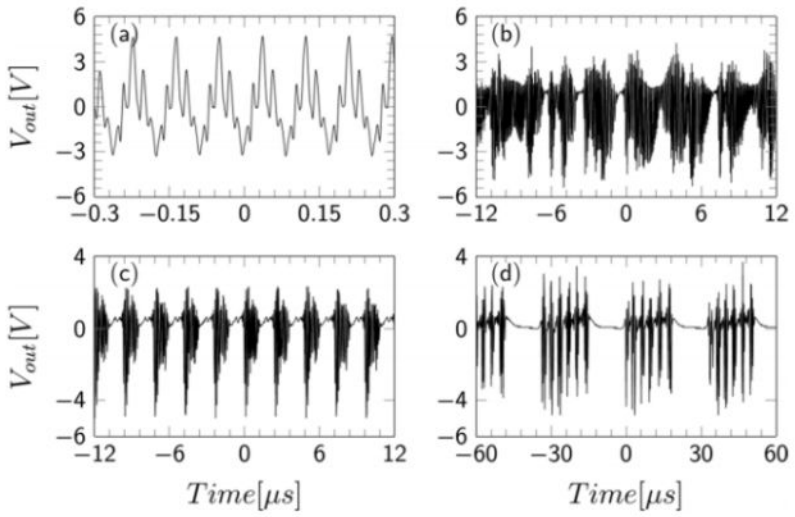

Figure 1.20: Multiperiodic, (b) chaotic bursting, (c) periodic bursting, and (d) pulsepackage oscillation in the time domain as the polarization voltage is increased beyond the threshold ($T_D = 0$) (a) $V_{pol} = 1.29V_{th}$; (b) $V_{pol} = 1.34V_{th}$; (c) $V_{pol} = 1.4V_{th}$; (d) $V_{pol} = 1.6V_{th}$ [58].

In the second time when the optical fiber is inserted, it yields (figure 1.21) multiperiodic oscillations, slow-fast dynamics, and chaotic bursting oscillation as the polarization voltage is increased.

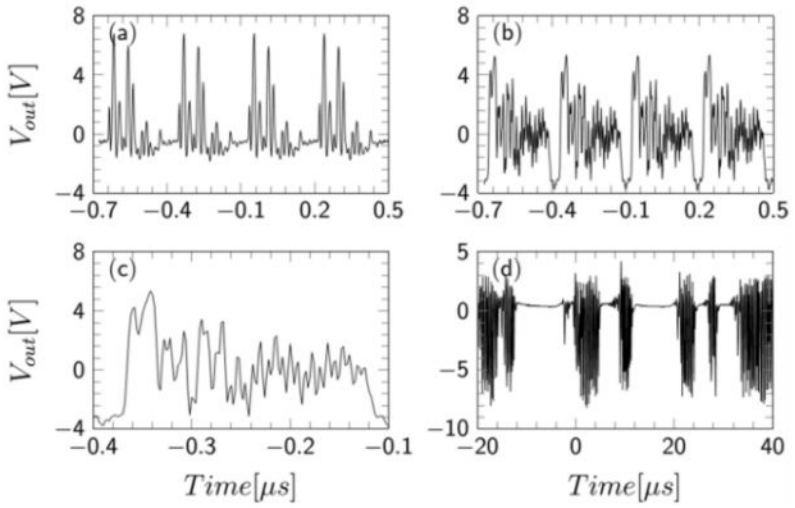

Figure 1.21: (a) Multi-periodic, (b) slow-fast dynamics, and (d) chaotic bursting oscillation in the time domain as the polarization voltage is increased beyond the threshold ($T_D = 0.2\mu s$). (a) $V_{pol} = 1.09V_{th}$; (b) $V_{pol} = 1.24V_{th}$; (d) $V_{pol} = 1.54V_{th}$; (c) is the enlargement of one package of (b) [58].

The results show that in the case where the optical fiber is removed, the dynamics offers higher frequencies bursting oscillations but, might be with slightly lower amplitude compared to the case where optical fiber is considered.

1.5 OEOs which use a laser diode for electrical-to-optical conversion.

In the standard OEO and most cases of optoelectronics oscillators, the device which performs the nonlinear conversion between the optical and the electrical signal is a phase or intensity modulator with a sinusoidal transfer function. However, a compact architecture, in which the intensity modulation of the laser light is performed through a direct optical feedback was proposed [64,65]. Generally, the majority of function generators used experimentally in laser diode current modulation are heavy, and can offer up to three functions namely, sine, square, and triangular. Autonomous oscillators are an eventual solution in the experimental laser diode modulation to generate more complex electrical signals like pulse, bursting, relaxation, and chaos oscillations [79,80].

1.5.1 OEO with direct feedback modulation.

In 2015 in the journal of lightwave technology, Chengui *et al.* presented a theoretical and experimental study of the simplest laser-based optoelectronic oscillator. Their architecture is presented in Figure 1.22.

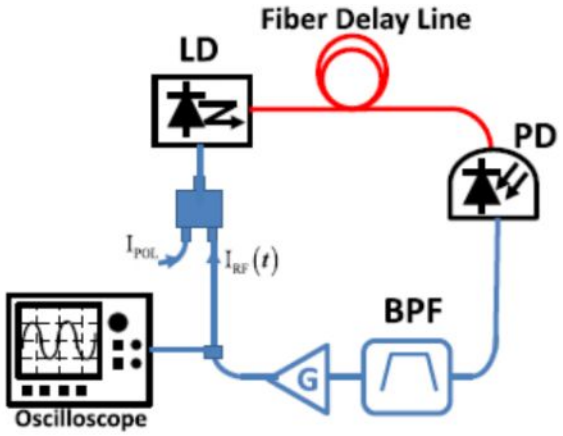

Figure 1.22: Experimental setup of direct modulation of the OEO. LD: laser diode, PD: photodiode, BPF: band pass filter, G: voltage variable attenuator [66].

It is the most simple autonomous optoelectronic oscillator with a delayed feedback loop. In this architecture, an electrical signal powers the laser which provides light which powers the oscillator. Indeed, this signal is delayed into the optical fiber then converted into an electrical signal through the photodiode. This electrical signal is feed the BPF and the output signal returns in the laser diode. The behavior of this OEO is critically dependent on the value of the feedback gain. This model gives an integro-differential equation characterized by three time scales indicated by the equation below:

$$x + \tau\frac{dx}{dt} + \frac{1}{\theta}\int_{t_0}^{t} x(s)ds = \beta D[x(t - T_D) - \vartheta]\,, \tag{1.10}$$

where D is the dimensionless nonlinear transfer function of laser diode, x the dimensionless voltage, θ the offset dimensionless voltage, β the feedback gain loop. The dynamics of the system depends on the sign and the value of the polarization current. In the case where $\vartheta > 0$, there is not oscillations in the system. In the case where $\vartheta < 0$, the system oscillate for a specifical value of ϑ.

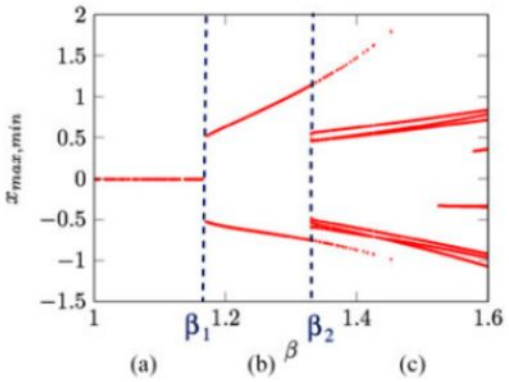

Figure 1.23: Numerical bifurcation diagram of the simplest OEO where the variable x, is plot as the gain β is increased [66].

In Figure 2.4, the bifurcation diagram show that the dynamics of this oscillator is dominated by the limit-cycle oscillation. For certain value of the feedback gain β, they is not oscillation in the system. For $1.18 < \beta < 1.34$ a fast-scale limit-cycle oscillations are sustained. For $\beta > 1.34$, a slow-scale limit-cycle oscillations can be excited.

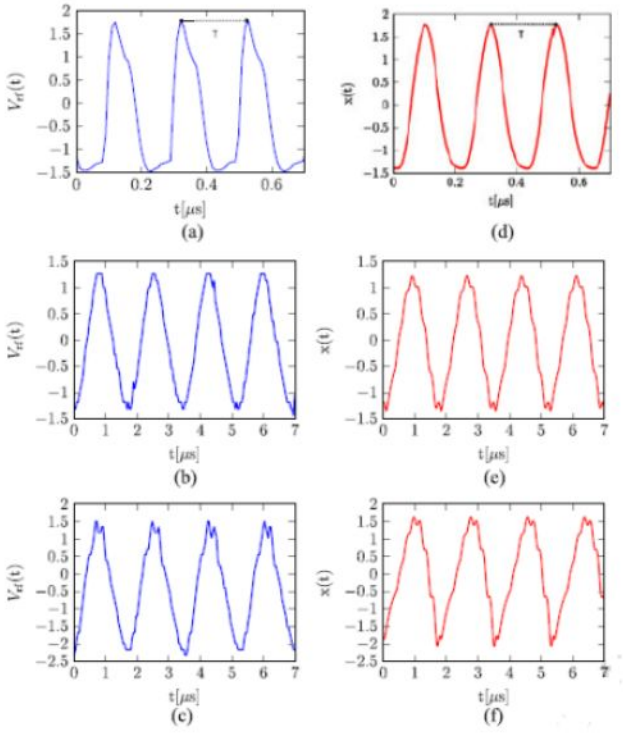

Figure 1.24: Experimental (left column) and numerical (right column) timetraces of the simplest OEO. $\vartheta = -0.5$, $\beta = 1.29$, $\beta = 1.37$, $\beta = 1.6$ [66].

It is important to precise that this work was done in the case of low pump currents. We see a excellent agrement between the numerical and experimental simulations (Figure

2.5). We can conclude that a nonlinear filter can seed a laser diode for optical-electrical conversion in optoelectronic oscillator.

1.5.2 OEO with modulation through a Van der Pol electrical component.

Goune *et al.* in 2018 presented an OEO where a Van der Pol oscillator is used as a filter and the laser is used for do the optical-to-electrical conversion [57]. The system is presented in Figure 1.25.

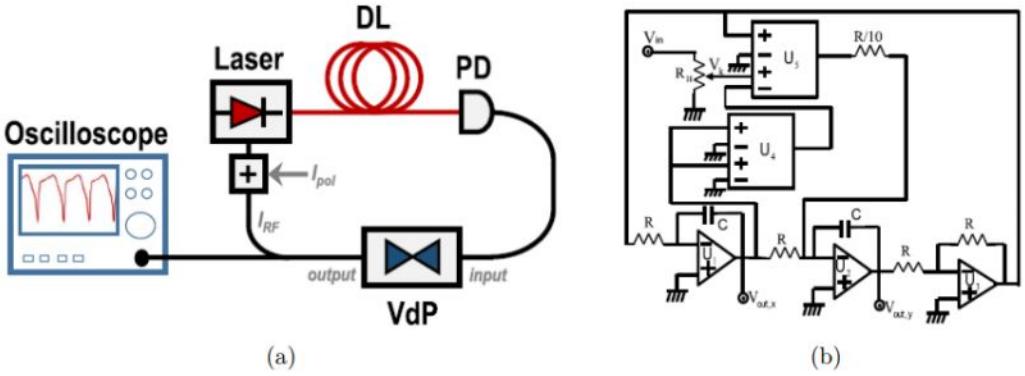

Figure 1.25: (a) The experimental setup of Van der Pol-optoelectronic oscillator and (b) experimental setup of the Van der Pol oscillator [57].

In this case, the additional nonlinearity from the nonlinear filter is expected to generate novel complex behaviors that do not exist in the conventional OEO architectures. Inserting a Van der Pol circuit into an OEO loop would allow to benefit simultaneously from the large bandwidth of the photonic components, and from the neuromorphic computing advantages. The dynamical state of the circuit Figure 1.25 (b) obeys the following Van der Pol dimensionless autonomous equation:

$$\ddot{x} - (\epsilon - x^2)\dot{x} + x = 0, \tag{1.11}$$

where ϵ is the dimensionless gain of the oscillator and x the dimensionless voltage. When we combine this filter with the optical part of the OEO where laser-diode make the conversion, it yields:

$$\ddot{x} - [\beta D(x_{T_D} - \vartheta) - x^2]\dot{x} + x = 0, \tag{1.12}$$

where, T_D is the dimensionless delay, β is the dimensionless gain, and ϑ the dimensionless offset value for diode nonlinearity. D is the dimensionless nonlinear transfer function of laser. For positive value of ϑ, we have periodic and chaotic dynamics in the system.

For a short time-delay, the term x_{T_D} do not affect greatly the dynamics of the system. For a low gain, it can be seen the quasi-sinusoidal oscillations after the Hopf bifurcation. As the gain is increased the harmonic behavior is observed. There is good agreement between numerical and experimental results. The main difference between the VDP oscillator and the VDP-OEO is that the oscillations in the latter case are asymmetric, with a skewness towards positive values. Along the same line, the transitions form negative to positive values are slower than those form positive to negative in the VDP-OEO, while both transitions are of equal duration in the classical VDP oscillator. For large delay ($T_D = 4$), the term x_{T_D} affects the dynamics of the system.

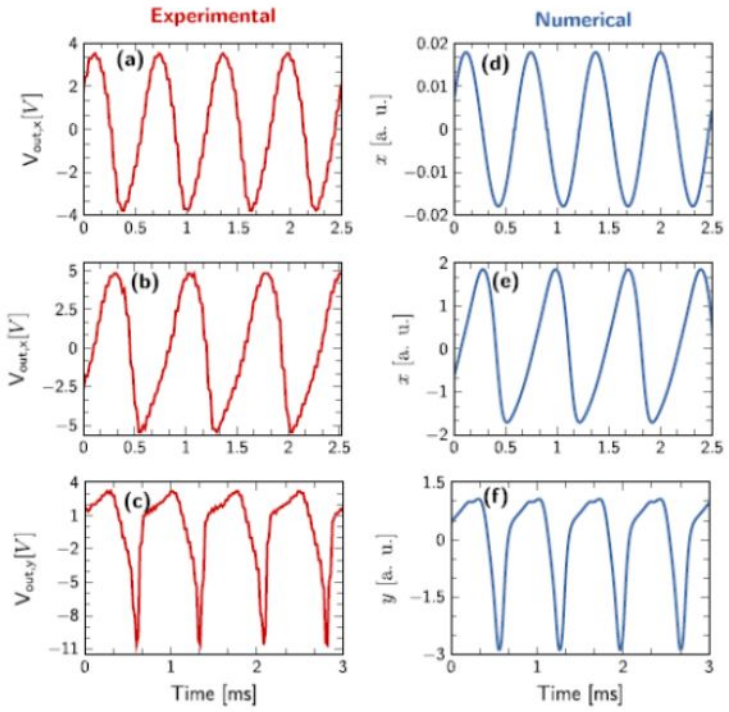

Figure 1.26: Experimental (left column) $V_{th} - V_{pol} = 1.314V$, $R = 10k\Omega$, $C = 10nF$, $T_D = 0.21\mu s$ and numerical (right column) timetraces of the simplest OEO. $\alpha = 0.1$, d for $\beta = 1.2$, e for $\beta = 2.2$, f for $\beta = 2.2$ [57].

We have a different type of attractors, including the chaos one. This complex dynamic is the result of the interplay of laser diode nonlinearity and VDP nonlinearity. We see a sudden jump of amplitude in the Hopf bifurcation point in $\beta = 0.405$ where x and y are quasi-sinusoidal oscillation confirm by Figure 1.28. The limit-cycle goes around twice before closing, as a consequence of a first period-doubling bifurcation. For $\beta = 1.55$, it is an infinite cascade of such period-doubling.

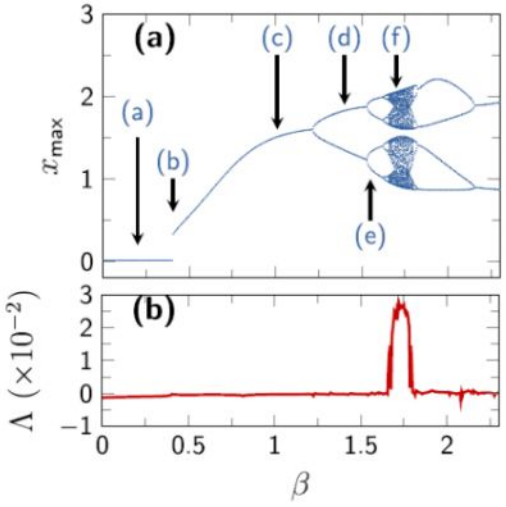

Figure 1.27: (a) Numerical bifurcation diagram of the simplified OEO where the variable x (maxima), (b) Lyapunov exponent of the system for $T_D = 4$ and $\vartheta = 0.1$. The label (a)-(f) indicate the dynamical regimes corresponding to the phase portraits of the Fig. 1.28.

The interplay between laser nonlinearity and the Van der Pol nonlinearity leads to some dynamics which were not still encountered in the classical OEO such as antimonotonicity, and period-doubling routes to chaos.

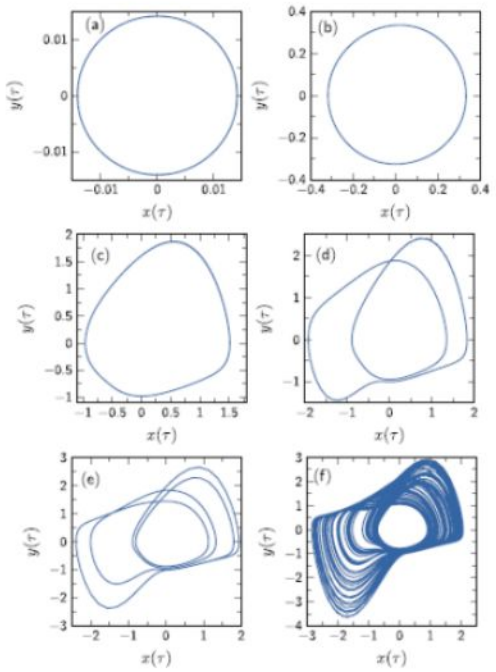

Figure 1.28: Numerical simulations of the dimensionless VdP-OEO for $T_D = 4$ and $\vartheta = 0.1$, for various gain values β in the space. (a) $\beta = 0.2$: quasi-sinusoidal oscillations with low amplitude. (b) $\beta = 0.405$: quasi-sinusoidal oscillations with high amplitude. (c) $\beta = 1.01$: Non-sinusoidal oscillations with high amplitude. (d) $\beta = 1.4$ period-two oscillations. (e) $\beta = 1.55$: period-four oscillations. (f) $\beta = 1.7$: chaos.

1.6 Problem statement of the work.

There is a lot of works that have studied the OEOs with a nonlinear filter. We want to provide some solutions to the problems generally encountered in chaos-based communication, random number generation, cryptographic, neurmorphic computing, and bioengineering where theses OEOs are used. A challenge remains that of finding electronic circuits as filters in optoelectronic oscillators whose implementation is simple compared to that of nonlinear filters such as the Van der Pol oscillator and the Colpitts oscillator. This research aims to obtain optoelectronic oscillators that are more versatile than the standard optoelectronic oscillator and which could generate higher frequency signals. New architectures can give rise to new dynamics that could inspire new technological applications.

Chembo et al. studied the experimental chaotic breathers in delayed electro-optical systems [21]. They showed that the phenomenon which occurred numerically in Ikeda model is confirmed experimentally. We see that as the gain increases, the relaxation, breathers, and chaos oscillations are observed. This work allowed to have an experimental and numerical confirmation of the standard oscillator. **Interested by this previous work, we extend a comparative study of a cubic-nonlinear bandpass filter-OEO**

numerically and experimentally to the standard optoelectronic oscillator.

Talla Mbé et al. proposed an experimental and theoretical study of a normal form method for the determination of the oscillations characteristic near the primary Hopf bifurcation in bandpass optoelectronic oscillator [21]. They showed that the amplitude and the frequency strongly depend on the normalized delay and the normalized gain. The analytical, numerical and experiment studies were in good agreement. **Interested by this work, we extend the method of the normal form to an OEO featuring the cubic-nonlinear filter to evaluate the effective amplitude of limit-cycle oscillations.**

In this thesis also propose a study based on the characterization by the normal form method near of Hopf primary bifurcation. Numerical, analytical, and experimental study of the limit-cycle oscillations near the primary Hopf bifurcation are propose. This thesis show how the amplitude of the oscillation growths with the normalized gain and the frequency decreases with the normalized time-delay. Because the laser diode has already been used successfully as electric-light convertor in the OEOs [10, 79], and has been generated strong dynamics to mimic many biological, bioengineering systems and reduce the number, the cost, power consumption of energy, and is very cheap, accessible, we have proposed a study of the laser diode pumps with a CNBPF in a loop. **Motivated by these previous works ([10,82]) based on laser diode conversion, we extend our study on an experimental and a numerical realization of an CN-OEO looped on the laser diode. The CNBPF is built analogically by the use of basic electronic components. We want to demonstrate that the CN-OEO evolve similarly to a standard OEO. However, the standard OEO evolves with a lower frequency of oscillation at the primary Hopf bifurcation compared to the CN-OEO even in the asymptotic case of large time-delays.**

1.7 Conclusion.

We have presented in this chapter a standard optoelectronic oscillator, a literature review on optoelectronic oscillators which use nonlinear filters, and the ones which perform laser and filter nonlinearities. This presentation has allowed us to highlight the problems of the thesis. The next Chapter will be devoted to theoretical, numerical, and experimental methods used to analyze the dynamical states of the devices proposed in this work.

Chapter 2

MATERIAL AND METHODOLOGY

2.1 Introduction

In the previous chapter, we posed a problem which was to propose other optoelectronic oscillators which are made with a nonlinear filter whose implementation is simple and which can operate in wide-band and narrow-band configurations. The goal of this chapter is to present the methods for solving this problem. Section 2.2 is reserved to the theoretical methods used to solve the integro-differential equations modeling the dynamics of the studied systems. The numerical methods will be given in section 2.3. In section 2.4, we will present the methods of calibrating the electronic and optical devices that will be use during the experiment and the last section will be devoted to the conclusion.

2.2 Mathematical formalisms and stability criteria

In this section, three mathematical formalisms are introduced. The first deals with the linear stability analysis of the dynamics of optoelectronic oscillators. The second deals with the characterization by the normal form of the delayed integro-differential equations, and the third formalism deals with intensity modulation by the laser in the optoelectronic oscillators.

2.2.1 Stability analysis for ordinary differential equations and delay differential equations

In general, the differential equations of optoelectronic oscillators with time-delay are under the form:

$$\frac{dX(t)}{dt} = F(X(t), X(t-T), \gamma) \tag{2.1}$$

where F a differentiable function, $X(t)$ et $X(t-T)$ are too vectors in $\Re^n$ ($X(t) = (x_1(t), x_2(t), ..., x_n(t), X(t-T) = (x_1(t-T), x_2(t-T), ..., x_n(t-T))$), and $T > 0$ is the time-delayed. To determine the fixed points, we solve the equation behind:

$$\frac{dX(t)}{dt} = 0\,, \tag{2.2}$$

The solutions of such equation are the fixed points and are under the form, $X = c^{te}$ so that $X(t) = X(t-T)$. To analyze the stability of the fixed points, one uses the perturbation method which consist to write the solution $X(t)$ under the form:

$$X(t) = X_0 + \delta X(t) \tag{2.3}$$

where $\delta X(t)$ is the small perturbation. The next step after determining the fixed point is the linearization of equation 2.1 around the fixed point and performing a truncation to order 1. It will allow us to obtain the variational equation yielding:

$$\frac{d\delta X(t)}{dt} = \frac{\partial F[X(t), X(t-T), \gamma]}{\partial X(t)}|_{X(t)=X_0}\delta X + \frac{\partial F[X(t), X(t-T), \gamma]}{\partial X_T(t)}|_{X(t)=X_0}\delta X_T \quad (2.4)$$

Consider J_1 et J_2, the jacobian matrices are defined by:

$$\begin{aligned} J_1 &= \frac{\partial F(X(t), X(t-T), \gamma)}{\partial X(t)}|_{X(t)=X_0} \\ J_2 &= \frac{\partial F(X(t), X(t-T), \gamma)}{\partial X_T(t)}|_{X(t)=X_0}\,, \end{aligned} \quad (2.5)$$

Let us consider $\delta X(t) = \delta X_0 e^{\lambda t}$, where δX_0 is an constant vector and have the same dimension with $X(t)$, and λ as eigenvalue of this system 2.4. This consideration permits to generate the eigenvalues equation of the system:

$$det(J_1 - \lambda I + e^{-\lambda T} J_2) = 0\,, \quad (2.6)$$

where$I$ is the unit matrix.

The eigenvalues, solution of the characteristic equation 2.6 can be either positive or negative real numbers, or complex conjugates.

- A fixed point is unstable if the real parts of the eigenvalues are positive.
- The fixed point is stable if the real parts of the eigenvalues are negative.
- It is neutral if the real roots are equal to zero.

The nature of the eigenvalues from solving the characteristic equation can be used to analyze the dynamic behavior of a system. Concerning OEOs, the fixed points and the eigenvalues depend on the parameter γ. It is noted that when the system evolves linearly or nonlinearly, the changing of the value of the parameter γ, can lead to carry significant qualitative changes in the properties of the system. This allows us to conclude that the study of fixed points and eigenvalues also makes it possible to analyze the dynamics of the system.

2.2.2 Characterization by the normal form of integro-differential equations with delay

The characterization by the normal form makes it possible to analyze the stability of the system according to the key parameters of the system considered. Nayfeh is the

one who developed the normal form method and we use the "center-manifold reduction" method to analyze the amplitude and the frequency of oscillations from the optoelectronic oscillators [95]. The first step consists of doing a limited Taylor expansion around the equilibrium points which are determined beforehand in order to obtain a differential vector equation with delay. It yields:

$$\dot{X} = \mathcal{L}X(t) + \mathcal{R}X_T + \mathcal{F}(X_T)\,, \tag{2.7}$$

With X as a vector which depends on the variables of the system. $\mathcal{L}$ and $\mathcal{R}$ the 2×2 matrices which contain the coefficients in front of the variables of the system and $\mathcal{F}$ a column vector which contains the nonlinear terms of the system.

To solve the equation (2.7), two time intervals must be considered: the interval taking into account the time-delay $[-T; 0]$ and the interval after the origin of times $[0; +\infty[$. Consider ς as the time in the first interval and t in the second interval, we can rewrite equation (2.7) in the form:

$$\frac{dX_{t(\varsigma)}}{dt} = \mathcal{A}X_{t(\varsigma)} + \mathcal{G}(X_{t(\varsigma)}), \tag{2.8}$$

where $X_{t(\varsigma)} = X(t + \varsigma)$ is a portion of the solution trajectory in the recent past. $\mathcal{A}$ is the linear operator with pure imaginary eigenvalue $i\omega_{_H}$ of the Hopf bifurcation point. $\mathcal{A}$ transforms a center subspace function $p(\varsigma)$ as follows:

$$\begin{aligned} \mathcal{A}p(\varsigma) &= i\omega_{_H} p(\varsigma) \\ &= \begin{cases} \frac{dp(\varsigma)}{d\varsigma} & \text{for} \quad -\nu \leq \varsigma \leq 0 \\ \mathcal{L}p(0) + \mathcal{R}p(-\nu) & \text{for} \quad \varsigma = 0. \end{cases} \end{aligned} \tag{2.9}$$

It is known that when $i\omega_{_H}$ is an eigenvalue of the Hopf bifurcation, its complex conjugate $-i\omega_{_H}$ is also an eigenvalue. Thus, to take into account both eigenvalues, we define the adjoint operator of $\mathcal{A}$, call $\mathcal{A}^*$ which also acts on another subspace function $q(\varsigma)$ as:

$$\begin{aligned} \mathcal{A}^*q(\varsigma) &= -i\omega_{_H} q(\varsigma) \\ &= \begin{cases} -\frac{dq(\varsigma)}{d\varsigma} & \text{for} \quad 0 \leq \varsigma \leq \nu \\ \mathcal{L}^*q(0) + \mathcal{R}^*q(\nu) & \text{for} \quad \varsigma = 0, \end{cases} \end{aligned} \tag{2.10}$$

where $\mathcal{L}^*$ and $\mathcal{R}^*$ are the adjoint of the operators $\mathcal{L}$ and $\mathcal{R}$, respectively. In equation (2.8), the expression of the vector $\mathcal{G}$ is:

$$\mathcal{G} = \begin{cases} 0 & \text{for} \quad -\nu \leq \varsigma \leq 0 \\ \mathcal{F} & \text{for} \quad \varsigma = 0. \end{cases} \tag{2.11}$$

In the theory of the center manifold reduction it requires that the subspace functions $p(\varsigma)$ and $q(\varsigma)$ satisfy the inner product:

$$< q, p >= \bar{q}(0)p(0) + \int_{-\nu}^{0} \bar{q}(\xi + \nu)R_H^* p(\xi)d\xi\,, \tag{2.12}$$

The "overline" stands for the complex conjugation. Since $X_t(\varsigma)$ must be finite, it is necessary to introduce a normalization condition such that $< q, p >= 1$ and $< q, \bar{p} >= 0$.

These inner products make it possible to define the values of the subspace functions $p(\varsigma)$ and $q(\varsigma)$. These functions determined, the next step is to decompose $X_{t(\theta)}$ into two components: the first one $\varrho(t)p(\varsigma) + \bar{\varrho(t)}\bar{p(\varsigma)}$ resting on the central subspace and the second $u_t(\varsigma)$ transverse to the center subspace is the infinite-dimensional component and satisfies $< p, u >= 0$ and $< \bar{p}, u >= 0$. Hence,

$$X_t(\varsigma) = \varrho(t)p(\varsigma) + \bar{\varrho(t)}\bar{p(\varsigma)} + u_t(\varsigma) \tag{2.13}$$

Substituting equation (2.13) into equation (2.8) and using the inner products yields a first order differential equation satisfied by ϱ. To solve this differential equation we must take the solution in the form:

$$\varrho(t) = z + k_{11}z^2 + k_{12}z\bar{z} + k_{13}\bar{z}^2 \tag{2.14}$$

This equation (2.14), as a solution form, replaced into equation (2.8) and the secular terms eliminated, we proceed by identifying the coefficients k_{11}, k_1, and k_{13}. The remaining non-secular terms will constitute the complex normal form of the system and will be given in differential equation satisfied by $\dot{z}$ ($\dot{z} \approx i\omega_H \mathrm{z}$). The variable z is linked to the complex amplitude of the limit-cycle oscillations by the relation: $z(t) = A(t)e^{i\omega_H t}$ which replaced in the differential equation satisfied by $\dot{z}$ will allow to have the complex normal form of the amplitude of the signal of the system:

$$\dot{A} = -\chi_1 A + \chi_2 \bar{A} \tag{2.15}$$

where χ_1 and χ_2 are complex coefficients resulting from the various developments. The solution of the Eq. (2.15), can be taken as $A = a(t)e^{i\varphi t}$. This solution form allow to have a first order differential equations in term of a and φ. These differential equations satisfied by a and φ will be used to know the fixed points of the system and we can analyze their stability. This last step makes it possible to have the amplitude a and the frequency φ of the limit-cycle oscillations analytically by using the method of center-manifold reduction of the normal form.

2.2.3 Intensity modulation by using the laser diode in an OEO: the limit of the low pumps of the laser diode

In this part, we are interested in the electrical-optical conversion in the limit of the low pumps of the laser diode [66]. Figure 2.1 permits to see different currents which feed the laser diode.

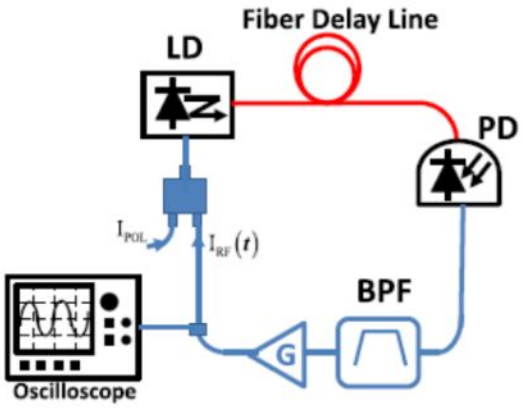

Figure 2.1: Experimental setup of direct modulation of the OEO. LD: laser diode, PD: photodiode, BPF: band pass filter, G: voltage variable attenuato [66].

The power of the signal from the laser $P(t)$ is a function of the current from the filter(I_{RF}) and the bias current (I_{pol}). These two electric currents allow us to have a threshold current (I_{th}):

$$I_{th} = I_{pol} + I_{RF} \tag{2.16}$$

The power of the signal from the laser $P(t)$ is a nonlinear function which is defined by the transfer function:

$$P(t) = \begin{cases} 0 & for\ I_{RF}(t) \leq I_0 \\ \mu[I_{RF}(t) - I_0] & for\ I_{RF}(t) > I_0, \end{cases} \tag{2.17}$$

The parameter $\mu = \eta_d h\nu$ is the laser conversion slope with η_d as the quantum efficiency, h the Planck constant, and ν the laser carrier frequency. The experimental value of the parameter μ in this thesis is $\mu = 0.21W/A$. In equation(2.17), $I_0 = I_{th} - I_{pol}$. Taking into account the time-delay experienced by the optical signal during its flow inside the delay line, the voltage provided by the photodiode is related to such retarded optical signal as follows:

$$V_{\text{in}} = KSP(t - T_D), \tag{2.18}$$

where K is a dimensional factor standing for the overall losses (electrical and optical) in

the feedback loop. This voltage will be use as input of the CNBPF.

2.3 Numerical methods

The mathematical treatment of some nonlinear that describe physical systems is not always easy. The analytical method which passes by the study of the stability of the fixed points allows us just to approximate the dynamic behavior of the optoelectronic systems. This assessment is not always satisfactory, that is why we also request numerical approximations for a better analysis of the system or confirmation of the analytical study. In this work, the systems are described by ordinary differential equations (ODE), differential equations with time-delay (DET), and nonlinear algebraic equations which lead to some developments. In order to have more information on the dynamical behaviour of the systems obtained in this work, one something needs numerical methods such as the Runge-Kutta methods for the ODEs and the DETs [101], and the bisection method for the nonlinear algebraic equations.

2.3.1 Runge-Kutta Methods

2.3.1.1 ODEs case

The Runge-Kutta method was first developed by the German mathematician C. Runge in 1894 and improved by M. W. Kutta in 1901. It is one of the most widely used numerical simulation algorithms for solving ordinary differential equations and differential equations with time-delay. This method is popular because it is a more stable and efficient numerical method [101, 102]. Runge-Kutta method behaves three orders knowing: the second-order (RK2), the third-order (RK3) and the fourth-order (RK4). The method used here is the fourth order Runge-Kutta method. Consider a physical system described by the first-order ordinary differential equation:

$$\dot{y} = f(t, y)\,, \tag{2.19}$$

with the initial condition $y(t_0) = y_0$. Using Runge-Kutta's method for solving the equation, we can approximate the numerical solution. the solution $y_{i+1} = y(t + h)$ is giving by (2.20) where h is the integration step.

$$y_{i+1} = y_i + \frac{1}{6}(K_1 + 2K_2 + 2K_3 + K_4) + O(h^5) \tag{2.20}$$

where the terms $K_{1,2,3,4}$ are given by:

$$\begin{aligned} K_1 &= hf(t,y) \\ K_2 &= hf(t+h/2, y+K_1/2) \\ K_3 &= hf(t+h/2, y+K_2/2) \\ K_4 &= hf(t+h, y+K_3)\,. \end{aligned} \tag{2.21}$$

The choice of initial condition y_0 is important. This choice is decisive in order to be able to calculate the other values. In the case of an integro-differential equation in the form

$$\dot{y} = f(t,y) + a\int_{t0}^{t} y(s)ds \tag{2.22}$$

with initial condition $y(t_0) = y_0$, where a is a parameter that does not depend on t and on y, we decompose this equation into two ordinary differential equations by setting a new variable

$$\begin{aligned} \dot{u} &= ay(t) \\ \dot{y} &= f(t,y) + au = g(t,y,u) \end{aligned} \tag{2.23}$$

where $g(t,y,u)$ is the new function. Consider that $z(t,y) = ay(t)$, the solution of that equation will be given by the Runge-Kutta method's:

$$u_{i+1} = u_i + \frac{1}{6}(L_1 + 2L_2 + 2L_3 + L_4) + O(h^5) \tag{2.24}$$

$$y_{i+1} = y_i + \frac{1}{6}(K_1 + 2K_2 + 2K_3 + K_4) + O(h^5)\,, \tag{2.25}$$

where the terms $K_{1,2,3,4}$ and the terms $L_{1,2,3,4}$ are given by:

$$\begin{aligned} K_1 &= hg(t,y,u) \\ K_2 &= hg(t+h/2, y+K_1/2, u+L_1/2) \\ K_3 &= hg(t+h/2, y+K_2/2, u+L_2/2) \\ K_4 &= hg(t+h, y+K_3, u+L_3) \\ L_1 &= hz(t,y) \\ L_2 &= hz(t+h/2, y+K_1/2) \\ L_3 &= hz(t+h/2, y+K_2/2) \\ L_4 &= hz(t+h, y+K_3)\,. \end{aligned} \tag{2.26}$$

The software used here to perform this scientific calculation is Fortran 90 and Matlab.

2.3.1.2 DETs case

For solving differential equations with time-delay, the most stable and suitable numerical solving method is the second order Runge-Kutta method (RK2). Let us consider a differential equation with delay given by:

$$\dot{x} = f[t, x(t), x(t-T)]\,, \tag{2.27}$$

with $t \in [-T, 0[$, T as time-delay. The initial condition is a constant function in a finite interval. Considering $N_T = \frac{T}{h}$ and $t = ih$ where i is an integer and h is the step of integration, the solution of that equation is given by:

$$X_{i+1} = X_i + \frac{1}{2}(k_1 + k_2) + O(h^3)\,, \tag{2.28}$$

with

$$\begin{aligned} k_1 &= hf(ih, X(i), X(i - N_T)) \\ k_2 &= hf((i+0.5)h, X(i) + k_1, X(i - N_T + 1))\,, \end{aligned} \tag{2.29}$$

which are the second order Runge–Kutta coefficients with delay.

2.3.2 Bisection method for solving nonlinear algebraic equations

The search for fixed points in this thesis has generated nonlinear equations for which it was important to find the roots. To determine the roots of the function $f(x)$ we solve:

$$f(x) = 0\,. \tag{2.30}$$

When $f(x)$ is a polynomial function that does not correspond to a known form, the bisection method can be used. It consists of dividing the search interval into two equal parts and this repeatedly, until the width of the interval is comparable to the desired precision ε on the position of root. Consider f as a monotonic function on the interval $[x_0; y_0]$ such as $f(x_0)f(y_0) < 0$; there is one and only one solution or root included in this interval.

The resolution algorithm is as follows: We calculate first $f(\frac{x_0+y_0}{2})$ and verified:

- if $f(\frac{x_0+y_0}{2})f(x_0) < 0$. we define a new framing of the root by the couple (x_1, y_1):

$$x_1 = x_0 \quad \text{et} \quad y_1 = \frac{x_0 + y_0}{2}\,. \tag{2.31}$$

- if $f(\frac{x_0+y_0}{2})f(x_0) > 0$. we define a new framing of the root by the couple (x_1, y_1):

$$y_1 = x_0 \quad \text{et} \quad x_1 = \frac{x_0 + y_0}{2}. \tag{2.32}$$

After several iterations, we obtain a sequence of couples (x_n, y_n) such that the desired precision $e_n = y_n - x_n$ verifies the relation:

$$e_{n+1} = \frac{e_n}{2} \tag{2.33}$$

where $e_0 = \frac{y_0 - x_0}{2}$. the tolerance e which represents the precision to which we want to obtain the root permits to calculate the number of iterations n to be carried out yields:

$$n = \ln\left(\frac{|y_0 - x_0|}{e}\right) \tag{2.34}$$

The choice of the precision requires some precautions.

2.4 Presentation of the experimental device

The goal is to present the material used in the experimental study of the optoelectronic oscillator in this thesis. The overall experimental device used is shown in Figure 2.2. It is made up of many components which the description is made here.

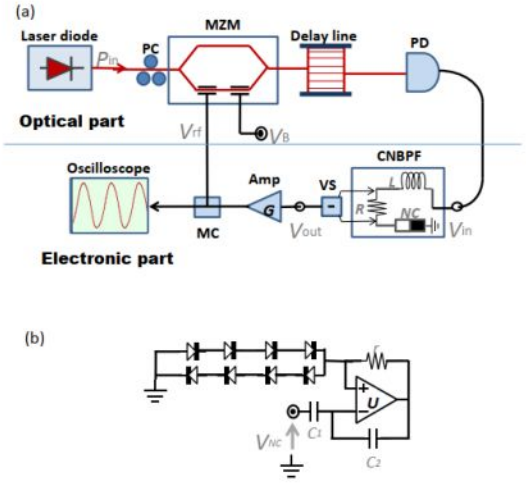

Figure 2.2: (a) Experimental setup of cubic-nonlinear optoelectronic oscillator. (b) Inner structure of the nonlinear capacitor [68, 69]. PC: Polarization Controller; MZM: MachZehnder Modulator; V_B is the offset phase control voltage; PD: Photodiode; CNBPF: Cubic-Nonlinear Band-Pass Filter; VS: Voltage Subtractor; Amp: RF amplifier; MC: Microwave Coupler.$L = 0.1\,m$H, $r = 300\,\Omega$, $C_1 = 270\,p$F, $C_2 = 9.15\,n$F

The experimental devices in the laboratory is presented in Figure2.3.

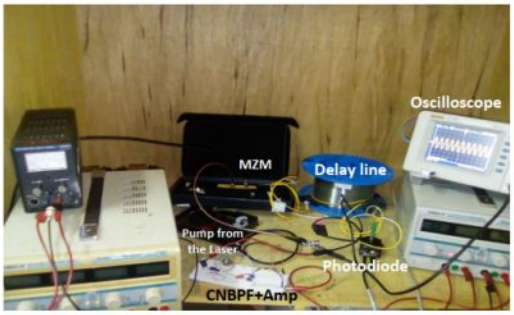

Figure 2.3: Experimental devices in the laboratory. One can identify different components cited in the text.

2.4.1 Cubic-nonlinear band-pass filter (CNBPF)

The CNBPF is implemented using two capacitors $C_{1,2}$, two resistors (r, R), an operational amplifier U (type $LF356$), a mixed assembly of eight simple junction diodes (type $IN400X$), and one coil L. The thermal voltage of these junction diodes is $V_T = 25\ mV$, the number of junction diodes in series is $n = 4$, and the inverse saturation current is $I_s = 5\ \mu A$. The goal of this part is to present each component.

2.4.1.1 Operational amplifiers (OPAMP) and operations using OPAMP

a) Operational amplifiers (OPAMP)

The operational amplifier is a fundamental element present in a very large number of electronic devices. It is an electronic amplifier which strongly amplifies an electrical potential difference present at its inputs. We use the LF356 series to realize the design of the CNBPF. It has eight pins and each of the eight pins is a small electric wire. Its symbol is shown in Figure 2.4. The pin marked NC is useless: NC means "Not Connected". Figure 2.5 is the electronic diagram of an OPAMP.

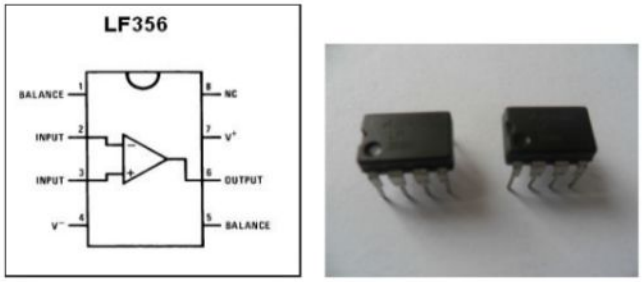

Figure 2.4: Operational amplifier LF356N.

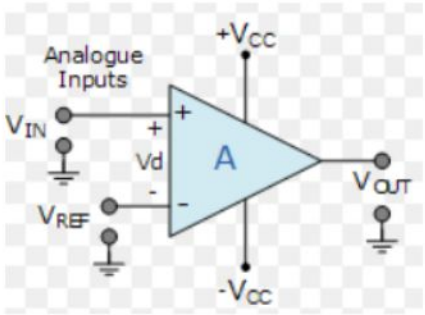

Figure 2.5: Electronic diagram of an OPAMP.

The way that the operational amplification is associated with resistors and capacitors it can perform many mathematical operations such as inversion, summation, derivation, and integration of the input signal.

b) Operations using OPAMPs

The association of the resistors and capacitor to the operational amplifier gives the following mini circuits presented in Figure 2.6, which have well defined roles.

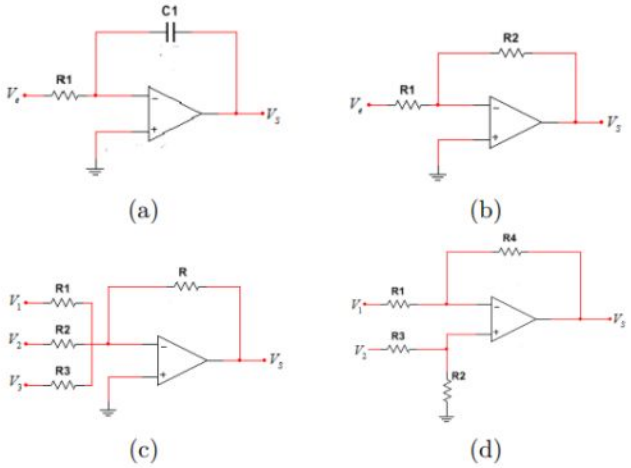

Figure 2.6: Some basic operations using OPAMP: (a) integrator; (b) inverter amplifier; (c) summator; (d) subtractor.

- **The integrator**: it is realized thanks to an OPAMP associated with a resistor and a capacitor. The circuit of an integrator is shown in Figure2.6, where R_1 is resistance, C_1 the capacity, V_e the input voltage and V_S the output voltage. No current enters in OPAMP which is considered as ideal. The expression of the voltage is given as follow:

$$V_S = -\frac{1}{R_1 C_1} \int V_e(t) dt \tag{2.35}$$

- **The voltage inverter amplifier**: it is a voltage amplifier which takes any signal at the input and invert it at the output. The expression of the voltage is given below:

$$V_S = -\frac{R_2}{R_1}V_e \tag{2.36}$$

Other operations are analog summators and subtractors whose role is to sum and subtract the input voltages respectively. The expressions of their output voltages are given by equations. (2.37) and (2.38) below:

$$V_S = -R\left[\frac{V_1}{R_1} + \frac{V_2}{R_2} + \frac{V_3}{R_3}\right] \tag{2.37}$$

$$V_S = \frac{(R_1 + R_4)}{R_1}\frac{R_2}{(R_3 + R_2)}V_2 - \frac{R_4}{R_1}V_1 \tag{2.38}$$

To constitute the CNBPF, we use only the subtractors.

2.4.1.2 Resistors and capacitors.

To model the nonlinear filter (CNBPF), we also used some resistors and some capacitors. These electrical components are shown in Figure 2.7.

(a) (b)

Figure 2.7: (a) Resistors and (b) Capacitors.

The role of the resistor is to limit the intensity of the electric current in a circuit. It is a passive dipole. A capacitor, meanwhile, smooths and stabilizes power supplies, filters and absorbs certain parasitic signals. It can increase the quality of signal transmission. It can also store electricity to ensure or facilitate the starting of a circuit by yielding the stored electricity.

2.4.1.3 Diodes and coils.

Diodes and coils are other elements that enter into the constitution of the CNBPF. They are presented in Figure 2.8.

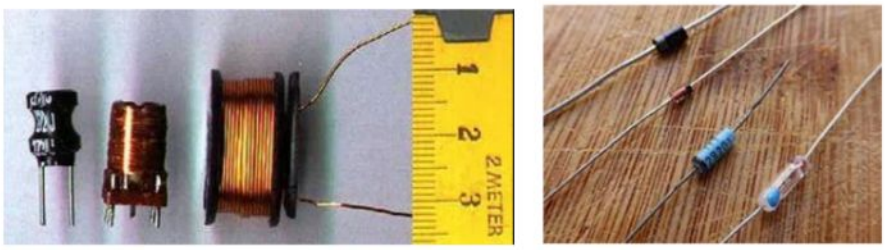

(a) (b)

Figure 2.8: (a) Coils and (b) diodes.

A diode is a semiconductor device that primarily acts as a one-way switch of current. It allows current to flow easily in one direction, but severely restricts current from flowing in the opposite direction. The induction coil on the other hand, is an element that stores energy in the core in the form of a magnetic field, so it converts the energy of the electric current into energy of the magnetic field or vice versa. A change in the current flowing through the winding generates an electromotive force in the direction that counteracts that change.

2.4.2 Stabilized DC power supply and Rigol oscilloscope.

In order to read information on the signal from the CN-OEO, measurement equipment was needed to carry out this experimental work. We can cite among others:

- a stabilized DC power supply (PS2303) with two variable outputs (0-30 V) and a fixed output of 12 V (see Figure2.9(a)), used to bias our electronic components that are the OPAMPs;
- a Rigol oscilloscope of type DS1102E, of bandwidth 100 MHz (see Figure2.9(b)) which allowed us to visualize the different signals from the CN-OEO when the value of the feedback gain was varied.

(a) (b)

Figure 2.9: Some additional materials used: (a) DC power supply; (b) Rigol oscilloscope.

2.4.3 Laser diode.

In the feedback loop that constitutes the simplified CN-OEO, we encounter the laser diode. It is a semiconductor laser with distributed feedback (see Figure 2.10). The optical power and wavelength of this laser is controlled by the electric currents. It emits a monochromatic beam in the infrared range, with a rectilinear polarization and wavelength $\lambda = 1550$ nm. Improper handling of the diode can easily damage it. It is important to point out that during certain manipulations, in order to control the power supply of the laser diodes, the devices such as the *"Laser Diode Controller"* (reference: LDC 200 C) and the "Temperature Controller" (reference: TED 200) control the injection current and temperature. An example of laser diode is presented in Figure 2.10

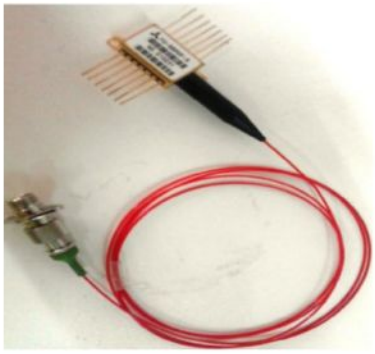

Figure 2.10: Distributed feedback laser diode

The current-power characteristics determining the threshold of the laser used is given by the Figure 2.11. The experimental threshold of the current of the distributed feedback laser diode is approximative the same with the constructor one(10 mA)

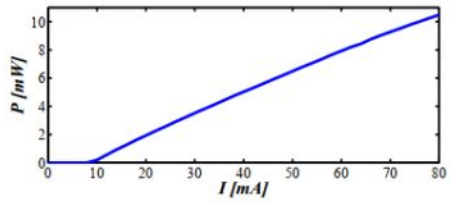

Figure 2.11: The current-power characteristics of the laser.

2.4.4 Polarization controller

Another component that comes after the laser diode is a polarization controller shown in Figure 2.12.

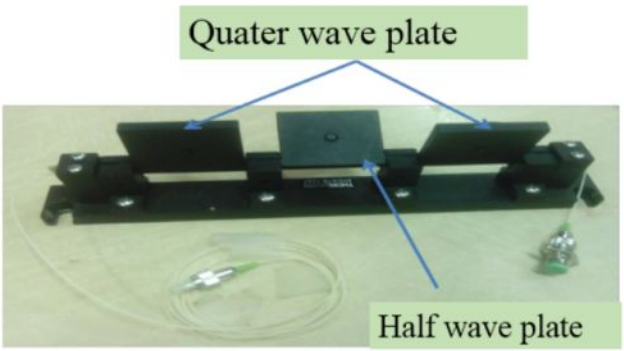

Figure 2.12: Polarization controller.

This device consists of three cascaded wave plates that can be turned manually. The first quarter-wave plate is oriented to transform the incident elliptical polarization into a linear polarization. The second half-wave plate transforms this linear polarization into another linear polarization. The last quarter-wave plate transforms linear polarization into elliptical polarization which is usable at the output.

2.4.5 Electro-optical modulator.

The modulation of the signal is done at the level of the Mach-Zehnder, which presents a $\cos^2$ nonlinearity. This Mach-Zehnder is made with the Lithium Niobate $LiNO_3$ and is based architecture composed of two head-to-tail "Y" junctions linked together by two straight guides which constitute the arms of the interferometer. A relative phase shift result between the arms of the Mach-Zehnder. The internal structure of Mach-Zehnder modulator is shown in Figure 2.13. The Mach-Zehnder (MZ) interferometer has two separate electrodes including the bias or DC electrode and the RF electrode for wave modulation. The MZ modulator is characterized by its static transfer function with gave the output optical power Pout as a function of the voltage V (t) applied to the electrodes. If Pin is the optical power input of the Mach-Zehnder, his relation with the output is giving by:

$$P_{out} = P_{in} \cos^2 \left[\frac{\pi V(t)}{2V_{\pi RF}} + \varphi \right], \tag{2.39}$$

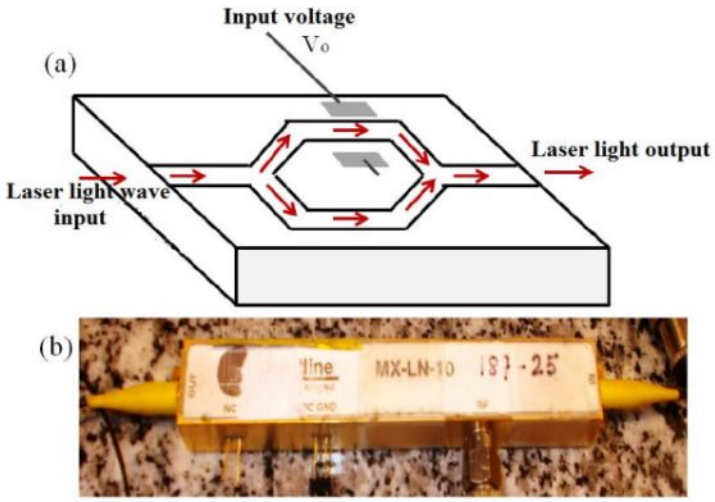

Figure 2.13: (a) Electro-optical modulator integrating phase modulation, (b) MachZehnder image.

where φ is the phase at the origin which is function of the voltage V_B applied to the bias (DC electrode) and the half-wave voltage $V_{\pi,DC}$ at this electrode, according to:

$$\varphi = \frac{\pi V_B}{2V_{\pi DC}}\,. \tag{2.40}$$

Mach-Zehnder modulator can generate a high optical power and produces the wave which can have more than 100 GHz frequency. They are more used in optical communication.

2.4.6 The optical fiber

The optical fiber is ideal for transmitting the optical information because it limits the energy losses. This fiber create a time-delay in the feedback loop. The parts of this fiber are indicated in Figure 2.14.

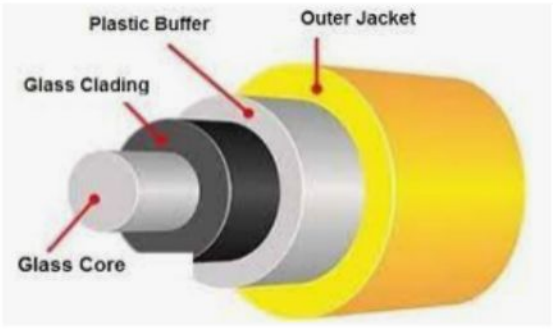

Figure 2.14: The structure of the optical fiber

- The glass core: this zone is made with a glass with a refractive index n_1. It allows to guide the light which propagates along the fiber.
- The glass clading: this area is also made with a glass with a refractive index $n_2 \neq n_1$. It surrounds the glass core to better confine the light thanks to the phenomenon of total reflection.
- the protection: it is a mechanical protective coating generally in polyvinyl chloride (PVC).

In this work, the wavelength of the laser used is $\lambda = 1550nm$. The longer of the fiber increases the time-delay. Indeed, the time-delay in the optical fiber is proportional to the refractive index of the glass core n1, the length of the fiber used L, and inversely proportional to the speed of light, according to:

$$T = \frac{nL}{c} \tag{2.41}$$

In order to avoid losses of light when the transmission is running, it is preferable to use a long optical. This is the reason why we used a fiber of 656 meters in the CN-OEO. Figure 2.15 presents the optical fiber uses in this these.

Figure 2.15: Optical fibers used to constitute CN-OEO.

Note that for a roll of 656m is use in this these. The time-delay is $T_D = 3.29\mu s$. the optical fiber provides the link between the electrical-to-optical convertor and photodiode.

2.4.7 Photodiode

The optical output chain is made with a photodiode which permits the conversion froms optical signal to electrical signal. The one we use in this work is the PDA10CF. It is an amplifier detector InGaAs type. This detector can detect the signal which the wavelength varying within 700 âĹŠ 1800 nm. His output impedance is 50Ω for 5 V voltage. It is presented in Figure 2.16

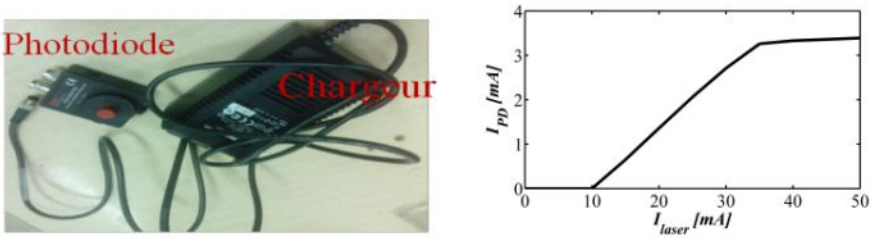

Figure 2.16: Optical fibers used to constitute CN-OEO.

The choice of this photodiode is motivated by the fact that his sensibility is near of 1 for the wavelength of the laser diode used in this thesis ($\lambda = 1550$ nm). The intervention of the photodiode in the optoelectronic oscillator's equation remain of the sensibility.

2.5 Conclusion

The aim of this chapter was to present the experimental setup and devices of CN-OEO, the summary of the mathematical methods which make it possible to analyze the stability of this oscillator by using the differential equations generated by the said oscillator. The numerical methods which have made it possible to successfully explore the dynamics of the CN-OEO was also presented. In the first part, analytical methods such as the perturbation method to analyse the stability of the fixed points, the normal form reduction and modulation of intensity by laser were presented. Then the numerical methods for the simulation of DETs were presented. Finally, we have presented the electronic and optical components necessary for the construction of CN-OEO, as well as the equipment used to build the devices. All of these methods (numerical and experimental) will be used in Chapter 3 which is devoted to the presentation of the main results of this thesis.

Chapter 3

RESULTS AND DISCUSSION

3.1 Introduction

We have specified in the previous chapters that the nature of the filter influences the dynamics of the optoelectronic oscillator. The filter may be linear in response as it may be nonlinear response. We have also specified that an intensity modulation can be achieved by using a diode laser instead of a phase or amplitude modulator. In this chapter, we will present and discuss the results obtained in our thesis. Section 3.2 will be devoted to the study of the dynamics of the optoelectronic oscillator using a cubic nonlinear bandpass filter (CNBPF) (CN-OEO). In this part, we will present the experimental device in order to establish the equation of the dynamics liking the parameters of the system. Next, we will examine the influence of the control oscillator parameters on the stability and the dynamics of the system. Section 3.3 will be reserved to the characterization using the normal form of this delayed-system. This part addresses a deeper dynamical characterization of that CN-OEO in term of key parameters such as the strength of the feedback gain, the time delay, the offset phase, and the cubic nonlinear term. Section 3.4 will perform the simplified benchmark of the CN-OEO. We will show that as in the simplest OEO, the dynamic essentially exhibits limit cycle oscillation in two kinds: quasi-sinusoidal and slow-fast oscillation but rather with higher frequency. Finally, Section 3.5 will be devoted to the conclusion.

3.2 Dynamics of an OEO which use the CNBPF

3.2.1 Model description and time-delayed model to investigate the complex dynamical behavior

This section will be divided in three main parts. We will first introduce the model description, and secondly propose a time-delayed model to investigate its complex dynamical behavior. In the last case, a description of the mathematical model of the oscillator highlighted will be presented.

3.2.1.1 Model description

The experimental setup of the cubic-nonlinear optoelectronic oscillator (CN-OEO) is presented in Figure 3.1 and described as follows: A polarized light of power P_{in} delivered by a telecommunication continuous-wave laser diode (with a wavelength equal $\lambda_L \simeq 1.55\mu m$) is modulated with a Mach-Zehnder modulator (MZM) whose half-wave voltages are $V_{\pi RF} = 3.8V$ and $V_{\pi DC} = 5V$. The modulated light is retarded with an optical delay line resulting in a time-delay equal to $T_{_D} = 3.28\mu$s, before being converted to an electrical signal with a photodiode (PD) of responsivity $S = 4.75V/mW$. The electrical signal generated by the photodiode V_{in} passes through a cubic-nonlinear band-pass filter

(CNBPF) which outputs V_{out} and in turn is suggested to an amplification before being re-injected into the RF electrode of the MZM. It can be noticed that the CNBPF is made of a resistor R, a coil L, and a nonlinear capacitor NC. This latter is constructed with an operational amplifier U (type LF356), two capacitors $C_{1,2}$, one resistor r, and a mixed assembly of eight simple junction diodes (type IN400X) and whose characteristics are the thermal voltage $V_T = 25$ mV, the inverse saturation current $I_s = 5$ μA (see Figure 3.1 (b)). A picture of the whole experimental setup in the laboratory is displayed in Figure 3.2.

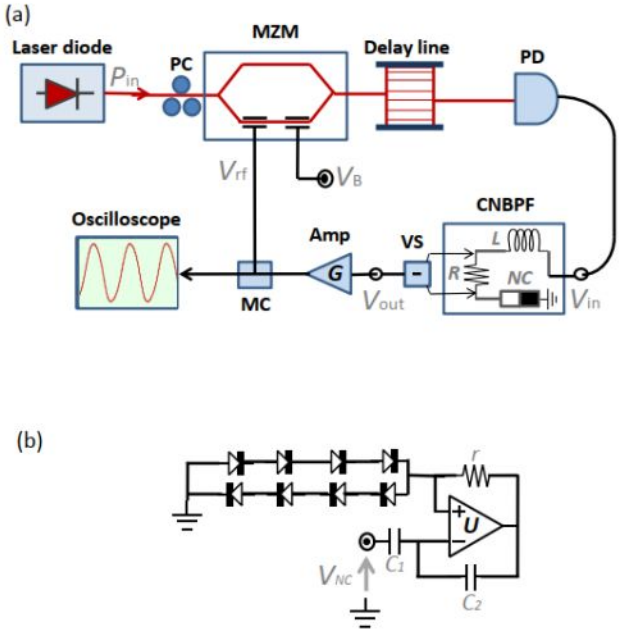

Figure 3.1: Experimental setup of cubic-nonlinear optoelectronic oscillator [**?**]. (b) inner structure of the nonlinear capacitor [68, 69]. PC: Polarization Controller; MZM: Mach-Zehnder Modulator; V_{B} is the offset phase control voltage; PD: Photodiode; CNBPF: Cubic-Nonlinear Band-Pass Filter; VS: Voltage Subtractor; Amp: RF amplifier; MC: Microwave Coupler. $L = 0.1\,m$H, $r = 300\,\Omega$, $C_1 = 270\,p$F, $C_2 = 9.15\,n$F.

3.2.1.2 Time-delayed model to investigate the complex dynamical behavior

The electronic part of the oscillator consists of a CNBPF. Given $V_{\text{in}}(t)$ the input voltage of the CNBPF circuit, and $V_{\text{out}}(t)$ the output voltage. The relation giving $V_{\text{in}}(t)$ according to $V_{\text{out}}(t)$ is established according to the Kirchhoff laws relating to the voltages.

The output voltage $V_{\text{out}}(t)$ of the CNBPF is related to the input $V_{\text{in}}(t)$ by:

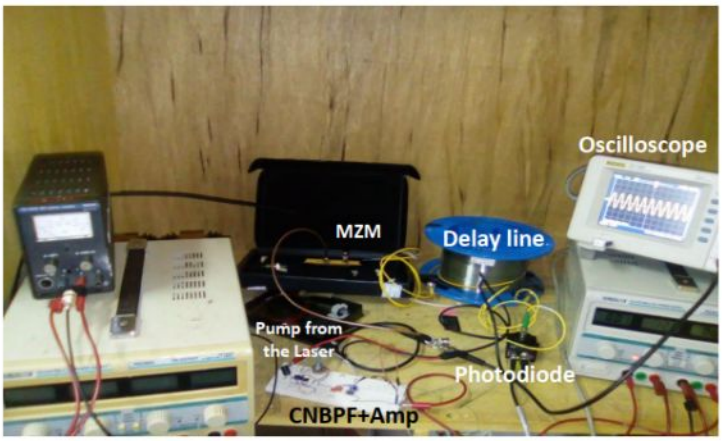

Figure 3.2: Experimental devices in the laboratory. One can identify different component cited in the text.

$$V_{\text{in}}(t) = \frac{L}{R}\frac{dV_{\text{out}}(t)}{dt} + V_{\text{out}}(t) + V_{\text{NC}}(t)\,. \tag{3.1}$$

$V_{\text{NC}}(t)$ is the voltage yields to a nonlinear capacitor. The application of Kirchhoff laws permits to evaluate the voltage across such a nonlinear capacitor which is a cubic-polynomial of the charge

$$q = \frac{1}{R}\int_0^t V_{\text{out}}(s)\,ds \tag{3.2}$$

of the series capacitor, and yields the relationship [68]:

$$V_{\text{NC}}(t) \;=\; \frac{1}{R}\left(\frac{1}{C_1} - \frac{nV_T}{2rI_sC_2}\right)\int_0^t V_{\text{out}}(l)dl + \frac{nV_T}{48(rRI_sC_2)^3}\left(\int_0^t V_{\text{out}}(s)\,ds\right)^3\,, \tag{3.3}$$

where t is the time.

Using equations. (3.3) and (3.1), and the usual closure relationships of broad bandpass optoelectronic oscillators [21], the system presented in Figure 3.1(a) obeys the following integro-differential delayed equation:

$$x+\tau\frac{dx}{dt}+\frac{1}{\theta}\int_0^t x(s)\,ds+\eta\left(\int_0^t x(s)\,ds\right)^3 = \beta\{\cos^2[x(t-T_D)+\phi]\}, \tag{3.4}$$

where $x = \pi V_{\text{out}}(t)/2V_{\pi\text{RF}}$ is the dimensionless dynamical variable of the system. According to equation. (3.4), the cubic-nonlinear band-pass filter is characterized by three time scales which are the high cut-off time τ, the low cut-off time θ, and the nonlinearity time

scale $\sqrt[3]{1/\eta}$ that are explicitly defined via

$$\tau = L/R \tag{3.5}$$
$$\theta = R\left[(1/C_1) - (nV_T/2rI_sC_2)\right]^{-1} \tag{3.6}$$
$$\eta = nV_TV_{\pi\mathrm{RF}}^2/\left[12(rRI_sC_2)^3(\pi G)^2\right]. \tag{3.7}$$

Therefore, adding the delay T_D confers to our CN-OEO a novel approach to implement a four-time scales OEO. The other parameters are the normalized loop-gain $\beta = \pi\kappa SGP_{\mathrm{in}}/2V_{\pi\mathrm{RF}}$ and the offset phase $\phi = \pi V_{\mathrm{B}}/2V_{\pi\mathrm{DC}}$. Throughout this thesis, except the tunable parameters G and P_{in}, the values of other parameters are kept compatible with the experimental set-up. They are set to $L = 0.1$ mH, $R = 2.5$ kΩ, $r = 300$ Ω, $C_1 = 270$ pF, $C_2 = 9.15$ nF, and $T_D = 3.29$ μs.

In order to facilitate the dynamical analysis, it is preferable to recast equation (3.4) under the form of a flow of first-order coupled delay differential equations. For this purpose, we introduce the new variable

$$y = -\frac{1}{\theta}\int_0^t x(s)\,ds \tag{3.8}$$

and the dimensionless time $\nu = t/\theta$. Equation (3.4) is then transformed into a slow-fast system with x as the fast variable while y is the slow variable [10]:

$$\varepsilon\frac{dx}{d\nu} = -x+y+\rho y^3+\beta\cos^2[x_\sigma+\phi] \tag{3.9}$$
$$\frac{dy}{d\nu} = -x\,. \tag{3.10}$$

The small quantity $\varepsilon = \tau/\theta = 9.7\times10^{-4}$ is the cut-off times ratio, $\sigma = T_D/\theta = 8\times10^{-2}$ represents the normalized delay so that $x_\sigma = x(\nu-\sigma)$ being the time-delay variable. The parameter $\rho = \eta\theta^3 = 6.4\times10^4$ stands for the cubic-nonlinear parameter.

In our case of study, the dynamics of the CN-OEO amounts to determining its dynamic behavior under the effect of feedback gain β, the normalized time-delay ν, and the cubic nonlinear parameter η. It is important to study the stability of the system by the method of fixed points and bifurcations.

To determine the equilibrium points of the amplitude of the signal which comes from the CN-OEO, we stand the points which represent amplitude to zero. Indeed, the equilibrium point of the set of equations. (3.9) and (3.10) is (x_0, y_0) such as, $x_0 = 0$ and y_0 being the real root of the third-order polynomial

$$\rho y_0^3+y_0+\beta\cos^2\phi = 0, \tag{3.11}$$

which is nontrivial if β or ϕ is different from 0 or $\pi/2$ (mod $[2\pi]$), respectively. It is

important to mention that y_0 is real and unique since ρ and β are positive quantities.

In order to study the stability of these fixed points, the perturbation method is used. The process of this method yields a characteristic eigenvalue equation which solutions being conjugate complexes. The stability of that equilibrium point can be investigated through the eigenvalues equation

$$\lambda^2+\frac{1}{\varepsilon}\left(1+\gamma e^{-\lambda\sigma}\right)\lambda+\frac{1}{\varepsilon}\left(1+3\rho y_0^2\right)=0\,, \tag{3.12}$$

where $\gamma=\beta\sin(2\phi)$ is the effective normalized gain. Limit-cycle oscillation might occur through a Hopf bifurcation if the eigenvalues become pure imaginary values ($\lambda=\pm i\omega$), with ω being the frequency of the corresponding limit-cycle which satisfies the following transcendental equation

$$\varepsilon\omega^2+\omega\,\tan(\omega\sigma)-\left(1+3\rho y_0^2\right)=0\,, \tag{3.13}$$

while the effective normalized gain γ rather satisfies

$$\gamma\,\cos(\omega\sigma)=-1\,. \tag{3.14}$$

In the approximation of small delay (small σ), the solutions of equations. (3.13) and (3.14) computed with an excellent precision give

$$\omega = \omega_{\rm sd}\sqrt{1+3\rho y_0^2}\,, \tag{3.15}$$

$$\gamma = -1+\frac{1}{2}\left(\frac{1+3\rho y_0^2}{\varepsilon+\sigma}\sigma^2\right)\,. \tag{3.16}$$

Here,

$$\omega_{\rm sd}=1/\sqrt{\varepsilon+\sigma} \tag{3.17}$$

represents the frequency of the limit-cycle for the standard OEO, that is the one with a linear band-pass filter that does not feature the cubic-term in equation. (3.4). We notice that from equations. (3.15) and (3.17), it clearly appears that the frequency of the limit-cycle oscillations of our CN-OEO is greater than the one displayed by a standard OEO for the same values of parameters. The numerical simulations and the experimentally ones will allows us to confirm theses analytical results.

3.2.2 Numerical and experimental simulations to approximate the dynamics of CN-OEO

The first numerical simulation which allows us to explore the dynamics of the CN-OEO is the Hopf bifurcation diagram. It permits to see the general behavior of the system as the normalized feedback gain increases. The comparison of the CN-OEO and the standard OEO, shows that the threshold of the effective normalized gain is not considerably affected by the cubic-nonlinear term since $\gamma \simeq -1$ as witnessed by the bifurcation diagram of Figure 3.3 (a), showing the evolution of the amplitude as the effective normalized gain increases. One can note that only fixed point, limit-cycles, and chaos are preserved. Indeed, for $|\gamma| < 1$, the fixed point $x_0 = 0$ dominates the dynamics of the system. From $|\gamma| = 1$, limit-cycle oscillations occur through a Hopf bifurcation and remain dominant for a long range of $|\gamma|$. When $|\gamma|$ is further increased, the limit-cycle disappears to give place to chaos. These transitions are emphasized by the corresponding largest Lyapunov exponent (Figure 3.3 (b)) defined as

$$\Lambda = \lim_{t \to +\infty} \frac{1}{t} \ln \left[\frac{|\delta x(t)|}{|\delta x(t_0)|} \right] , \tag{3.18}$$

with $\delta x(t)$ being a linear perturbation of the system [57]. The Lyapunov exponent Λ is known to be a positive quantity for chaotic behavior and negative or zero otherwise. It is shown from both figures that the bifurcation diagram and the largest Lyapunov exponent indicate the same window of dynamical behaviors for the chosen parameters.

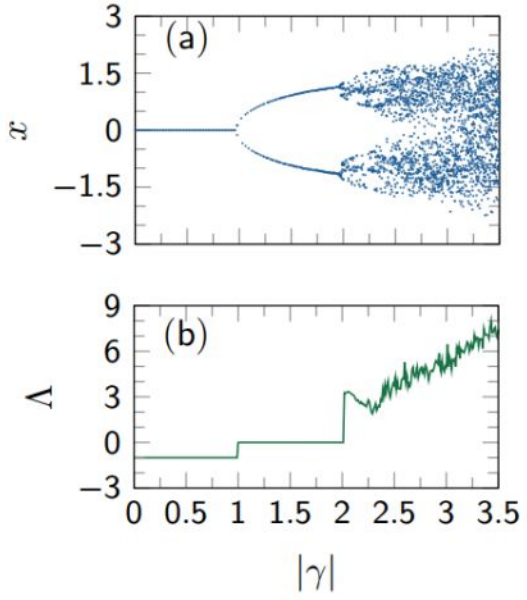

Figure 3.3: (Color online) (a) Bifurcation diagram depicting the Hopf bifurcation routes to chaos. (b) Largest Lyapunov exponent Λ.

Another comparison between standard OEO and CN-OEO which is presented in the bifurcation diagram, is to notice that for the chosen parameters, mixed-mode oscillations also known as breathers are missed in our CN-OEO [10, 57]. The theory of breathers in OEO has been investigated through the geometric singular perturbation theory (see [84] and Refs. therein) and it is well known that the standard wide-band OEO displays breathers while routing to chaos [10]. To gain insight into their control in our system, it is necessary to analyze the case where only the cubic-term is canceled in equation. (3.4). The result presented in Figure 3.4 (a) testifies the presence of breathers which are manifested by damped oscillations around the attractive branches of the invariant critical manifold of the system, while they do not occur when the cubic-term is considered (Figure 3.4 (b)).

Indeed, the invariant critical manifolds are those static S-shaped curves of Figures 3.4 (a) and (b) defined in the (x–y) plane by setting $\varepsilon dx/d\nu = 0$ in equation. (3.9); That is:

$$\rho y^3 + y = x - \beta\{\cos^2[x_\sigma + \phi]\}\,. \tag{3.19}$$

Each invariant critical manifold is characterized by two fold points x_1 and x_2 which are solutions of $dy/dx = 0$, yielding

$$x_1 = -\frac{\pi}{2} + \frac{1}{2}\arcsin\left(\frac{1}{\beta}\right) - \phi\,, \tag{3.20}$$

$$x_2 = -\frac{1}{2}\arcsin\left(\frac{1}{\beta}\right) - \phi\,. \tag{3.21}$$

These critical points are marked with large dots and subdivide each invariant critical manifold into three branches, two of which are attractive (solid lines) and one is repulsive (dotted line) (see Figure 3.4).

The slow-fast oscillations recorded in OEO result from alternate passages of its trajectory from one attractive branch to another and thanks to the acceleration it undergoes when this trajectory enters the zone of the repulsive branch. Indeed, a point of the trajectory taken near the fold point is accelerated by the repulsive branch towards the other attractive branch which is not attached to that fold point. The influence of the repulsive branch on the trajectory can not dwell infinitely. It ceases when the speed cancels out ($dx/d\nu \to 0$ in dynamic mode). In the phase plane, this corresponds to $dx/dy = 0$, with $\sigma \neq 0$ and are marked by points a_1 and a_2 of Figure (a), and b_1 and b_2 of Figure 3.4 (b). We will refer them as the first notches. The positioning of these first notches is crucial for the appearance of breathers: if the first notch (for example a_1) is quite far from the attractive branch, the attraction imposed by the branch on the trajectory is manifested through damped oscillations around the branch, and the trajectory ended up alongside it. The damped oscillations give rise to other notches (see Figure 3.4 (a)). In the time domain, this phenomenology is known as breathers. On the contrary, if the first notch

(for example b_1) occurs very close to the attractive branch, then the trajectory fully or asymptotically meet this attractive branch while evolving towards the fold static point (for example x_1) where the acceleration of the repulsive branch takes the relay and the cycle starts again. Therefore, the system will not display breathers, and in this regard, the dynamics of this system significantly differs from the multiscale oscillations that can be observed in other architectures of OEOs (see for example [17, 19, 57]).

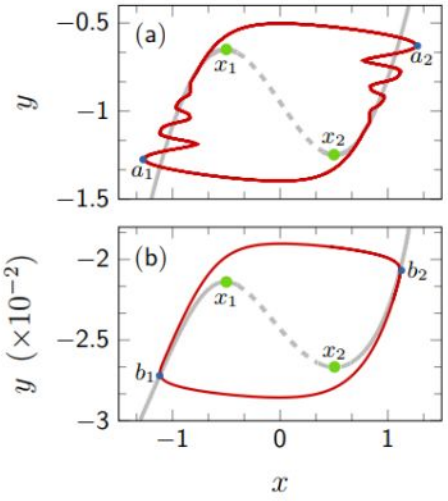

Figure 3.4: (Color online) Projections in the (x–y) plane of the trajectories (solid red (or black)) of: (a) the standard OEO (i.e. without cubic-term in equation. (3.9)) and (b) the cubic-nonlinear OEO. The time trace of Figure 3.4 (b) is given in Figure 3.6 (d). The dashed and solid greys are the instable and stable branches of the invariant critical manifold, respectively. The invariant critical manifolds are plotted for $\sigma \to 0$ [12]. In both figures, $|\gamma| = 1.9$ and $\phi = -\pi/4$.

Time traces permits to highlight the dynamic of the oscillator. First, we will see the comportment near the Hopf bifurcation, doing a comparison between the standard OEO and the CN-OEO. Taking the case of $|\gamma| = 1.01$ and $\phi = -\pi/4$, the frequency increasing factor $\sqrt{1 + 3\rho y_0^2} \sim 4$, Figure 3.5 validates the increase of the frequency of the CN-OEO, as well as its amplitude, comparatively to the standard OEO. That increase of frequency dwells for all values of the gain.

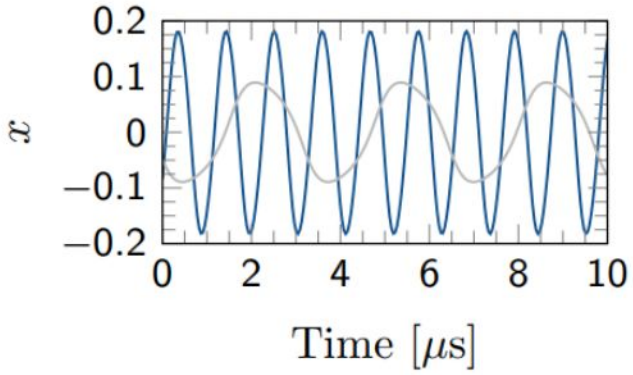

Figure 3.5: (Color online) Timetraces of the amplitude of the cubic-nonlinear OEO (blue or black) versus the standard OEO (grey). $|\gamma| = 1.01$ and $\phi = -\pi/4$. A noticeable effect of the nonlinearity is to increase the frequency of the limit-cycle induced by the primary Hopf bifurcation..

The bifurcation diagram also showed that the amplitude of the signal would increases os the normalized feedback gain increased, and the route to chaos across through a limit-cycle. The time traces at different levels of the bifurcation diagram reveals that close to the Hopf bifurcation, the system displays harmonic oscillations (Figures 3.6 (a) and (b)). But, as $|\gamma|$ increases, harmonic oscillations are replaced by relaxation limit-cycles demonstrating the alternation between the slow and the fast transitions as the time evolves (Figures 3.6 (c) and (d)). For very large values of $|\gamma|$ time traces of Figures 3.6 (e) and (f) illustrate the chaotic behavior of the system.

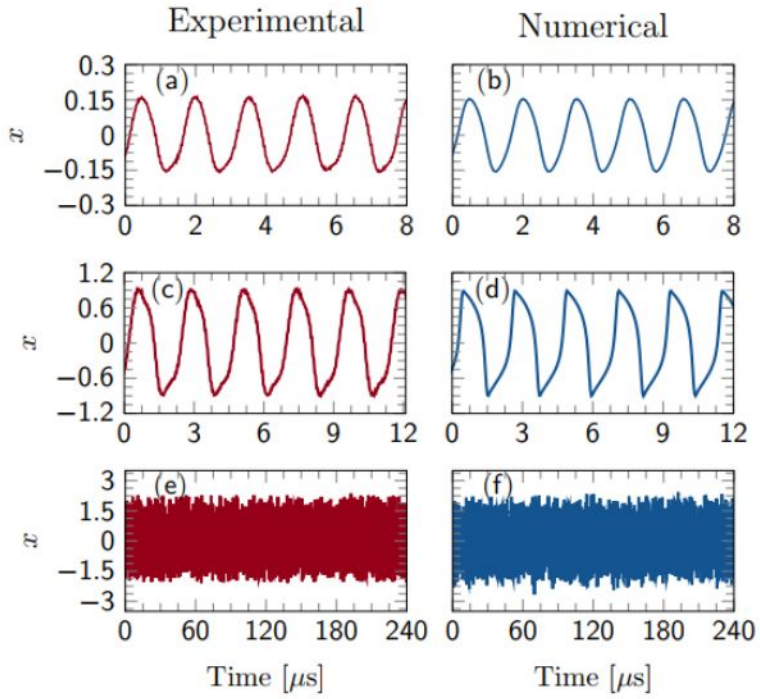

Figure 3.6: (Color online) Experimental and numerical timetraces demonstrating the dynamical evolutions of the system as the gain increases. $\phi = -\pi/4$. From top to bottom: - for experimental curves, P_{in} is progressively 6.51 mW, 7 mW, and 7.8 mW; - for the numerical ones, β is equal to 1.1, 1.9, and 3.

Our CN-OEO can operate either narrow-band or wide-band. It can displays or not a breathers. Indeed, when we take $\eta = 0$ the oscillator run with the same dynamic with the standard one. It means that our CN-OEO is more versatile that the standard one. After theses general observations, it is time to characterize that CN-OEO through some keys parameters of the system.

3.3 Characterization in term of keys parameters of the system of the CN-OEO

This part addresses a deeper dynamical characterization of the CN-OEO in terms of key parameters such as the strength of the feedback gain, the time-delay, the offset phase, and the cubic-nonlinear term. To this end, this part will be subdivided into four parts. The first one is the stability analysis of fixed points in term of keys parameters, the second part addresses to the bifurcation analysis of the CN-OEO, third part presents the normal form analysis which help to study the properties of the system (amplitude, frequency), and the last part deals with the effect of the cubic-nonlinear term on oscillation condition of the system.

3.3.1 Stability analysis of fixed points in term of keys parameters

To perform this analysis, we consider equation. (3.4) and rewrite it considering the following rescaling $\nu = \frac{T_D}{\tau}$, $x(t-\nu) = x_\nu$, $y = \frac{1}{\tau}\int_0^t x(s)\,ds$, $\epsilon = \frac{\tau}{\theta}$, and $\eta = \mu\tau^3$. The equation. (3.4) can be rewritten under the form of the following flow:

$$\dot{x} = -x - \epsilon y - \eta y^3 + \beta\cos^2[x_\nu + \phi] \tag{3.22}$$

$$\dot{y} = x\,, \tag{3.23}$$

where the "overdot" stands for the derivation according the dimensionless time $t = \frac{t'}{\tau}$. In the previous section, it was shown that the fixed point (x_{st}, y_{st}) of the system is such that [**?**]:

$$x_{st} = 0 \tag{3.24}$$

$$y_{st}^3 + \frac{\epsilon}{\eta}y_{st} = \frac{\beta}{\eta}\cos^2\phi \tag{3.25}$$

The stability analysis of the fixed point shows that limit-cycle oscillation of frequency $\omega_{_H}$ might occur through a Hopf bifurcation at $\gamma_{_H}$ (with $\gamma = \beta\sin(2\phi)$ being the effective feedback gain and $\gamma_{_H} = \beta_{_H}\sin(2\phi)$ its value at the Hopf bifurcation point) if and only if $\omega_{_H}$ and $\gamma_{_H}$ fulfill the following transcendental equations:

$$1 + \gamma\cos\omega_{_H}\nu = 0 \tag{3.26}$$

$$-\omega_{_H}^2 + (\epsilon + 3\eta y_{st}^2) + \gamma\omega_{_H}\sin\omega_{_H}\nu = 0\,, \tag{3.27}$$

After some mathematical investigations, equations. (3.26) and (3.27) can be approximated with a third-order precision as:

$$\omega_{_H} = \sqrt{\frac{3}{2}\left[\frac{-1+\sqrt{1+\frac{4}{3}\nu(\epsilon+3\eta y_{st}^2)}}{\nu^2}\right]} \tag{3.28}$$

$$\gamma_{_H} = -1 - \frac{\omega_H^2\nu^2}{2} + \frac{\omega_H^4\nu^4}{24}. \tag{3.29}$$

Theses last equations allows us to say that the frequency of the system decreases with the normalized time-delay ν, and increases with the cubic nonlinear parameter η. This Hopf bifurcation point marks the beginning of oscillations in the system that evolve until the chaotic dynamics as it is developed in the next section.

3.3.2 Bifurcation analysis of the CN-OEO: Route to chaos

In the previous section, the equation (3.29) predict that a Hopf bifurcation for $|\gamma| \simeq 1$.

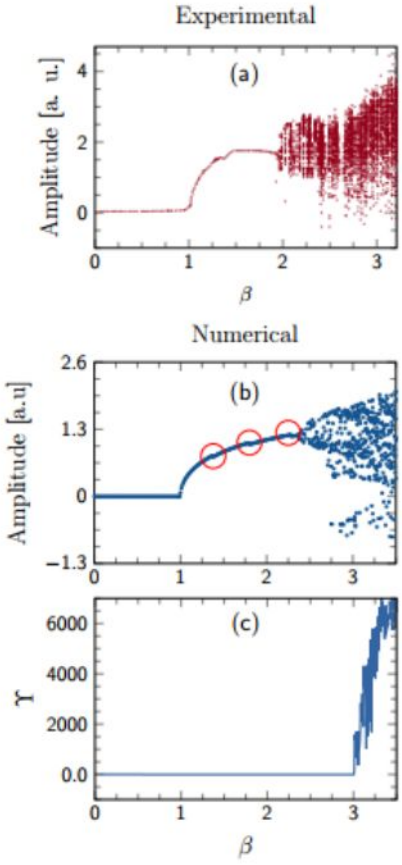

Figure 3.7: (a) A point-by-point recorded of the experimental bifurcation diagram. (b) the numerical bifurcation diagram and (c) the corresponding maximum Lyapunov exponent. One can note the qualitative agreement between the experimental and numerical curves. The value of η calculated using the experimental values of components is $\eta = 9.809 \times 10^{-5}$, $\phi = \frac{-\pi}{4}$

The bifurcation diagrams of Figures 3.7 (a,b) effectively unveils a Hopf bifurcation at $|\gamma| \simeq 1$ as predicted by equation (3.29). Just above 2.5, Chaos arises in the system as confirmed by the plot of the maximum Lyapunov exponent of Figure 3.7 (c). It is also important to note that in the region of limit-cycle oscillations, the amplitude globally grows with the feedback gain. More precisely, it is a stepped bifurcation characterized by amplitude jump phenomenon at some specific values of the feedback gain but not regularly spaced ($|\gamma| \simeq 1.379$, $|\gamma| \simeq 1.797$, and $|\gamma| \simeq 2.28$).

The first region where the amplitude jump phenomenon occurs is highlighted in Figure 3.8 (the case for $|\gamma| \simeq 1.379$). As it can be seen, around that region, the amplitude first undergoes a progressive increase and suddenly decreases before starting to gradually increase again. Before and after the fall of amplitude, the periods of oscillations of the system for two neighboring values of $|\gamma|$ are very close. For instance, for two points taken before the jump, we noticed that $T = 3.288 \times 10^{-7}$s when $|\gamma| = 1.378$ and $T = 3.278 \times 10^{-7}$s when $|\gamma| = 1.379$. After the jump, $T = 3 \times 10^{-7}$s when $|\gamma| = 1.38$ and $T = 2.981 \times 10^{-7}$s

when $|\gamma| = 1.381$. One can immediately observed that the period globally decreases as the effective feedback gain increases. For very close values of the effective feedback gain, and at the neighborhood of the jump, there is an important variation of the period of oscillation compared to closer points at each size. Indeed, when $\gamma = 1.379$, $T = 3.278 \times 10^{-7}$s and when $|\gamma| = 1.38$, $T = 3 \times 10^{-7}$s; the variation of the period in this interval gives $\Delta T = 2.78 \times 10^{-8}$s for just a light change in the effective feedback gain equal to 0.001.

Then, the amplitude drop is accompanied by a large variation of the period of limit-cycle oscillation. Moreover, this phenomenon unveils that two limit-cycle oscillations with the same amplitude can evolve with different periods. An example is the case of two limit-cycles (one obtained at $|\gamma| = 1.365$ and the other at $|\gamma| = 1.397$) which oscillate with the periods ($T = 3.27 \times 10^{-7}$s and $T = 3.278 \times 10^{-7}$s, respectively) but with same amplitude $x \simeq 0.782$. It was noticed that this behavior is globally the same for the other jumps point apart from the fact that the variation of the periods are not the same, however, gradually decreases as the effective feedback gain increases. Indeed, for the second and the third points of jump phenomenon $|\gamma| \simeq 1.797$ and $|\gamma| \simeq 2.28$, the variations are $\Delta T = 2.28 \times 10^{-8}$s and $\Delta T = 1.98 \times 10^{-8}$s, respectively.

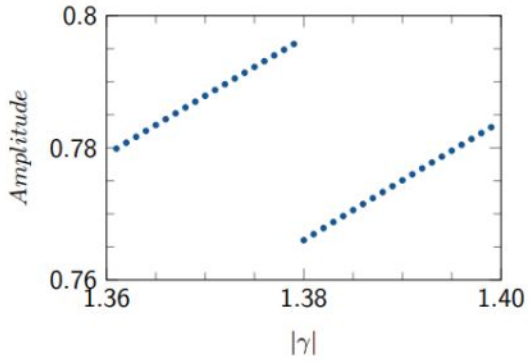

Figure 3.8: (Observation of one step of the bifurcation curve when $\beta = 1.379$.

The phase portrait allows us to understand the dynamics of the CN-OEO. Indeed, the limit-cycle oscillation dominates until $|\gamma|$ close to 2.5 (see Figures 3.9 (a),(d)). A time trace of chaotic dynamics and the corresponding phase portrait are shown in Figures. 3.9 (c),(f). The transition from limit-cycle to chaos occurs exactly at $|\gamma| = 2.5$ and the system displays a crenelated oscillation (see Figures. 3.9 (b),(e)). This crenelated oscillation is similar to the one obtained by Weicker *et al.* with a standard OEO featuring a phase modulator in the nonlinear transfer function and two time-delays in the feedback loop [17]. The crenelated oscillation displays two type of dynamics: the slow dynamics characterized by square oscillations of the plateau and the fast dynamics representing the fast oscillations inside the plateau.

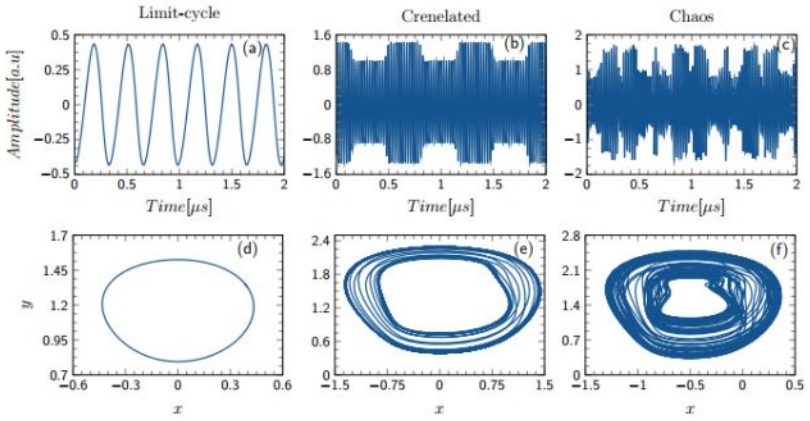

Figure 3.9: (Time traces and phase portraits (for $\phi = \frac{-\pi}{4}$, and $\eta = 9.809360 \times 10^{-5}$) of the system at different levels of the bifurcation diagram.$|\gamma| = 1.1$ (a) and (d), $|\gamma| = 2.5$ (b) and (e), and $|\gamma| = 3.0$ (c) and (f).

From this bifurcation analysis it is noticeable that two main dynamics are dominant in the CN-OEO: the limit-cycle and chaos oscillations. The analytical analysis of Chaos remain a great challenge whereas recently, it was demonstrated that limit-cycle in inherent-infinite dimensional systems such the standard OEO can be analytically characterized in terms of their amplitude and frequency using the method of the normal form [12]. In the next section, that method of the normal form will be applied on our CN-OEO.

3.3.3 Characterization of limit-cycle oscillation by using the Normal form

The literature proposes several approaches to analyze the nature of Hopf bifurcation of retarded systems including integral averaging, the Freehold alternative, the implicit function theorem, the method of multiple scales and the center-manifold reduction [95]. In this thesis, we choose the method of center manifold reduction since it has been successfully used to characterize standard OEO [12] and other time delayed systems [95–98]. It stipulates that the long-time dynamics of a system can be reduced to the dynamics on its center manifold. Also, it is a rigorous mathematical technique that makes this reduction possible, at least near the Hopf bifurcation point (see [99]).

Before the Hopf bifurcation point, the dynamics of the system is ruled by the trivial steady state of the variable $x_{st} = 0$ (see Figure 3.7). Moreover, around that Hopf bifurcation point the relative gain $\delta = \gamma - \gamma_{_H} = (\beta - \beta_{_H}) \sin 2\phi$ is considered as a small parameter ($\delta \ll 1$). Therefore, in the neighborhood of the Hopf bifurcation point, a Taylor expansion around x_{st} and δ can be carried out so that equations. (3.22) and (3.23) transform into a linear ($\mathcal{L}X + \mathcal{R}X_\nu$) and nonlinear ($\mathcal{F}(X_\nu)$) part as follows:

$$\dot{x} = -x - \epsilon y - \eta y^3 - \beta[x_\nu \sin 2\phi + x_\nu^2 \cos 2\phi - \frac{2}{3} x_\nu^3 \sin 2\phi] \quad (3.30)$$

$$\dot{y} = x \quad (3.31)$$

Let us introduce the vector matrix $X = \binom{x}{y}$. For mathematical convenience and without loss of generality, equations. (3.30) and (**??**) can be separated into a linear ($\mathcal{L}X + \mathcal{R}X_\nu$) and nonlinear ($\mathcal{F}(X_\nu)$) part as follows [12]:

$$\dot{X} = \mathcal{L}X + \mathcal{R}X_\nu + \mathcal{F}(X_\nu)\,, \quad (3.32)$$

with $X = \binom{x}{y}$ being the vector matrix of the variable of the system, and

$$\mathcal{L} = \begin{bmatrix} -1 & -\epsilon \\ 1 & 0 \end{bmatrix} \quad (3.33)$$

and

$$\mathcal{R} = \begin{bmatrix} -\gamma_{_H} & 0 \\ 0 & 0 \end{bmatrix} \quad (3.34)$$

are the 2×2 matrices. $\mathcal{F}$ is a column vector defined as:

$$\mathcal{F}(X_\nu) = \begin{pmatrix} -\delta x_\nu - \eta y^3 - \alpha\gamma_{_H} x_\nu^2 + \frac{2}{3}\gamma_{_H} x_\nu^3 \\ 0 \end{pmatrix} \quad (3.35)$$

In equation (3.35), $\alpha = [\tan(2\phi)]^{-1}$. Since equation. (3.32) is a delay-differential equation, computing this equation requires to consider the time intervals in the past ($[-\nu, 0]$) and after the time origin ($[0, +\infty[$). Let us refer as θ the time within the interval $[-\nu, 0]$ and maintain the notation of time t within $[0, +\infty[$. Then, equation (3.32) can be written as a step equation:

$$\frac{dX_{t(\varsigma)}}{dt} = \mathcal{A}X_{t(\varsigma)} + \mathcal{G}(X_{t(\varsigma)}), \quad (3.36)$$

where $X_{t(\varsigma)} = X(t + \varsigma)$ is a portion of the solution trajectory in the recent past. $\mathcal{A}$ is the linear operator with pure imaginary eigenvalue $i\omega_{_H}$ of the Hopf bifurcation point. $\mathcal{A}$ transforms a center subspace function $p(\theta)$ as follows:

$$\begin{aligned} \mathcal{A}p(\varsigma) &= i\omega_{_H} p(\varsigma) \\ &= \begin{cases} \frac{dp(\varsigma)}{d\varsigma} & \text{for} \quad -\nu \le \varsigma \le 0 \\ \mathcal{L}p(0) + \mathcal{R}p(-\nu) & \text{for} \quad \varsigma = 0. \end{cases} \end{aligned} \quad (3.37)$$

It is known that when $i\omega_{_H}$ is an eigenvalue of the Hopf bifurcation, its complex conjugate

$-i\omega_{_H}$ is also an eigenvalue. Thus, to take into account both eigenvalues, we define the adjoint operator of $\mathcal{A}$, call $\mathcal{A}^*$ which also acts on another subspace function $q(\varsigma)$ as:

$$\begin{aligned} \mathcal{A}^* q(\varsigma) &= -i\omega_{_H} q(\varsigma) \\ &= \begin{cases} -\frac{dq(\varsigma)}{d\varsigma} & \text{for} \quad 0 \leq \varsigma \leq \nu \\ \mathcal{L}^* q(0) + \mathcal{R}^* q(\nu) & \text{for} \quad \varsigma = 0, \end{cases} \end{aligned} \tag{3.38}$$

where $\mathcal{L}^*$ and $\mathcal{R}^*$ are the adjoint of the operators $\mathcal{L}$ and $\mathcal{R}$, respectively. In equation (3.36), the expression of the vector $\mathcal{G}$ is:

$$\mathcal{G} = \begin{cases} 0 & \text{for} \quad -\nu \leq \varsigma \leq 0 \\ \mathcal{F} & \text{for} \quad \varsigma = 0. \end{cases} \tag{3.39}$$

In the theory of the center manifold reduction it requires that the subspace functions $p(\varsigma)$ and $q(\varsigma)$ satisfy the inner product:

$$< q, p >= \bar{q}(0)p(0) + \int_{-\nu}^{0} \bar{q}(\xi + \nu) R_H^* p(\xi) d\xi \,, \tag{3.40}$$

The "overline" stands for the complex conjugation. Since $X_t(\varsigma)$ must be finite, it is necessary to introduce a normalization condition such that $< q, p >= 1$ and $< q, \bar{p} >= 0$. These inner products lead to the following solutions of equations (3.37) and (3.38), respectively:

$$p(\varsigma) = \binom{i\omega_{_H}\varsigma}{1} e^{i\omega_{_H}\tau}; q(\varsigma) = b \begin{pmatrix} 1 \\ -i\epsilon/\omega_{_H} \end{pmatrix} e^{i\omega_{_H}\varsigma} \tag{3.41}$$

where b is a complex-valued parameter defined as follows:

$$b = [1 - 2i\omega_{_H} + \gamma_{_H}(1 + i\omega_{_H}\nu)e^{i\omega_{_H}\varsigma}]^{-1} \,. \tag{3.42}$$

The next step consists to use the center subspace to decompose the trajectory $X_t(\varsigma)$ into two components: the first one $\mathfrak{y}(t)p(\varsigma) + \bar{\mathfrak{y}}(t)\bar{p}(\varsigma)$ lying in the center subspace; the second one $u_t(\varsigma)$ transverse to the center subspace is the infinite-dimensional component and satisfies $< p, u >= 0$ and $< \bar{p}, u >= 0$. Hence,

$$X_t(\varsigma) = \mathfrak{y}(t)p(\varsigma) + \bar{\mathfrak{y}}(t)\bar{p}(\varsigma) + u_t(\varsigma) \tag{3.43}$$

Substituting this last equation into equation 3.36 and using the inner products yield that

$\mathfrak{y}(t)$ satisfies the following first-order differential equation:

$$\begin{aligned}\dot{\mathfrak{y}}(t) = i\omega_{_H}\mathfrak{y} - \delta\bar{b}\lambda\mathfrak{y} - 3\eta b\mathfrak{y}^2\bar{\mathfrak{y}} - \bar{b}\gamma_{_H}\alpha(\lambda\mathfrak{y} + \bar{\lambda}\bar{\mathfrak{y}})^2 \\ -2i\bar{b}(\gamma_{_H}\alpha\lambda)^2\bar{\lambda}[\tfrac{\bar{b}}{\omega_{_H}}\lambda - 7\tfrac{b}{3\omega_{_H}}\bar{\lambda} + 2\omega_{_H}\Gamma e^{-2i\omega_{_H}\nu}]\mathfrak{y}^2\bar{\mathfrak{y}} \\ +2\bar{b}\gamma_{_H}\lambda^2\bar{\lambda}\mathfrak{y}^2\bar{\mathfrak{y}} + NRT\end{aligned} \tag{3.44}$$

NRT represents the non-resonant terms of the equation and the "overdot" represents the differentiation with respect to time. The complex coefficients λ and Γ are explicitly given by:

$$\lambda = i\omega_{_H}e^{-i\omega_{_H}\nu} \quad , \tag{3.45}$$

$$\Gamma = [4\omega_{_H}^2 - \epsilon - 2i\omega_{_H}(1 + \gamma_{_H}e^{-2i\omega_{_H}\nu})]^{-1} \tag{3.46}$$

Now introducing the near-identity transformation

$$\mathfrak{y}(t) = z + k_{11}z^2 + k_{12}z\bar{z} + k_{13}\bar{z}^2 \tag{3.47}$$

into equation 3.44 and eliminating the secular terms yields:

$$k_{11} = \tfrac{i\bar{b}\gamma_{_H}\alpha}{\omega}\lambda^2, \tag{3.48}$$

$$k_{12} = \tfrac{-2i\bar{b}\gamma_{_H}\alpha}{\omega}\lambda\bar{\lambda}, \tag{3.49}$$

$$k_{13} = \tfrac{-i\bar{b}\gamma_{_H}\alpha}{3\omega}\bar{\lambda}^2 \tag{3.50}$$

The non-secular terms that remain constitute the complex normal form of the system given by:

$$\dot{z} = i\omega z - \delta\bar{b}\lambda z - 3\eta\bar{b}z^2\bar{z} + \bar{b}\gamma_{_H}\lambda^2\bar{\lambda}[2 - 4i\omega\gamma_{_H}\alpha^2\Gamma e^{-2i\omega\nu}]z^2\bar{z} \tag{3.51}$$

where the coefficient

$$\alpha = [\tan(2\phi)]^{-1} \ , \tag{3.52}$$

and $\delta = \gamma - \gamma_{_H}$ is the relative effective feedback gain. The "overline" stands for the complex conjugation. In the first approximation, the variable z is related to the complex amplitude of limit-cycle oscillation by $z(t) = A(t)e^{i\omega_{_H}t}$ which, replaced in Eq. 3.51 leads to the complex normal form of the amplitude:

$$\dot{A} = -\delta\Lambda_1 A + \Lambda_2 A^2\bar{A}\,, \tag{3.53}$$

where the coefficients Λ_1 and Λ_2 have the following expressions:

$$\Lambda_1 = \tfrac{i\omega_{_H}e^{-i\omega_{_H}\nu}}{[1+2i\omega_{_H}+\gamma_{_H}(1-i\omega_{_H}\nu)e^{-i\omega_{_H}\nu}} \quad , \tag{3.54}$$

$$\Lambda_2 = 2\gamma_{_H}\omega_{_H}^2\Lambda_1[1 - 2i\omega_{_H}\gamma_{_H}\alpha^2\Gamma e^{-2i\omega_{_H}\nu}] - 3\eta\Lambda_1/\lambda \tag{3.55}$$

Equation (3.53) is a complex equation whose solution can be approximated in the form of $A = a(t)e^{i\varphi(t)}$ that will allow us to study the evolution of the amplitude and the frequency around the Hopf bifurcation. Replacing A in Eq. (3.53) yields:

$$\dot{a} = -\delta\Lambda_{1r}a + \Lambda_{2r}a^3 \tag{3.56}$$

$$\dot{\varphi} = -\delta\Lambda_{1i} + \Lambda_{2i}a^2, \tag{3.57}$$

with Λ_{1r} and Λ_{1i} being the real and the imaginary parts of Λ_1, respectively. Similarly, Λ_{2r} and Λ_{2i} are also the real and the imaginary parts of Λ_2, respectively.

The equilibrium points of equation (3.56) are:

$$a_{st_0} = 0\,, \tag{3.58}$$

$$a_{st_1} = \sqrt{\tfrac{\delta\Lambda_{1r}}{\Lambda_{2r}}}\,, \tag{3.59}$$

$$a_{st_2} = -\sqrt{\tfrac{\delta\Lambda_{1r}}{\Lambda_{2r}}}\,, \tag{3.60}$$

which are defined if and only if $\Lambda_{2r} \neq 0$ and $\frac{\delta\Lambda_{1r}}{\Lambda_{2r}} > 0$. The stability condition of the trivial(a_{st_0}) and the non trivial ($a_{st_{1,2}}$) states depends on the sign of the multiplicities

$$\lambda_{st_0} = -\delta\Lambda_{1r} \tag{3.61}$$

and

$$\lambda_{st_{1,2}} = 2\delta\Lambda_{1r} \tag{3.62}$$

, respectively. Equation (3.57) reveals that the dynamics of the phase is directly related to the one of the amplitude. The phase is defined for amplitudes different from zero. Indeed, for $a = a_{st0} = 0$, $A(t) = 0$ and $z(t) = 0$; There are no oscillations in the system. For $a = a_{st_{1,2}}$, the solution of equation (3.57) yields:

$$\varphi = \delta kt + \varphi_0\,, \tag{3.63}$$

where φ_0 being the reference phase which is arbitrarily set to zero if needed and $k = \frac{\Lambda_{1r}\Lambda_{2i} - \Lambda_{1i}\Lambda_{2r}}{\Lambda_{2r}}$ being a coefficient. The stability of the phase is satisfied if $k = 0$ which corresponds to $\Lambda_{1r}\Lambda_{2i} = \Lambda_{1i}\Lambda_{2r}$.

Beyond the Hopf bifurcation point, the system undergoes the limit-cycle oscillations. From what precedes, it can be demonstrated that the amplitude and the frequency of such limit-cycle oscillations can be explicitly defined as a function of the relative effective feedback gain $\delta \equiv \gamma - \gamma_{_H}$ following:

$$a = 2\omega_{_H}\sqrt{(\gamma - \gamma_{_H})\tfrac{\Lambda_{1r}}{\Lambda_{2r}}} \tag{3.64}$$

$$\omega_{eff} = \omega_{_H} + (\gamma - \gamma_{_H})\tfrac{\Lambda_{1r}\Lambda_{2i} - \Lambda_{1i}\Lambda_{2r}}{\Lambda_{2r}} \tag{3.65}$$

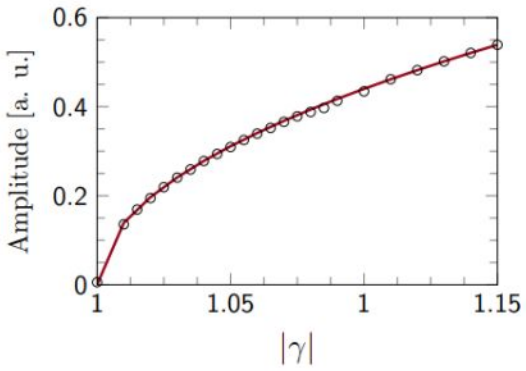

Figure 3.10: Variation of the amplitude versus the effective feedback gain $|\gamma|$. The analytical curve (solid line) is obtained from equation (3.64), while the numerical curve (black circles) is plotted using equations (3.22) and (3.23). $\phi = -\frac{\pi}{4}$, $y_{st} = 14.6$, $\eta = 9.809360 \times 10^{-5}$, and $\phi = \frac{-\pi}{4}$.

The Figure 3.10 shows the variation of the amplitude when the gain is increased beyond the Hopf bifurcation point. Besides, Figure 3.11 shows the variations of the effective frequency of oscillation as a function of the normalized time-delay. Qualitatively, the variation in both figures are similar to those observed with the standard OEO [12]. The amplitude scales as $\sqrt{|\delta|}$ beyond the Hopf bifurcation with the proportionality factor equal to $2\omega_H\sqrt{\frac{\Lambda_{1r}}{\Lambda_{2r}}}$ and is a function of all the time constants of the oscillator including the cubic-nonlinear coefficient. However, the frequency asymptotically decreases with the time-delay. Furthermore, Figure 3.11 depicts that for the same value of a time-delay, the CN-OEO evolves with limit-cycle oscillations whose frequencies are higher compared to those of the standard OEO. These results are in accordance with the prediction. It is noteworthy that when investigating on the optoelectronic oscillators, the offset phase (see equation (3.63)) remains a parameter that should be taken with more consideration. Indeed, the oscillations can be cancelled if the offset phase is not appropriately chosen [100–103]. The next section addresses the impact of the cubic-nonlinear term on the oscillation condition induced by the offset phase.

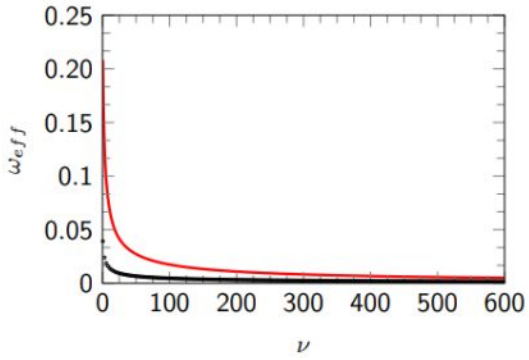

Figure 3.11: Evolution of the effective frequency as a function of the normalized time-delay ν. For the solid line (upper curve), $\eta \neq 0$ and for the dots line (bottom curve), $\eta = 0$. $y_{st} = 14.6$, $\phi = -\frac{\pi}{4}$ and $\delta = -0.02$.

3.3.4 Effect of the cubic-nonlinear term on oscillation condition of the system.

It is know that the standard OEO does not oscillate for all values of the offset phase (see equation 3.63). The values of the offset phase for which the standard OEO runs are very narrow and periodically spaced [100–103]. As well as the limit-cycle is concerned, oscillation means that the steady state $a_{st_{1,2}}$ exist and are stable whereas as a_{st_0} is unstable. Inversely, if the OEO switches off, it means that a_{st_0} is stable while $a_{st_{1,2}}$ is unstable. In other words, the stability condition of a_{st_0} and $a_{st_{1,2}}$ are opposite (see equations (3.61) and (3.62)) and then describe the supercritical and subcritical pitchfork bifurcation. Indeed, the fact that $a_{st_{1,2}}$ are stable while a_{st_0} does not is similar to a supercritical bifurcation whereas stable branch of a_{st_0} when $a_{st_{1,2}}$ are unstable is refers to a subcritical bifurcation of the amplitudes. Then, the oscillating condition can be determine through the existence and stability conditions of $a_{st_{1,2}}$. Such conditions depend on the sign of Λ_{2r} and Λ_{1r} [103]. Remarking that the offset phase only appears in the expression of Λ_2 through the coefficient α (see equations (3.52) and (3.55)) and not in the one of Λ_1 (see equation(3.54)), therefore, the oscillation condition can be determined with the sign of Λ_{2r}. Negative value of Λ_{2r} refers to oscillation of the system whereas positive branch of Λ_{2r} witnesses no oscillation of the system. We plot in Figure 3.12 the value of Λ_{2r} as a function of ϕ. The figure reveals that the standard OEO only oscillates for narrow ranges of ϕ periodically spaced with a period of $|\phi| = \pi/2$. For ϕ within -6 to 0, the system is expected to run when ϕ is around -0.79, -2.35, -3.93, and -5.5 (Figure 3.12(a)). On the contrary, in the CN-OEO, Λ_{2r} is negative for the entire values of ϕ. Consequently, it oscillates regardless the value of the offset phase (Figure 3.12(b)). Nevertheless, we have noticed a threshold value of the cubic nonlinear term that permits to the CN-OEO to display oscillation whatever the value of ϕ. That is $\eta = 2.80936 \times 10^{-5}$. Below that value,

the system behaves as a standard OEO presenting the regions of ϕ for which the OEO functions alternated by the non-oscillating regions (Figure 3.13).

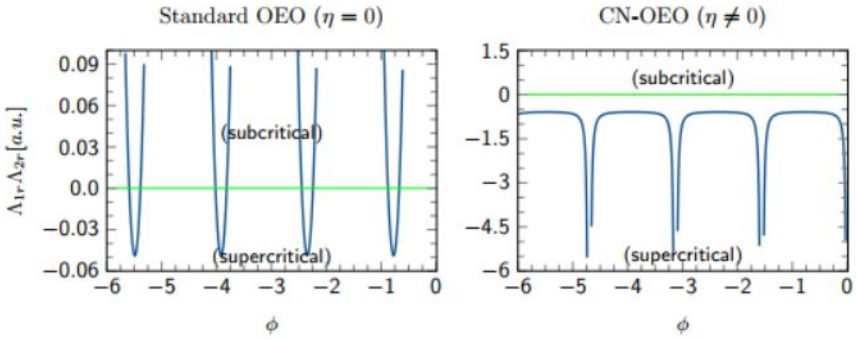

Figure 3.12: Analytical bifurcation map showing the transition between supercritical and subcritical Hopf bifurcation when $\eta = 0$ (the left curve). The horizontal line marks the frontier. For this results, we have focused on the negative slope. On the right we have, for standard-OEO, the analytical bifurcation map which shows the supercritical Hopf bifurcation when $\eta \neq 0$

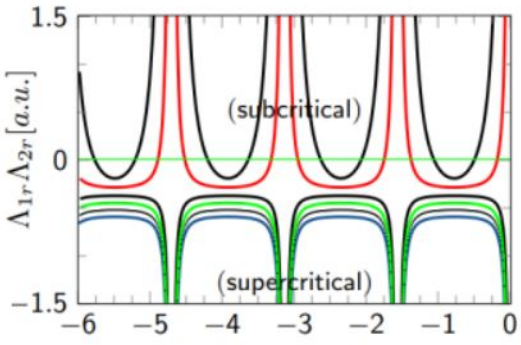

Figure 3.13: Below the border, from bottom to top, these are supercritical curves for η ($\eta = 7.80936 \times 10^{-5}$,$\eta = 5.80936 \times 10^{-5}$,$\eta = 3.80936 \times 10^{-5}$,$\eta = 2.80936 \times 10^{-5}$). The mixed curves are those obtained for $\eta = 1.80936 \times 10^{-5}$,and $\eta = 0.580936 \times 10^{-5}$

We have analyzed the characteristics of the limit-cycle oscillations in terms of some parameters of the system such as the time delay, the feedback strength, and the cubic-nonlinear terms. The frequency increases with the cubic-nonlinear term and decreases with the normalized time-delay. As the bifurcation is concerned, the dynamics of the CN-OEO is essentially dominated by the limit-cycle oscillation and chaos. The transition between them is through crenelated oscillation. Moreover, the limit-cycle oscillations undergo small amplitude jumps that are observed at specific points during its progression. These amplitude jumps are manifested by a sudden decrease of the period of oscillation. The characterization of the limit-cycle oscillation by the use of the normal form reduction

has permitted to derive the analytical expressions of both their amplitude and frequency. It is demonstrated that their evolve similarly to a standard OEO. But, this latter has lower frequency of oscillation. The method of the normal form reduction has also helped to analyse the impact that the cubic nonlinear term has the oscillation condition of the CN-OEO. The results have shown the this when this term is appropriately chosen, the OEO can run independently of the offset phase. Such result can be benefit in manufacturing optimal OEO with energy efficiency. Our future works will deal with the application of this work to other simple architectures of OEO and the synchronization of several CN-OEOs.

Our CN-OEO is rubust to the offset phase of the intensity MZM.

3.4 The simplified benchmark of the CN-OEO

In this part, we present a study of a simplified optoelectronic oscillator (OEO) that features both the laser and the filter nonlinearities. We consider the case where we have a low pumps of laser diode.It is important to mention that the nonlinear transfer function in the limit of low pumps of laser diode it is not the same with the nonlinear transfer function in the limit of high pumps of laser diode. To perform that simplified OEO, we will subdivide this section in three subsections.The first subsection will be devoted to the system and model of the system, the second subsection will presents the stability analysis, the third section will presents the nonlinear dynamics.

3.4.1 System and model of the simplified CN-OEO

The CN-OEO presented in the previous sections, apart runs in narrow-band and wide-band, generate ultra-pure high frequency signals, be more versatile that the standard OEO, has several application like chaos-based communication, measurement, sensing, detections, neuromorphic computing... Achieving these applications is not the only objective. Another one is to meet the strict requirements of future communications, radars, navigation, satellite systems, and embedded systems. In that scope, in this system (simplified CN-OEO), the electro-optical modulation is carried out by the laser diode and no longer with the Mach Zehnder modulator. Indeed, instead of using the intensity or phase modulator, other electro-optic devices such as electroabsorption modulated laser were used to simultaneously perform three functions namely lasing, photodetection, and intensity modulation [61] or direct optical feedback onto the laser-diode was also proposed to perform intensity modulation [64, 65].

The goal of the simplified CN-OEO is to reduce the number of components in the OEO oscillator. Here, the seeding laser diode itself is used to perform the electro-optical conversion through its light-intensity piecewise function instead of an intensity or phase-

modulator and termed simplest OEO [66]. The drawback of this method is the reduction of the bandwidth which is scaled from kHz to tens of GHz (with external modulator) to kHz to few GHz (with seeding laser-diode) imposed by the relaxation oscillation frequency of the laser diode. Nevertheless, this method brings a general benefit in the physical equipment, power consumption, and it reduces the cost and congestion [57, 66, 79]. Later on, to emulate the complex dynamics in this simplified architecture of OEO, other authors proposed cascading the electrical path of the simplest OEO with additional nonlinear electronic oscillators such as the Van der Pol [57] and the Colpitts [58] oscillators. Novel dynamics not encountered in standard and simplest OEOs were recovered namely, bursting, anti-monotonicity, and pulse packages.

The experimental device of our simplified CN-OEO presented in Figure 3.14 is made of a telecommunication continuous-wave distributed feedback laser diode source with wavelength $\lambda_L \simeq 1.55\ \mu m$, threshold current $I_{th} = 15.2\ mA$ which is pumped with a current under the form of $I_{pol} + I_{RF}(t)$, where I_{pol} is the polarization current, $I_{RF}(t)$ is the time-varying radio-frequency (RF) current. Then, the laser outputs the power $P(t)$ that is retarded through an optical delay line yielding a time-delay T_D. An InGaAs fast photodiode (PD) converts the delayed light into an electrical signal V_{in} with a conversion factor $S = 4.75\ V/mW$. This electrical signal V_{in} undergoes a nonlinear transformation by propagating through the cubic-nonlinear band-pass filter (CNBPF). A voltage subtractor (VS) probes the voltage across the resistor of the CNBPF V_R which is then converted into the RF current ($I_{RF} = \frac{V_R}{R_Z}$, where $R_Z = 50\ \Omega$ is the characteristic impedance used for the voltage-to-intensity conversion). This current is combined with the polarization current I_{pol} (bias current) to feed the laser which therefore performs the electrical-to-optical conversion.

The CNBPF is implemented using two capacitors $C_{1,2}$, two resistors (r, R), an operational amplifier U (type $LF356$), a mixed assembly of eight simple junction diodes (type $IN400X$), and one coil L. The thermal voltage of these junction diodes is $V_T = 25\ mV$, the number of junction diodes in series is $n = 4$, and the inverse saturation current is $I_s = 5\ \mu A$.

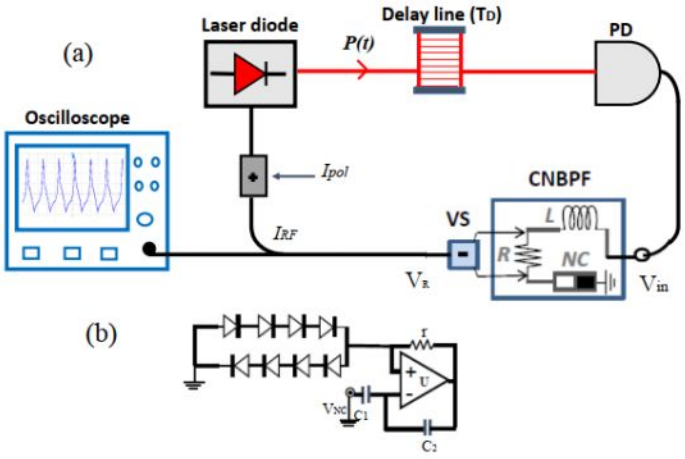

Figure 3.14: (Color online)(a) Experimental setup of OEO featuring both the laser and the filter nonlinearities and (b) Nonlinear Capacitor (NC). The laser used is a DFB telecom laser diode ($\sim$ 1.55 μm) with a threshold injection current $I_{\text{th}} = 15.2$ mA. The 656 m optical fiber induces a time-delay of $T_D = 3.28$ μs. PD is Photodiode, I_{pol} is polarization current; I_{RF} is the current from feedback loop. CNBPF refers to Cubic-Nonlinear Band-pass Filter, VS is the voltage subtractor.

Here again, we Apply the Kirchhoff's laws to Figure 3.14 (b), to have the relationship between the input (V_{in}) and the output (V_R) of the CNBPF. It yields:

$$V_R + \frac{L}{R}\frac{dV_R}{dt} + \left[\frac{1}{c_1} - \frac{nV_T}{2rI_s c_2}\right]\frac{1}{R}\int_0^t V_R\, ds + \frac{nV_T G^2}{6}\left[\frac{1}{2rI_s c_2 R}\right]^3 \left(\int_0^t V_R\, ds\right)^3 = GV_{\text{in}}, \tag{3.66}$$

where t is the time and G is the gain of the voltage subtractor. The laser diode which performs the conversion of the electrical-to-optical signal, in the limit of the low pumps of the laser diode, has the following nonlinear transfer function [57, 66, 79, 80]:

$$P(t) = \begin{cases} 0 & for\ I_{RF}(t) \leq I_0 \\ \mu[I_{RF}(t) - I_0] & for\ I_{RF}(t) > I_0, \end{cases} \tag{3.67}$$

The parameter $\mu = \eta_d h\nu$ is the laser conversion slope with η_d as the quantum efficiency, h the Planck constant, and ν the laser carrier frequency. The experimental value of the parameter μ is $\mu = 0.21W/A$. In Eq.(3.67), $I_0 = I_{th} - I_{pol}$. Taking into account the time-delay experienced by the optical signal during its flow inside the delay line, the voltage provided by the photodiode is related to such retarded optical signal as follows:

$$V_{\text{in}} = KSP(t - T_D), \tag{3.68}$$

where K is a dimensional factor standing for the overall losses (electrical and optical) in

the feedback loop. Inserting equation(3.68) into equation(3.66), our simplified CN-OEO is described by the piecewise cubic-nonlinear integro-differential delayed equation (see equation(3.67) for $P(t-T_D)$):

$$\begin{aligned} V_R + \frac{L}{R}\frac{dV_R}{dt} + \left[\frac{1}{c_1} - \frac{nV_T}{2rI_sc_2}\right]\frac{1}{R}\int_0^t V_R\,ds \\ +\frac{nV_TG^2}{6}\left[\frac{1}{2rI_sc_2R}\right]^3\left(\int_0^t V_R\,ds\right)^3 &= GKSP(t-T_D). \end{aligned} \tag{3.69}$$

Then, considering $I_{RF}(t-T_D) = \frac{V_R(t-T_D)}{R_Z}$ and setting the dimensionless voltage $x = \frac{V_R(t)}{V_0}$, with V_0 a reference voltage ($V_0 = 1\ V$), Eq. (3.69) yields:

$$\begin{aligned} x + \frac{L}{R}\frac{dx}{dt} + \left[\frac{1}{c_1} - \frac{nV_T}{2rI_sc_2}\right]\frac{1}{R}\int_0^t x\,ds \\ +\frac{nV_TG^2V_0^2}{6}\left[\frac{1}{2rI_sc_2R}\right]^3\left(\int_0^t x\,ds\right)^3 &= \frac{KSG}{R_Z}P\left[x(t-T_D) - \frac{R_ZI_0}{V_0}\right]. \end{aligned} \tag{3.70}$$

According to equation (3.70), the system is characterized by four timescales which are the time-delay T_D, the high cut-off time τ, the low cut-off time θ, and the nonlinear timescale ρ that are explicitly given as:

$$T_D = \tfrac{n_0L}{c}, \tag{3.71}$$

$$\tau = \tfrac{L}{R}, \tag{3.72}$$

$$\theta = R[\tfrac{1}{c_1} - (nV_T/2rI_sc_2)]^{-1}, \tag{3.73}$$

$$\rho = \tfrac{nV_TG^2V_0^2}{6}\left[\tfrac{1}{2rI_sc_2R}\right]^3. \tag{3.74}$$

In equation (3.71), L and $n_0 = 1.5$ are respectively the length and the refraction index of the optical delay line, and c is the velocity of light in the vacuum. Therefore, equation (3.70) can be rewritten as:

$$x + \tau\frac{dx}{dt} + \frac{1}{\theta}\int_0^t x\,ds + \rho\left(\int_0^t x\,ds\right)^3 = \frac{KSG}{R_Z}P\left[x(t-T_D) - \frac{R_ZI_0}{V_0}\right]. \tag{3.75}$$

To facilitate the dynamical analysis, it is preferable to recast equation (3.75) under the form of a coupled delay differential equations. For this purpose, we introduce the new variable $y = \frac{1}{\tau}\int_0^t x\,ds$ and the dimensionless times $t' = \frac{t}{\tau}$, $\nu = \frac{T_D}{\tau}$ (the normalized time-delay). Equation (3.75) is therefore transformed into a piecewise slow-fast dynamical system with x as the fast variable while y is the slow variable:

$$\dot{y} = x \tag{3.76}$$

$$\dot{x} + x + \varepsilon y + \eta y^3 = \beta P(x_\nu - \alpha) = \begin{cases} 0\ if\ x_\nu - \alpha \leq 0 \\ \beta(x_\nu - \alpha)\ if\ x_\nu - \alpha > 0. \end{cases} \tag{3.77}$$

Here $x_\nu = x(t' - \nu)$ is the time-delayed variable, and the feedback gain $\beta = \frac{KSG\mu}{R_Z}$. The small quantity $\varepsilon = \frac{\tau}{\theta}$ is the cut-off times ratio, the parameter $\eta = \rho\tau^3$ stands for the cubic-nonlinear parameter, $\alpha = \frac{R_Z I_0}{V_0}$ is the bias parameter. Except the tunable parameter G, other parameters are compatible with the experimental values taken as $L = 0.1\,mH$, $r = 300\,\Omega$, $R = 1.62\,k\Omega$, $C_1 = 270\,pF$, $C_2 = 9.15\,nF$, and $T_D = 3.29\,\mu s$.

To perform the stability analysis, the first step is to determine the fixed points and the second step is to evaluate the stability of theses fixed points through the method of perturbation.

3.4.2 Stability analysis of the simplified CN-OEO

To determine the fixed-point (x_{st}, y_{st}), we stand equations (3.76) and (3.77) obeys to the following:

$$x_{st} = 0 \tag{3.78}$$

$$y_{st}^3 + \frac{\varepsilon}{\eta} y_{st} = \begin{cases} 0 & if \;\; \vartheta \geq 0 \\ \frac{-\alpha\vartheta}{\eta} & if \;\; \vartheta < 0. \end{cases} . \tag{3.79}$$

It appears from equation (3.79) that the solution critically depends on the sign of the bias parameter ϑ.

3.4.2.1 Case of $\vartheta \geq 0$

In this case, equation (3.79) becomes:

$$y_{st}^3 + \frac{\varepsilon}{\eta} y_{st} = 0. \tag{3.80}$$

There is a unique trivial fixed point $(x_{st}, y_{st}) = (0, 0)$ because $\frac{\varepsilon}{\eta}$ is a positive quantity. The stability of this trivial fixed point is determined by the value of the eigenvalue λ (after applying the method of pertubation) which satisfies the following second-order polynomial:

$$\lambda^2 + \lambda + \varepsilon = 0, \tag{3.81}$$

and is calculated as:

$$\lambda_\pm = \frac{-1 \pm \sqrt{1 - 4\varepsilon}}{2}. \tag{3.82}$$

The trivial fixed point (0, 0) is unconditionally stable since the cut-off time is known to be very small ($\varepsilon \ll 1$) in broadband OEO (in the present work, $\varepsilon = 9.7 \times 10^{-4}$). Therefore, no oscillation is expected regardless of the value of the feedback gain β.

3.4.2.2 Case of $\vartheta < 0$

According to equation (3.79), the fixed point y_{st} is the root of the following third-order polynomial:

$$y_{st}^3 + \frac{\varepsilon}{\eta} y_{st} = \frac{-\vartheta\beta}{\eta}, \tag{3.83}$$

which solutions are non-trivial if $\beta \neq 0$ and is unique since $\frac{\varepsilon}{\eta}$ is a positive quantity. Figure 3.15 shows that y_{st} grows which the feedback gain β. It can be noticed that the values of the fixed point parabolically grows with the feedback gain.

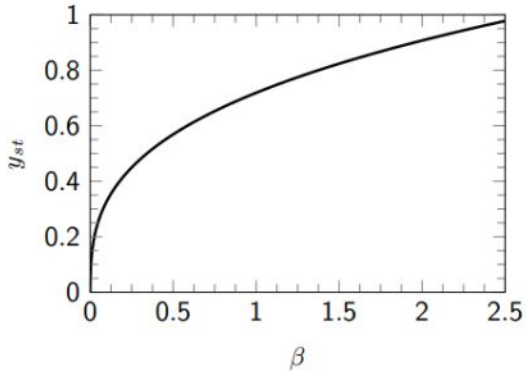

Figure 3.15: Analytical plot of the fixed point y_{st} as a function of the feedback gain β ($\mu = 0.21$, and $\vartheta = -0.12$) (see equation (3.83)).

The eigenvalues that determine the stability of the fixed point are solutions of the following transcendental equation:

$$\lambda = -1 - (\varepsilon + 3\eta y_{st}^2)\frac{1}{\lambda} + \beta e^{-\lambda\nu}. \tag{3.84}$$

Then, limit-cycle oscillation might occur through a Hopf bifurcation if the eigenvalues become pure imaginary values ($\lambda = \pm i\omega$), with ω being the frequency of the corresponding limit-cycle oscillation which satisfies the following transcendental equation:

$$-\omega^2 + i\omega + (\varepsilon + 3\eta y_{st}^2) = i\omega\beta \exp -i\omega\nu. \tag{3.85}$$

Separating the real and imaginary parts, equation (3.85) enables to obtain the following equations:

$$\omega \tan \omega\nu = -\omega^2 + (\varepsilon + 3\eta y_{st}^2) \tag{3.86}$$

$$\beta^2 = 1 + (\frac{-\omega^2 + (\varepsilon + 3\eta y_{st}^2)}{\omega})^2 \tag{3.87}$$

These equations cannot be solved exactly; so, to compute the Hopf bifurcation point, some approximations need to be considered. That is for instance $\tan \omega\nu \simeq \omega\nu$ [21] leads

to the critical frequency:

$$\omega = \sqrt{\frac{(\varepsilon + 3\eta y_{st}^2)}{1+\nu}}. \tag{3.88}$$

Equation (3.88) clearly shows that the frequency of the limit-cycle increases with the cubic-nonlinear parameter η of the system and decreases when the normalized time-delay ν of the system grows. It should be noted that the value of y_{st} is a function of the feedback gain (see equation (3.83) and its plot in Figure 3.15). Therefore, the variation of the feedback gain also affects the frequency of the limit-cycle oscillation. According to Figure 3.15, the frequency will also increases if the feedback gain increases. These analytical results will be numerically confirm in the next section.

3.4.3 Nonlinear dynamics of the simplified CN-OEO

In the previous section, we have demonstrated that the dynamics of the simplified CN-OEO strongly depend on the value of bias parameter ϑ. This is to highlight the importance of the bias parameter ϑ on the dynamics of the simplified CN-OEO. Indeed, it can cancel oscillations in the system for any value greater than or equal to zero. It the goal to prove that information, the plot of the bifurcation diagram of the variable x as a function of ϑ gives the numerical confirmation of this analytical result (Figure 3.16). Starting from negative values of the bias parameter ϑ, it appears that the amplitude of oscillations decreases when the bias parameter ϑ increases and vanishes from $\vartheta = 0$ (Figure 3.16).

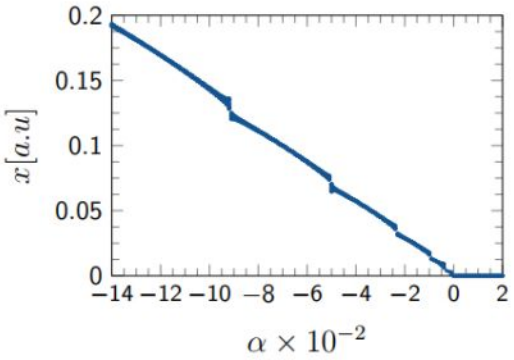

Figure 3.16: Numerical plot of the bifurcation diagram for the variable x of the system as a function of ϑ for $\nu = 53.14$ and $\beta = 1.08$.

For appropriate negative value of the bias parameter ϑ ($\vartheta = -0.12$), the bifurcation diagram in terms of the feedback gain β is displayed in Figure 3.17 (a). It present the general observation of the dynamic of the simplified CN-OEO. It yields that the dynamic presents a limit-cycle oscillation,a doubling of periods to route of chaos. Figure 3.17 (b) presents the Lyapunov exponent which confirms the dynamics of the bifurcation diagram.

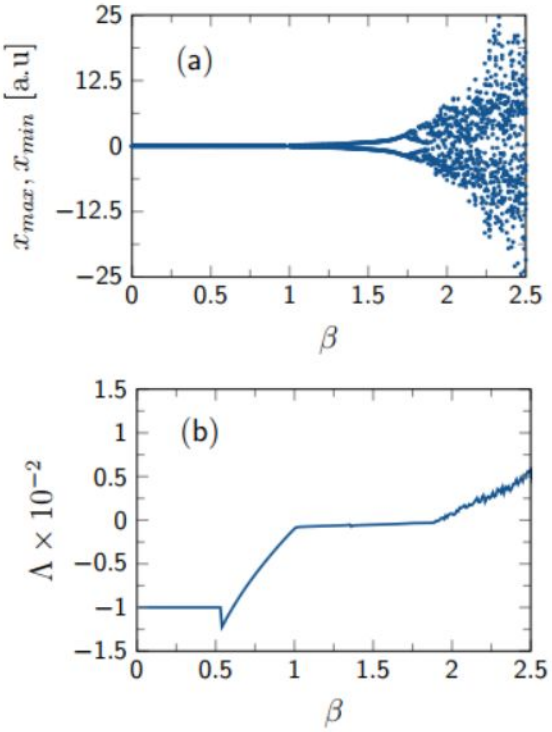

Figure 3.17: (a) Numerical plot of the bifurcation diagram for the variable x. (b) Lyapunov exponent Λ of the system $\nu = 53.14$ and $\alpha = -0.12$.

In order to make a comparison between the simplest OEO or simplified standard OEO and this simplified CN-OEO, the analysis will concern the limit-cycle oscillation. For this purpose, we consider the bifurcation diagram give in Figure 3.18

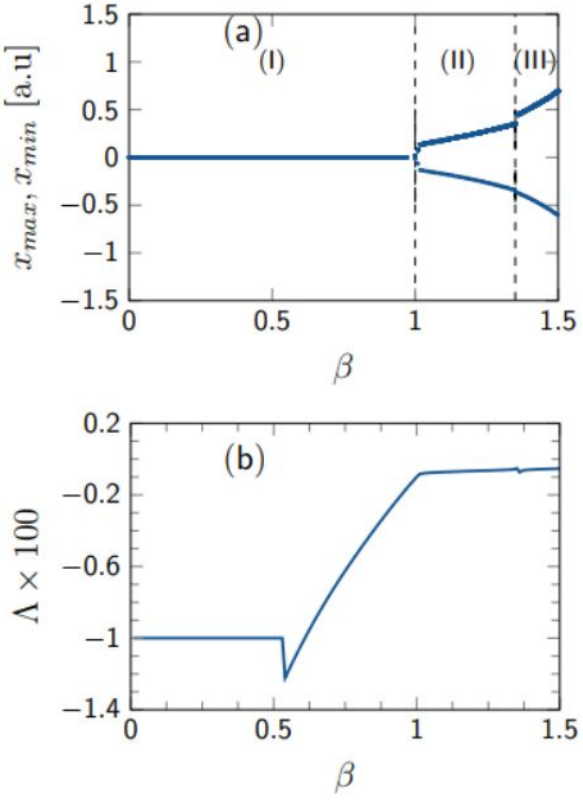

Figure 3.18: (a) Numerical plot of the bifurcation diagram for the variable x. (b) Lyapunov exponent Λ of the system $\nu = 53.14$ and $\alpha = -0.12$.

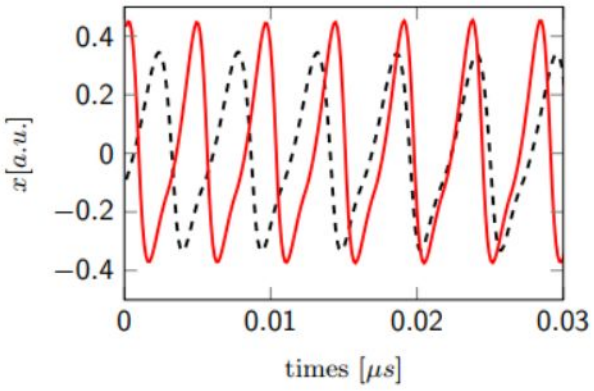

Figure 3.19: Timetraces of the signal around the jump amplitude. The dashed line is the timetrace of the signal for $\beta = 1.35$ (i.e. just before the jump point), and the red one is the timetrace of the signal for $\beta = 1.36$ (i.e. just after the jump point).

In Figure 3.18 (a), it yields that the amplitude of the limit-cycle oscillations grows when β increases. This bifurcation diagram can be divided in three parts. The first part (I) corresponds to $\beta < 1$ where there are not oscillations in the system; the fixed point is exponentially stable and there is no other attractor in the system. This numerical value of

the Hopf point ($\beta \simeq 1$) matches with the analytical result of equation(3.87). The second part (II) correspond to $1 < \beta \leq 1.35$. In this part, one notes the limit-cycle oscillations whose amplitude increases. The third part (III) corresponds to $\beta \geq 1.35$. In this part, the amplitude of the limit-cycle oscillations continues to progressively increase. The second (II) and the third (III) parts are separated by an amplitude jump occurring at $\beta = 1.35$. Figure 3.19 shows the comparison of the signal for two neighboring values of the feedback gain β around the jump point (in particular for $\beta = 1.35$ (dashed) and $\beta = 1.36$ (line)). The signal increases in both the amplitude and the frequency (at $\beta = 1.35$ the amplitude is 0.35 and the frequency is $0.184\,GHz$ while at $\beta = 1.36$ the amplitude is 0.45 and the frequency is $0.216\,GHz$). There is also a phase shift between the two signals emitted before and after the jump point. The signal emitted when $\beta = 1.35$ is in phase-advance over the signal emitted when $\beta = 1.36$. The Lyapunov exponent of Figure 3.18(b) is compatible with the bifurcation diagram of Figure 3.18 (a). The Lyapunov exponent Λ is the same as defined in equation (3.18).

The phase portrait is a suitable tool for evaluating the dynamic of a system. To explore the dynamic of the simplified CN-OEO, we have first plot the phase portraits in the limit-cycle oscillation region. It appears that near the threshold value of Hopf bifurcation (the second part of the bifurcation diagram), the system displays a quasi-sinusoidal oscillation as confirmed by the limit-cycle of Figure 3.20 (a) for $\beta = 1.08$. After the jump, for $\beta = 1.5$ (the third part of the bifurcation diagram), the phase portrait of the system magnifies the slow-fast limit-cycle oscillations (Figure 3.20 (b)).

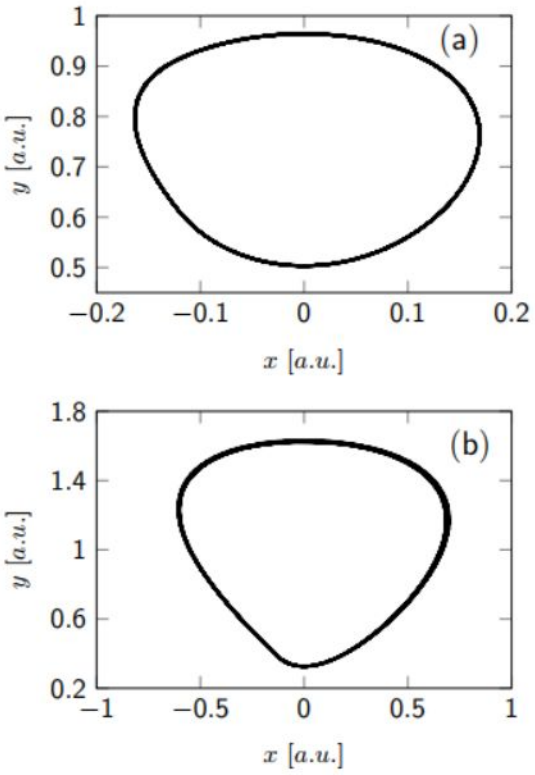

Figure 3.20: Numerical simulations of the CN-OEO-LASER for $\nu = 53.14$ and $\alpha = -0.12$, when β is varied. (a) is quasi sinusoidal oscillations for $\beta = 1.08$, and (b) is slow-fast oscillations for $\beta = 1.5$.

Secondly, to confirm the analysis of the phase portraits, the experimental analysis is carried out. In Figure 3.21, we have displayed the numerical and experimental time traces. For experimental analysis, the polarization voltage is set to $I_{th} - I_{pol} = 0.263\,V$. It can be seen that for low feedback gain, one obtains a quasi-sinusoidal oscillation after the Hopf bifurcation threshold (Figures 3.21 (a) and 3.21 (c)). When the value of the feedback gain increases, it affects the dynamics of the system. In particular, the slow-fast oscillations recorded in this simplified CN-OEO result from alternate passages of accelerated trajectory and slow trajectory in the oscillation (Figures 3.21 (b) and (d)). Figure 3.21 also shows that the frequency of limit-cycle increases as the feedback gain increases (see Figures 3.21 (a) and 3.21 (b)) as predicted by the analytical study (see equation. (3.88)).

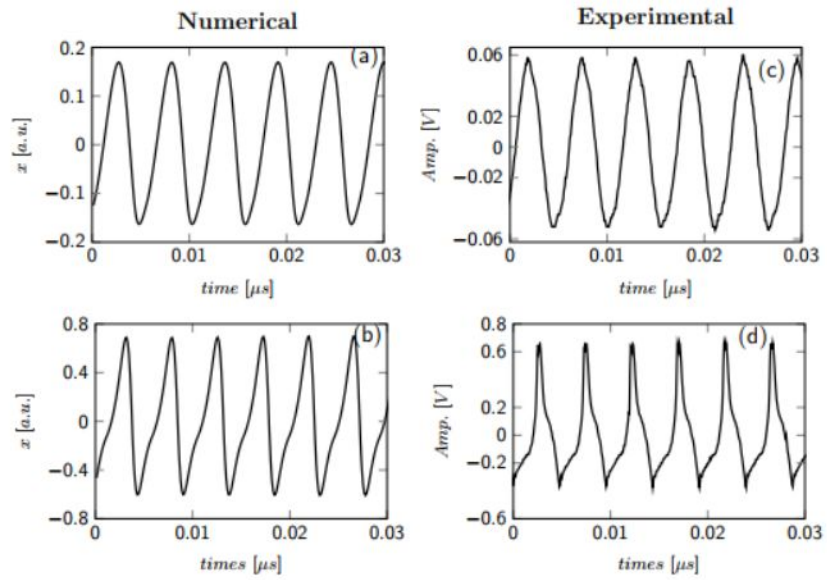

Figure 3.21: Time traces of the simplified CN-OEO. Left column [(a), and (b)]: corresponding numerical simulations from Eqs. (3.76) and (3.77) for $\nu = 53.14$ and $\alpha = -0.12$, when β is varied. (a) is x for $\beta = 1.08$, and (b) is x for $\beta = 1.5$. Right column [(c),and (d)] experimental measurements for $R = 2.5\,k\Omega$, $r = 300\,\Omega$, $C_1 = 270\,pF$, $C_2 = 9.15\,nF$, $T_D = 3.28\mu s$, and $V_{th} - V_{pol} = 1.314\,V$.

It is important to highlight that slow-fast dynamics are responsible for "canard explosions" which are observed in many biological, chemical, mechanical, electronic, optical, and engineering systems [72–75, 77, 78, 81–84].

On the interest of the chaotic region, for the large feedback gain ($\beta > 1.75$), the time-trace show a large difference between the experimental and the numerical results as shows Figure 3.22. This difference is due to the internal dynamics of the laser diode. We conclude that a discrepancy occurs between experimental and numerical records when the feedback gain becomes large.

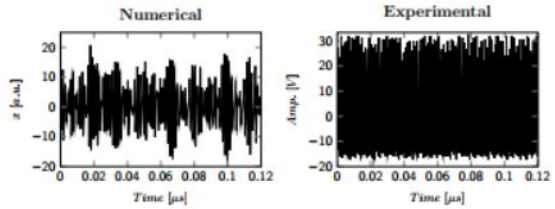

Figure 3.22: Time traces of the experimental and numerical results when the feedback gain become large ($\beta = 2.5$). Other parameters are the same as in Figure 3.21.

At the end of investigation on the simplified CN-OEO, after having proposed the experimental device, have established the equations reflecting the dynamics of limit-cycle oscillations of the system. We can say that the system is efficient and can be used

for several application considering the limit of pumps of the laser diode. In this case specially, we have used the transfer function of the laser in the limit of low pumps. Moreover, the system oscillates only for appropriate negative value of the bias parameter ϑ but it does not regardless any positive value of ϑ. The theoretical analysis of these equations has allowed to realize that the frequency of the system grows with the cubic-nonlinear parameter of the system (η), the feedback gain (β), and decreases when the normalized time-delay (ν) of the system increases. The bifurcation curve has shown that the simplified CN-OEO is dominated by the limit-cycle oscillations, and chaos. These dynamical phenomena (quasi-sinusoidal oscillation, slow-fast oscillation, and chaos) that occurred have been experimentally proven and confirmed. But we mention that when the feedback gain growths it is a discrepancy between experimental and numerical records.

Our simplified CN-OEO is cheaper and constitutes a step towards photonic integrated circuits.

GENERAL CONCLUSION

1- Main Results

In this thesis, the study of optoelectronic oscillator with the Cubic-Nonlinear Band-Pass Filter (CNBPF) has been carried out theoretically and experimentally with the simplified model of that CN-OEO.

Firstly, the Cubic-Nonlinear Band-Pass Filter (CNBPF) have been considered. A mathematical description has been made. The equivalent electrical circuit of this filter has been presented in order to carry out the experiment. The theoretical and experimental studies have shown that this filter is able to run the CN-OEO under the variation of some parameters.

Secondly, the optoelectronic oscillator with the Cubic-Nonlinear Band-Pass Filter (CNBPF) has been analyzed, theoretically, and experimentally. The CNBPF cancels breathers in the dynamics of the OEO, generates quasi-periodic oscillations, slow-fast oscillations, and chaos. The CN-OEO runs in higher frequency than the standard OEO and can operate in narrow-band and wide-band. The CN-OEO is more versatile than the standard one because it generates the same dynamics that are observed in the standard OEO (breathers, relaxation oscillations, and chaos) by tuning some parameters of the CNBPF. The mathematical analysis has shown that the signal frequency of the CN-OEO grow with the cubic-nonlinear parameter and decreases with the normalized time-delay. The numerical and experimental analysis have shown that the Hopf bifurcation was not affected by the use of CNBPF and we always have limit-cycle oscillations and chaos but with high frequency. It is interesting to mention that the transition between limit-cycle oscillations and chaos present crenelated oscillations. In the dynamics of the CNOEO, jumped points have been observed corresponding to where the amplitude decreases first before restarting to increase. The characterization of the CN-OEO in terms of some key parameters have shown that the amplitude and the frequency of the CN-OEO evolve similarly as on the standard OEO but with higher frequency oscillations in primary Hopf bifurcation. A good qualitative agreement has been found between the theoretical and experimental investigations.

Thirdly, the simplified CN-OEO has been presented. It has been investigated mathematically, numerically, and experimentally, in the limit of low pumps of the laser diode. The laser diode is used to perform the electro-optical conversion in the simplified CN-OEO. The goal of this system is to reduce the number of components, the power energy consumption, and the cost of materials. It can also be put as integrated circuits for applications in communication, navigation, and other tech-nological aims. Quasiperiodic and slow-fast oscillations were recorded. We highlighted that slow-fast oscillations are responsible of the phenomena of "canard explosion". The mathematical analysis has shown that the signal frequency of the CN-OEO grows with the cubicnonlinear parameter and decreases with the normalized time-delay. The bifurcation diagram still presents jump

points. Compared to the direct feedback modulation of the standard OEO, the simplified CN-OEO still runs in higher frequencies. As in the simplified standard OEO, in the simplified CN-OEO, the oscillations critically depend of the negative value of the bias voltage parameter. For appropriate value of that bias voltage, we have oscillations in the system. When the feedback gain increases, we see a discrepancy between experimental and numerical results, because the laser diode begins to operate in the limit of high pumps. However, the numerical investigation was closed to experiment in the low pumps regime.

2- Perspectives

This work presents a model of OEO which has a cubic-nonlinear band-pass filter. It can be used for random numbers, for generation chaos-based communication, detection, sensing, and neuromorphic computing.

It would be interesting to investigate later the dynamics of the CN-OEO with a polarized Mach Zehnder in order to explore some new dynamics, to see a possible addition of times scale for new applications of the CN-OEO. Indeed, in this study, the Mach-Zehnder was biased with a DC voltage. We also think to explore its dynamics if it is polarized with an alternative function.

Bibliography

[1] **Neyer, A.**, **Vogues, E.**, *Dynamics of electroopic bistable devices with delayed feedback*. IEEE J. Quantun Electron. 104(12), 2009–2015 (1982)

[2] **Yao, X. S.**, **Maleki L.**, *High frequency optical subcarrier generator*. Electron. Lett, 19(11), 1525–1526, (1994)

[3] **Yao, X. S.**, **Maleki L.**, *Optoelectronic microwave oscillator*. J. Opt. Soc. Amer. B. 13(8) , 1725–1735, (1996)

[4] **Maleki, L.**, *The Optoelectronic Oscillator*, Nature Photon 5(12), 728-730, (2011)

[5] **Chembo, Y. K.**, **Larger, L.**, **Bendoula, R.**, **Colet, P.**, *Effects of gain and bandwidth on the multimode behavior of optoelectronic microwave oscillators*. Optics Express 16(12) 9067-9072, (2008)

[6] **Chembo, Y. K.**, **Larger, L.**, **Tavernier, H.**, **Bendoula, R.**, **Rubiola, E.**, **Colet, P.**, *Dynamic instabilities of microwaves generated with optoelectronic oscillators*. Optics Lett. 32 2571-2573, (2007)

[7] **Chembo, Y. K.**, **Larger, L.**, **Colet, P.**, *Nonlinear dynamics and spectral stability of optoelectronic microwave oscillators*. IEEE journal of quantum electronics 44(9) 858-866, (2008)

[8] **Romeira, B.**, **Javaloyes, J.**, **Figueiredo, J.M.L.**, **Ironside, C.N.**, **Cantu, H.I.**, **Kelly, A.E.**, *Delayed feedback dynamics of Liénard-type resonant tunneling-photodetector optoelectronic oscillators*. IEEE J. of Quantum Electron. 49(1), 31-42 (2013)

[9] **Chengui, G.R.G.**, **Talla, A. F.**, **Talla Mbé, J.H.**, **Coillet, A.**, **Saled, K.**, **Larger, L.**, **Woafo, P.**, **Chembo, Y.K.**, *Theoretical and experimental study of slow-scale hopf limit-cycles in laser-based wideband optoelectronic oscillators*. J. Opt. Soc Amer. B, Opt. Phys., 31(10), 2310-2316 (2014)

[10] **Talla Mbé, J.H.**, **Talla, A. F.**, **Chengui, G.R.G.**, **Coillet, A.**, **Larger, L.**, **Woafo, P.**, **Chembo, Y.K.**, *Mixed-mode oscillations in slow-fast delayed optoelectronic systems*. Phys. Rev. E, 91(012902), (2015)

[11] **Munnelly, P.**, **Lingnau, B.**, **Karow, M.M.**, **Heindel, T.**, **Kamp, M.**, **Hofling, S.**, **Ludge, K.**, **Schneider, C.**, **Reitzenstein, S.**, *On-chip optoelectronic feedback in a micropillar laser-detector assembly*, Optica, 4(3), 303-306 (2017)

[12] **Talla Mbé, J.H.**, **Woafo, P.**, **Chembo, Y.K.**, *A normal form method for the determination of oscillations characteristics near the primary Hopf bifurcation in bandpass optoelectronic oscillators: Theory and experiment.* Chaos,29,(033104), (2019)

[13] **Murphy, T.E.**, **Cohen, AB.**, **Ravoori, B.**, **Schmitt, KR.**, **Setty, AV.**, **Sorrentino, F.**, **Williams, CR.**, **Ott, E.**, **Roy, R.** *Complex dynamics and synchronization of delayed-feedback nonlinear oscillators.* Philos.Trans. Roy. Soc. A Math. Phys. Eng. Sci. 368, 343-366 (2010)

[14] **Callan, K.E.**, **Illing, L.**, **Gao, Z.**, **Gauthier, D.J.**, **Scholl, E.**, *Broadband chaos generated by an optoelectronic oscillator.* Phys. Rev Lett., 104, 113901 (2010)

[15] **Martinez-Llinas, J.**, **Colet, P.**, **Erneux, T.**, *Tuning the period of square-wave oscillations for delay-coupled optoelectronic systems.* Phys. Rev. E, Stat. Phys. Plasmas Fluids Relat. Interdiscip. Top. 89, 042908 (2014)

[16] **Jiang, X.**, **Cheng, M.**, **Luo, F.**, **Deng,L.**, **Fu, S.**, **Ke, C.**, **Zhang, M.**, **Tang, M.**, **Shum, P.**, **Liu, D.**, *Electro-optic chaotic system based on the reverse-time chaos theory and a nonlinear hybrid feedback loop.* Opt. Express 24, 28804-28814 (2016)

[17] **Weicker, L.**, **Erneux, T.**, **Jacquot, M.**, **Chembo, Y.**, **Larger, L.**, *Crenelated fast oscillatory outputs of tow-delay electro-optic oscillator.* Phys. Rev. E, 85 026206,(2012)

[18] **Williams, C.R.S.**, **Murphy, T.E.**, **Roy, R.**, **Sorrentino, F.**, **Dahms, T.**, **Scholl, E.**, *Experimental observations of group synchrony in a system of chaotic optoelectronic oscillators.* Phys. Rev. Lett. 110, 064104, (2013)

[19] **Weicker, L.**, **Erneux,T.**, *Slow-Fast dynamics of time-delayed electro-optic oscillator.* Philos. Trans. Roy. Soc. A. Math., Phys. 371(1999), 20120459, (2013)

[20] **Talla, A. F.**, **Marteninghi, R.**, **Woafo, P.**, **Chembo, Y. K.**, *Breather and pulse package dynamics in multinonlinear electrooptical systems with delay feedback.* IEEE Phton. J., 8(4) 7803608, (2016)

[21] **Kouomou, Y. C.**, **Colet, P.**, **Gastaud, N.**, *Chaotic Breathers in Delayed ElectroOptical Systems.* Phys. Rev. Lett. 95, 203903-1âĂŞ 203903-4, (2005)

[22] **Ha, M.**, **Chembo, Y.K.**, *Nonlinear dynamics of continuously tunable optoelectronic oscillators based on stimulated Brillouin amplification.* Optics Express 29(10), 14630-14648 (2021)

[23] **Talla, A.F.**, **Martinenghi, R.**, **Talla. Mbé, J. H.**, **Saleh, K.**, **Lin, G.**, **Chengui, G.R.G.**, **Coillet, A.**, **Woafo, P.**, **Chembo, Y.K.**, *Analysis of phase locking in narrow-band optoelectronic oscillators with intermediate frequency.* IEEE photonics journal. 2425957, (2016)

[24] **Chembo, Y. K.**, *Laser-based optoelectronic generation of narrowband microwave chaos for radar and radio-communication scrambling.* Opt. lett., 3431-3434, (2017)

[25] **Yang, J.**, **Jin-Long, Y.**, **Yao-Tian, W.**, **Li-Tai, Z.**, **En-Ze, Y.**, *An optical domain combined dual-loop optoelectronic oscillator.* IEEE. Photon. Technol. Lett., 19(11), 807-809 (2007)

[26] **Kim, J. M.**, **Cho, D.**, *Optoelectronic oscillator stabilized to an intraloop Fabryperot cavity by a dual servo system.* Optics Express 18(14) 14905-14912, (2010)

[27] **Li, W.**, **Yao,J.**, *An optically tunable optoelectronic oscillator.* J. Lightw. Technol.,28(18) 2640-2645, (2010)

[28] **Ozdur, I.**, **Akbulut, M.**, **Hoghooghi, N.**, **Mandridis, D.**, **Piracha, M.U.**, **Delfyett,P.J.**, *Optoelectronic loop desing with 1000 finesse Fabry-Perot etalon.* IEEE. Photon. Technol. Lett. 27(2) 213-216, (2014)

[29] **Jia, S.**, **Yu,J.**, **Wang, J.**, **Wu,Q.**, **Huang, G.**, **Yang, E.**, *A novel optoelectronic oscillator based on wave-length multiplexing.* J. Opt. Soc. Amer. B., 13(8) 1725-1735, (1996)

[30] **Zhang, Y.**, **Hou, D.**, **Zhao, J.**, *Long-term frequency stabilization of an optoelectronic oscillator using phase-locked loop.* J. Lightw. Technol., 32(13) 2408-2414, (2014)

[31] **Nguimdo, R.M.**, **Chembo, Y.K.**, **Colet, P.**, **Larger, L.**, *On the phase noise performance of nonlinear double-loop optoelectronic microwave oscillators.* IEEE J. Quantum Electron., 48(11) 1415-1423, (2012)

[32] **Okasuga, O.**, **Adles, E.J.**, **Levy, E.C.**, **Zhou, W.**, **Carter, G.M.**, M, C.R., **Hrowitz,M.**, *Spurious mode reduction in dual injection-locked opotoelectronic oscillators.* Opt. Exp. 19(7) 5839-5854, (2011)

[33] **Saleh, K.**, **Lin, G.**, **Chembo, Y. K.**, *Effect of laser coupling and active stabilization on the phase noise performance of optoelectronic microwave oscillator based on whispering-gallery mode-oscillator resonators.* IEEE photon. J. 7(1), Art.(5500111), (2015)

[34] **Lelievre, O.**, **Crozatier, V.**, **Berger, P.**, **Baili, G.**, **Liopis, O.**, **Dolfi, D.**, **Nouchi, P.**, **Goldfard, F.**, **Bretenaker, F.**, **Morvan, L.**, **Pillet, G.**, *A model designing ultralow noise single-and dual-loop 10-GHz optoelectronic oscillators.* J.Lightw. Technol., 35(20) 4366-4374, (2017)

[35] **Paquot, Y.**,**Dupont, F.**, **Smerieri, A.**, **Dambre,J.**, **Schrauwen, B.**, **Haelterman, M.**, **Massar, S.**, *Optoelectronic reservoir computing.* Sci. Rep., 2(287), (2012)

[36] **Bruner, D.**, **Soriano, M.C.**, **Mirasso, C.R.**, **Fischer, I.**, *Parallel photonic information processing at gigabyete per second data rates using transient states.* Nature Commun., 4 1364, (2013)

[37] **Duport, F.**, **Smerieri, A.**, **Akrout, A.**, **Haelterman, M.**, **Massar,S.**, *Fully analogue photonic reservoir computer.* Sci. Rep., 6(6) 22381, (2016)

[38] **Barron-Zambrano, J.H.**, **Torres-Huitzil, C.**, *FPGA implementation of a configurable neuromorphic CPG-based locomotion controller Neural.* Netw., 45 50-61 (2013)

[39] **Soriano, M.C.**, **Ortin, S.**, **Larger, L.**, **Mirasso, C.R.**, **Fischer, I.**, **Pesquera, L.**, *Optoelectronic reservoir computing: Tackling noise-induced performance degradation.* Opt. Express, 21(1) 12-20, (2013)

[40] **Larger, L.**, **Baylon-Fuentes, A.**, **Martinenghi, R.**, **Udaltsov, V.S.**, **Chembo, Y.K.**, **Jacquot, M.**, *High-speed photonic reservoir computing using a time-delaybase architecture: million words per second classification.* Phys. Rev. X, 7(011015), (2017)

[41] **Wang, S.**, **Fang, N.**, **Wang, L.**, *Signal recovery based on optoelectronic reservoir computing for high speed optical fiber communication system.* Opt. Commun. 495(15) 127082, (2021)

[42] **Dai, H.**, **Chembo, Y.K.**, *Classification of IQ-Modulated Signals Based on Reservoir Computing With Narrowband Optoelectronic Oscillators. IEEE J. Quantum Electron.* 57(3), 1-8, (2021)

[43] **Zou, X.**, **Xinkai, L.**, **Li, W.**, **Li, P.**, *Optoelectronic oscillators(OEOs) to sensing, measurement, and detection.* IEEE J. Quantum Electron. 52(1)0601116, (2016)

[44] **Yao, J.**, *Optoelectronic oscillator for high speed and high resolution optical sensing.* J. lightw. Technol., 35(16) 3489-3497, (2017)

[45] **Wu, B., et al.**, *Magnetic field sensor based on dual- frequency optoelectronic oscillators using cascaded magnetostrictive alloy a fiber Bragg grating-Fabry Perot and fiber Bragg grating-Fabry Perot filters.* Optics Express, 26(21), 27628-27638, (2018)

[46] **Argyris, A.**, **Syvridis, D.**, **Larger, L.**, **Annovazzi-Lodi, V.**, **Colet, P.**, **Fischer, I.**, **G arcia-Ojalvo, J.**, **Mirasso, C.R.**, **Pesquera, L.**, **Shore, K.A.**, *Chaos-based communication at high bit rates using commercial fibre-optic links.* Nature 438, 343-346, (2015)

[47] **Uchida, A.**, *Optical Communication With Chaotic Lasers: Applications of Nonlinear Dynamics and Synchronization.* New York, NY, USA: Wiley (2012)

[48] **Ai, J.**, **Wang, L.**, **Wang, J.**, *Secure communications of CAP-4 and OOK signals over MMF based on electro-optics chaos.* Opt. Lett.,42(18) 3662-3665, (2017)

[49] **Nguimdo, R.M.**, **Lavrov, R.**, **Colet, P.**, **Jacquot, M.**, **Chembo, Y.K.**, **Larger, L.**, *Effects of fiber dispertion on broadband chaos communication implemented by electro optic nonlinear delay phase dynamics.* J. Lightw. Technol., 28(18) 2688-2689, (2010)

[50] **Talla Mbé, J.H.**, **Atchoffo, N.W.**, **Tchitnga, R.**, **Woafo, P.**, *Dynamics of Time-Delayed Optoelectronic Oscillators With Nonlinear Amplifiers and Its Potential Application to Random Numbers Generation.* IEEE J. of Quantum Electron., 57(5), 5000507, (2021)

[51] **Zou, F.**, **Zou, L.**,**Yang, B.**, **Ma, Q.**, **Zou, X.**, **Zou, J.**, **Chen, S.**, **Milosevic, D.**, **Cao, Z.**, **Liu,H.**, *Optoelectronic Oscillator for 5G Wireless Networks and Beyond.* J. Phys. D: Appl. Phys., **DOI: 10.1088/1361-6463/ac13f2**, (2021)

[52] **Ly, A.**, **Auroux, V.**, **Khayatzadeh, R.**, **Gutierrez, N.**, **Fernandez, A.**, **Llopis, O.**, *Highly spectrally pure 90GHz signal synthesis using a coupled optoelectronic oscillator.* IEEE photon. Technol. Lett., 30(14), 1313-1316, (2018)

[53] **Huang, L.**, **Deng, L.**, **Fu, S.**, **Tang, M.**, **Cheng, M.**, **Zhang, M.**, **Liu, D.**, *Stable and compact dual-loop optoelectronic oscillator using self-polarization-stabilization technique and multicore fiber.* J. Lightw. Technol., 36(22) 5196-5202, (2018)

[54] **Shi, M.**, **Yi, L.**, **Wei, W.**, **Hu, W.**, *Generation and phase noise analysis of a wide optoelectronic oscillator with ultra-high resolution based on stimulated Brillouin scattering.* Optics Express, 5(13) 16113-16124, (2018)

[55] **Zhou, P.**, **Pan, S.**, **Guo, R.**, **Zhu, D.**, **Zhang, F.**, **Zhao, Y.**, *A compact optoelectronic oscillator based on an electroabsorption modulated laser.* IEEE journal of quantum electronics 26(1) 86-88, (2014)

[56] **Tang J., et al.**, *Integrated optoelectronic oscillator Optics Express.* 26(9) 12257-12265, (2018)

[57] **Larger L.**, *Complexity in electro-optic delay dynamics: Modelling, design and applications*. Philos. Trans. Roy. Soc. A, Math. Phys. Eng. Sci., 371(20120464) 12257-12265, (2013)

[58] **Goune Chengui, G.R.**, **Talla Mbé, J.H.**, **Talla, A.F.**, **Woafo, P.**, **Chembo, Y.K.**, *Dynamics of Optoelectronic Oscillators With Electronic and Laser Nonlinearities*. IEEE J. of Quantum Electron, 54(1), (2018)

[59] **Kouayep, R.B.**, **Talla, A.F.**, **Talla Mbé, J.H.**, **Woafo, P.**, *Bursting oscillations in Colpitts oscillator and application in optoelectronics for the generation of complex optical signals*. Opt. and Quant. Electron. 52 1-13, (2020)

[60] **Hao, T.**, **Liu, Y.**, **Tang, J.**, **Cen, Q.**, **Li, W.**, **Zhu, N.**, **Dai, Y.**, **Capmany, J.**, **Yao, J.**, **Li, M.**, *Recent advances in optoelectronic oscillators*. Adv. Photonics 2(4), (2020)

[61] **Chembo, Y.K, Brunner, D.**, **Jacquot, M.**, **Larger, L.**, *Optoelectronic oscillators with time-delayed feedback*. Rev. Mod. Phys. 91(3), 035006 (2019)

[62] **Zhou, P.**, **Pan, S.**, **Zhu, D.**, **Guo, R.**, **Zhang, F. Zhao, Y.**, *A compact optoelectronic oscillator based on an electroabsorption modulated laser*. IEEE Photon, Technol. Lett., 26(1)86-88, (2014)

[63] **Nguewou-Hyousse, H.**, **Chembo, Y.K.**, *Nonlinear dynamics of miniature optoelectronic oscillators based on whispering-gallery mode electrooptical modulators*. Optics Express, 28(21)30656-30674, (2020)

[64] **Nguewou-Hyousse, H.**, **Chembo, Y.K.**, *Stochastic Analysis of Miniature Optoelectronic Oscillators Based on Whispering-Gallery Mode Electrooptical Modulators*. IEEE Phot. Journal, 13(3), 3000110, (2021)

[65] **Chang, C.Y.**, **Choi, D.**, **Michael, A.L.**, **Wishon, J.**, **Merghem, K.**, **Ramdane,A.**, **Lelarge, F.**, **Martinez, A.**, **Citrin, D.S.**, *A multi- GHz chaotic optoelectronic oscillator based on laser terminal voltage*. Appl. Phys. Lett.108(19). (191109) 27628-27638, (2016)

[66] **Chang, C.Y.**, **Choi, D.**, **Michael, A.L.**, **Wishon, J.**, **Merghem, K.**, **Ramdane, Lelarge, F.**,**Martinez, A.**, **Citrin, D.S.**, *Tunable X-band optoelectronic oscillators on external-cavity semiconductor laser*. IEEE J. of Quantum Electron., 53(3), (2017)

[67] **Goune Chengui, G.R.**, **Woafo, P.**, **Chembo, Y.K.**, *The Simplest Laser-Based Optoelectronic Oscillator: An experimental and Theoreticcal Study*. J. Lightw. Technol., 0733-8724, (2015)

[68] **Mboyo Kouayep, R.**, **Talla, A. F.**, **Talla Mbé, J.H.**, **Woafo, P.**, *Bursting oscillations in Colpitts oscillator and application in optoelectronics for the generation of complex optical signals.* Springer Science+Business Media, LLC, part of Springer Nature (2020).

[69] **Fatoorehchi H.**, **Abolghasemi H.**, **Zarghami R.**, *Analytical approximate solutions for a general nonlinear resistor-nonlinear capacitor circuit model.* Appl. Math. Model 39(19) 6021-6039, (2015)

[70] **Kwuimy K.**, **Woafo P.**, *Experimental realization and simulations a self-sustained macro electromechanical system.* Mech. Res. Commun., 37 106-110, (2010)

[71] **Fregien G.**, **Van Wyk J. D.**, *Nonlinear capacitor in snubber circuits for GTO thyristors.* IEEE Trans. Power. Electron, 7 (2) 425-429, (1992)

[72] **Hayashi C.**, *Nonlinear oscillations in physical systems.* New York, NY, USA: McGraw Hill (1964)

[73] **Broms, M.**, **Kaper, T.J.**, **Rotstein, H.G.**, *Introduction to focus issue: Mixed mode oscillations: Experiment, computation, and analysis.* Chaos 18(1) 015101, (2008)

[74] **Petrov, V.**, **Scott, SK.**, **Showalter, K.**, *Mixed-mode oscillations in chemical systems.* J. Chem. Phys. 97(9) 6191-6198, (1992)

[75] **Huack, T.**, **Scheinder, F.W.**, *Mixed-mode and quasiperiodic oscillations in the peroxidase reaction.* J. Chem. Phys. 97 391, (1993)

[76] **Vo, T.**, **Bertram, R.**, **Tabak, J.**, **Wechselberger, M.**, *Mixed mode oscillations as a mechanism for pseudo-plateau bursting.* J. Comput. Neurosci 28 443, (2010)

[77] **Sekikawa, M.**, **Inaba, N.**, **Yoshinaga, T.**, **Hikihara T.**, *Period-doubling cascades of canards from the extended Bonhoeffer-Van der Pol oscillator.* Phys. Lett. A 3743745, (2010)

[78] **Duhram, J.**, **Moehlis, J.**, *Feedback control of canards.* Chaos 18 015110, (2008)

[79] **Shchepakina, E.**, **Korotkova, O.**, *Canard explosion in chemical and optical systems.* Discrete Continuous Dyn. Syst. 18(2), 495-512 (2013)

[80] **Talla Mbé, J.H.**, **Woafo, P.**, *Modulation of distributed feedback (DBF) laser diode with a autonomous ChuaâĂŹs circuit: Theory and experiment.* Opt. Lasers Techn. 145- 152, (2018)

[81] **Talla Mbé, J.H.**, **Woafo, P.**, **Fotsin, H.B**, *Experimental direct modulation of a laser diode with a Van der Pol circuit and applications.* Opt. Eng. 58(6) 066114, (2019)

[82] **Qin, BW.**, **Kwok-Wai C.**, **Algaba, A.**, **Alejandro J.**, **Rodriguez-Luis.**, *Asymptotic expansions for a degenerate canard explosion.* Physica D: *Nonlinear Phenomena* 418, 132841, (2021)

[83] **Qin, BW.**, **Chung, KW.**, **Algaba, A.**, *High-order study of the canard explosion in an aircraft ground dynamics model.* Nonlinear Dyn 100, 1079-1090 (2020)

[84] **Qin, BW.**, **Kwok-Wai C.**, **Algaba, A.**, **Alejandro J.**, **Rodriguez-Luis.**, *High-order analysis of canard explosion in Brusselator equations.* International Journal of Bifurcation and Chaos 30(05), 2050078, (2020)

[85] **Desroches, M.**, **Guckenheinmer, J.**, **Krauskopf, B.**, **Kuehn, C.**,**Osinga, H.M, Wechselberger, M.**, *Mixed-mode oscillations with multiple times scales.* SIAM Rev. 54(2) 211-288, (2012)

[86] **Goedgebuer, J.-P.**, **Larger L.**, **Porte H.**, **Delorme F.**, *Chaos in wavelength with a feedback tunable laser diode.* Phys. Rev. E 57 2795-2798, (1998)

[87] **Chembo Y. K.**, *Optoelectronic oscillators with time-delayed feedback.* Reviews of modern physics 91 2795-2798, (2019)

[88] **Cohen, A., B.**, **Ravoori, B.**, **Murphy, T., E.**, **Roy, R.**, *Using Synchranization for Prediction of High-Dimensional Chaotic Dynamics.* Phys. Rev. Lett. 101, 154102 (2008)

[89] **Appeltant, L.**, **Soriano, M. C.**, **Van der Sande, G.**, **Danckaert, J. Massar, S.**, **Dambre J.**, **Schrauwen B.**, **Mirasso C. R.**, **Fischer I.**, *Information processing using a single dynamical node as complex system.* Nat. Commun. 2, (468), (2011)

[90] **Duport, F., A**. **Smerieri, A. Akrout, M. Haelterman, Massar, S. Fully** *Analogue photonic reservoir computer.* Sci. Rep. 6 (22381) (2016a)

[91] **Yao, X. S.**, **Maleki L.**, *High frequency optical subcarrier generator, Electron.* Lett. 30, 1525-1526 (1994)

[92] **Narendra, S.**, **Aloka, S.**, *Chaos-based secure communication system using logistic map.* Elsevier, Opt. Lasers Eng. 43, 398-404 (2009)

[93] **Jing Z.**, **Wang M.**, **Tang Yu**, **Ding Qi**, **Wang C.**, **Huang X.**, **Desheng C.**, **Yan F.**, *Angular Velocity Measurement With Improved Scale Factor Based on a*

Wideband-Tunable Optoelectronic Oscillator. IEEE transactions on instrumentation and measurement, 70: 1-19 (2021)

[94] **Toan, T. P.**, and **Van Y. V.**, *A study on measuring refractive index by using an optoelectronic oscillator*. IEEE, (2014)

[95] **Okusaga O.**, **Pritchett J.**, **Sorenson R.**, **Zhou W.**, **Berman M.,** *The OEO as an Acoustic Sensor*. IEEE 66-68 (2013)

[96] **Nayfeh A.H.**, *The method of Normal Forms*. Wiley-VCH, 2011.

[97] **Tian Y**, **Yu P.**, *An explicit recursive formula for computing the normal forms associated with semisimple cases*. Commun. Nonlinear Sci. Numer. Simulat., 19:2294-2308 (2014)

[98] **YuanGuang Z**, **ZaiHua W.**, *Delayed Hopf bifurcation in time-delayed slow-fast systems*. Sci. China Tech. Sci., 53:656-663 (2010)

[99] **Illing L.**, **Gauthier, D. J.**, *Hopf bifurcations in time-delay systems with bandlimited feedback*. Physica D 210, 180-202 (2005)

[100] **Carr J.**, **Muncaster,R. G.**, *The application of centre manifolds to amplitude Expansions*. Jounal of Differential Equations, 50 , 280-288 (1983)

[101] **Talla Mbé J. H., Jimmi** Offset Phase OEO, Name of repository, Dataset. **https://www.researchgate.net/publication/334455155-JimmiâĹŠOffsetPhaseâĹŠOEO**. (2019)

[102] **Hoffman J.D.**, **Marcel Dekker**, *Numerical Methods for Engineers and Scientists*. New-York, 372-373, (2001)

[103] **Teukolsky S.A**. and **Flannery B.P.**, *Numerical recipe/ the art scientific computing*. W.H. press, Cambridge University Press, New York, (2007)

[104] **Talla Mbé, J.H**.,and **Woafo, P.** *Study of the effect of the offset phase in timedelay electro-optical systems*. Chaos 30, 093130 (2020)

[105] **Yanhong Z.**, **Xiaofeng J.**, **Hao C.**, **Shilie Z.**, **Xianmin Z.** *High-sensitivity temperature sensor based on an optoelectronic oscillator*. Optical Society of America, ID 213010, (2014)

[106] **Koualong Tchuissa, M. K.**, **Talla Mbé J. H.**, **Tatietse Tamo T.**, *Efficient Sensings of Temperature, Refractive Index, and Distance Measurement using the cubic-Nonlinear Optoelectronic oscillators*. Optical and Quantum Electronics, 54(311), (2022)

LIST OF PUBLICATIONS

1. **Deumi Kamaha J. S.**,Talla Mbé J. H., Noubissie S. Fotsin H. B., and Woafo P. **"Dynamics of optoelectronic oscillators with band-pass filter and laser nonlinearities: theory and experiment"**: Journal of Optical and Quantum Electronics, 54(178), (2022)

2. **J.S. Deumi Kamaha,** J.H. Talla Mbé, H.B. Fotsin, and P. Woafo **"Routes to chaos and characterization of the limit-cycle oscillations in wideband time-delayed optoelectronic oscillators with nonlinear filters"**: Journal of the Optical Society of America B, 37(11) A75-A85, (2020)

3. Talla Mbé J. H., **Deumi Kamaha J. S.**, Chembo Y. K., and Woafo P. **"Dynamics of wideband time-delayed optoelectronic oscillators with nonlinear filters"**: IEEE Journal of the Quantum Electronics, 55(4) 5000106, (2019)

Optical and Quantum Electronics (2022) 54:178
https://doi.org/10.1007/s11082-022-03546-6

Dynamics of optoelectronic oscillators with band-pass filter and laser nonlinearities: theory and experiment

Juliette S. D. Kamaha[1] · Jimmi Hervé Talla Mbé[2] · Samuel Noubissie[3] · Hilaire Bertrand Fotsin[2] · Paul Woafo[1]

Received: 13 August 2021 / Accepted: 22 January 2022

Abstract
In this paper, we present a study of a simplified optoelectronic oscillator (OEO) that features both the laser and the filter nonlinearities. We show that this optoelectronic oscillator depicts the phenomena of quasi-sinusoidal oscillations when the feedback gain is small, relaxation and chaos oscillations when the feedback gain increases. It is analytically confirmed that the frequencies of the limit-cycle oscillations increase with the cubic-nonlinear term and the feedback gain but decrease with the time-delay of the system. The experimental measurements are qualitatively in agreement with the theoretical and numerical analysis.

Keywords Optoelectronic oscillator · Nonlinear band-pass-filter · Quasi-sinusoidal oscillation · Slow–fast oscillation

1 Introduction

Optoelectronic oscillators (OEOs) are autonomous nonlinear hybrid systems made of an optical and electrical path. After the pioneering work of Neyer and Vogues (1982), OEOs have been widely studied from the fundamental viewpoint (see for example Romeira et al. 2013; Chengui et al. 2014; Talla Mbé et al. 2015; Munnelly et al. 2017; Talla Mbé et5 al. 2019; Murphy et al. 2010; Callan et al. 2010; Martinez-Llinas et al. 2014; Jiang et al. 2016; Weicker et al. 2012; Williams et al. 2013; Weicker and Erneux 2013; Talla et al. 2016; Chembo et al. 2005; Ha and Chembo 2021), to several applications such as ultra-stable microwave generations (Talla et al. 2015; Chembo 2017; Yao 1994; Yang et al. 2007; Yao 1996; Kim and Cho 2010; Li and Yao 2010; Ozdur et al. 2014; Jia et al. 1996; Chembo

✉ Jimmi Hervé Talla Mbé
jhtallam@yahoo.fr

[1] Laboratory of Modeling and Simulation in Engineering, Biomimetics and Prototypes, Department of Physics, University of Yaoundé I, P. O. Box 812 Yaoundé, Cameroon

[2] Research Unit of Condensed Matter, Electronics and Signal Processing, Department of Physics, University of Dschang, P.O. Box 67 Dschang, Cameroon

[3] Research Unit of Industrial Systems Engineering and Environment (RU-ISEE), Fotso-Victor University Institute of Technology, University of Dschang, Bandjoun, Cameroon

Published online: 21 February 2022

et al. 2008; Zhang et al. 2014; Nguimdo et al. 2012; Okasuga et al. 2011; Saleh et al. 2015; Lelievre et al. 2017), neuromorphic computing (Paquot et al. 2012; Bruner et al. 2013; Duport et al. 2016; Barron-Zambrano and Torres-Huitzil 2013; Soriano et al. 2013; Larger et al. 2017; Wang et al. 2021; Dai and Chembo 2021), measurement, sensing, detections (Zou et al. 2016; Yao 2017; Wu 2018), chaos-based communications (Argyris et al. 2015; Uchida 2012; Ai et al. 2017; Nguimdo et al. 2010), random numbers generation (Talla Mbé et al. 2021), 5-G wireless communication (Zou et al. 2021), and others technological aims (Ly et al. 2018; Huang et al. 2018; Shi et al. 2018). The richness of the dynamics and applications of OEOs have been recently reviewed in Hao et al. (2020), Chembo et al. (2019).

But, achieving these applications is not the only objective. Another one is to meet the strict requirements of future communications, radars, navigation, satellite systems, and embedded systems. In that scope, compact OEOs were designed (Maleki 2011; Zhou et al. 2014; Nguewou-Hyousse and Chembo 2020, 2021). Besides, instead of using the intensity or phase modulator, other electro-optic devices such as electroabsorption modulated laser were used to simultaneously perform three functions namely lasing, photodetection, and intensity modulation (Zhou et al. 2014) or direct optical feedback onto the laser-diode was also proposed to perform intensity modulation (Chang et al. 2016, 2017). However, another alternative consists to reduce the number of components in the OEO oscillator. The pioneering work in this orientation focused on the electrical-to-optical signal conversion where the seeding laser diode itself was used to perform that conversion through its light-intensity piecewise function instead of an intensity or phase-modulator and termed simplest OEO (Goune Chengui et al. 2015). Only quasi-sinusoidal and relaxation oscillations were recorded with a standard bandpass filter (Goune Chengui et al. 2015). The drawback of this method is the reduction of the bandwidth which is scaled from kHz to tens of GHz (with external modulator) to kHz to few GHz (with seeding laser-diode) imposed by the relaxation oscillation frequency of the laser diode. Nevertheless, this method brings a general benefit in the physical equipment, power consumption, and it reduces the cost and congestion (Goune Chengui et al. 2015, 2018; Talla Mbé and Woafo 2018; Talla Mbé et al. 2019a). Later on, to emulate the complex dynamics in this simplified architecture of OEO, other authors proposed cascading the electrical path of the simplest OEO with additional nonlinear electronic oscillators such as the Van der Pol (Goune Chengui et al. 2018) and the Colpitts (Kouayep et al. 2020) oscillators. Novel dynamics not encountered in standard and simplest OEOs were recovered namely, bursting, anti-monotonicity, and pulse packages.

Recently, another architecture of OEO in which the electric path features a cubic-nonlinear response was investigated and called the cubic-nonlinear optoelectronic oscillator (CN-OEO) (Talla Mbé et al. 2019b; Kamaha et al. 2020). In that architecture, an intensity Mach-Zehnder modulator translates the RF electrical signal of a cubic-nonlinear bandpass filter (CNBPF) into the optical domain. The dynamics of that OEO was shown to be more versatile than the standard OEO and generated higher frequency and amplitude of limit-cycle oscillations in a larger range of the feedback gain. The frontier transition between the limit-cycle oscillations and the chaotic motion shown crenelated oscillations. The idea addressed in this paper is to perform the simplified benchmark of the CN-OEO. It is also shown that as in the simplest OEO (Goune Chengui et al. 2015), for low values of the feedback gain, the dynamics essentially exhibits limit-cycle oscillations of two kinds: quasi-sinusoidal and slow–fast but rather with higher frequency. Slow–fast dynamics are trajectories of a dynamical system in which there are alternately successive large and small amplitudes in the time evolution (Talla Mbé et al. 2015). It is important to highlight that slow–fast dynamics are responsible for "canard explosions"which are observed in many

biological, chemical, mechanical, electronic, optical, and engineering systems (Broms et al. 2008; Petrov et al. 1992; Huack and Scheinder 1993; Vo et al. 2010; Sekikawa et al. 2010; Duhram and Moehlis 2008; Shchepakina and Korotkova 2013; Qin et al. 2021, 2020, 2020; Desroches et al. 2012). But, for high values of the feedback gain, chaotic dynamics is recorded.

This paper is organized as follows: Sect. 2 presents the experimental system along with its mathematical model. Section 3 deals with the stability analysis of this OEO. Section 4 presents the numerical simulations and the experimental results. The last section contains the concluding remarks.

2 System and model

The experimental device of our simplified CN-OEO presented in Fig. 1 is made of a telecommunication continuous-wave distributed feedback laser diode source with wavelength $\lambda_L \simeq 1.55$ µm, threshold current $I_{th} = 15.2$ mA which is pumped with a current under the form of $I_{pol} + I_{RF}(t)$, where I_{pol} is the polarization current, $I_{RF}(t)$ is the time-varying radio-frequency (RF) current. Then, the laser outputs the power $P(t)$ that is retarded through an optical delay line yielding a time-delay T_D. An InGaAs fast photodiode (PD) converts the delayed light into an electrical signal V_{in} with a conversion factor $S = 4.75$ V/mW. This electrical signal V_{in} undergoes a nonlinear transformation by propagating through the cubic-nonlinear band-pass filter (CNBPF). A voltage subtractor (VS) probes the voltage

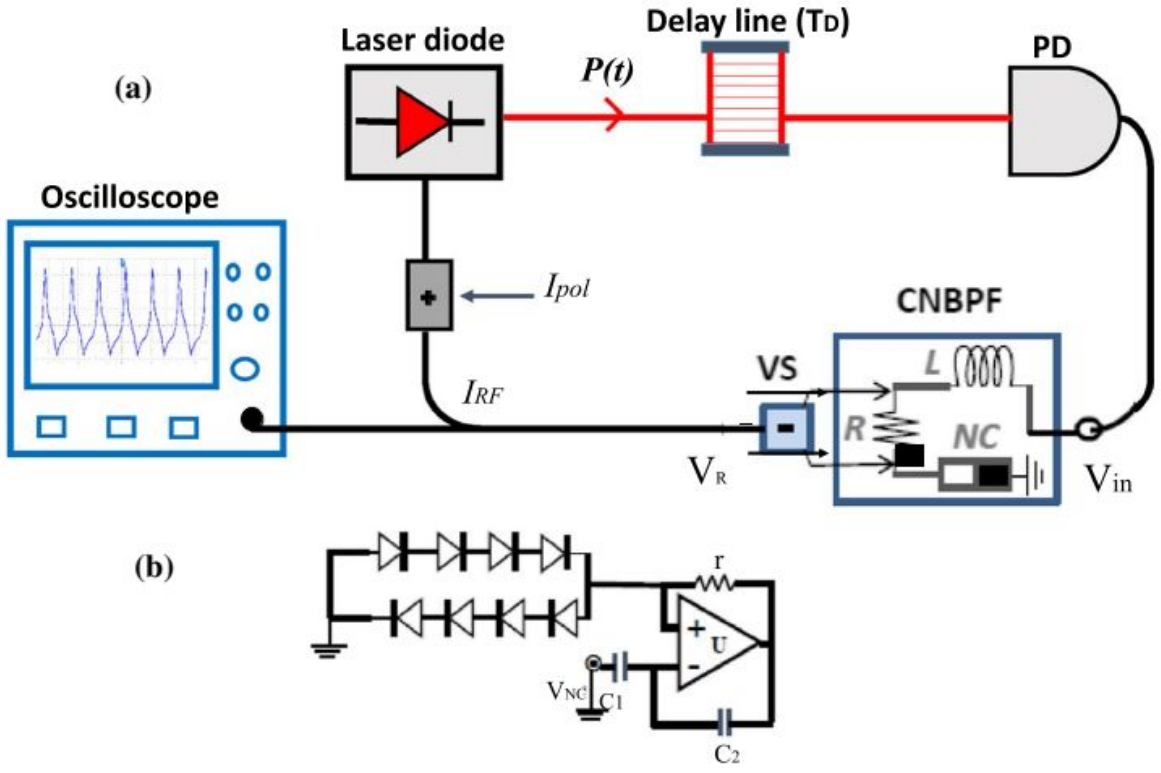

Fig. 1 (Color online) **a** Experimental setup of OEO featuring both the laser and the filter nonlinearities and **b** nonlinear capacitor (NC). The laser used is a DFB telecom laser diode (~ 1.55 µm) with a threshold injection current $I_{\text{th}} = 15.2$ mA. The 656 m optical fiber induces a time-delay of $T_D = 3.28$ µs. PD is Photodiode, I_{pol} is the polarization current; I_{RF} is the current from feedback loop. CNBPF refers to cubic-nonlinear band-pass Filter, VS is the voltage subtractor

across the resistor of the CNBPF V_R which is then converted into the RF current ($I_{RF} = \frac{V_R}{R_Z}$, where $R_Z = 50\,\Omega$ is the characteristic impedance used for the voltage-to-intensity conversion). This current is combined with the polarization current I_{pol} (bias current) to feed the laser which therefore performs the electrical-to-optical conversion.

The CNBPF is implemented using two capacitors $C_{1,2}$, two resistors (r, R), an operational amplifier U, a mixed assembly of eight simple junction diodes, and one coil L. The thermal voltage of these junction diodes is $V_T = 25\,\text{mV}$, the number of junction diodes in series is $n = 4$, and the inverse saturation current is $I_s = 5\,\mu\text{A}$.

Applying the Kirchhoff's laws to Fig. 1b, the relationship between the input (V_{in}) and the output (V_R) of the CNBPF yields (Talla Mbé et al. 2019b):

$$\begin{aligned} V_R + \frac{L}{R}\frac{dV_R}{dt} + \left[\frac{1}{c_1} - \frac{nV_T}{2rI_sc_2}\right]\frac{1}{R}\int_0^t V_R\,ds \\ + \frac{nV_TG^2}{6}\left[\frac{1}{2rI_sc_2R}\right]^3\left(\int_0^t V_R\,ds\right)^3 = GV_{\text{in}}, \end{aligned} \tag{1}$$

where t is the time and G is the gain of the voltage subtractor. In the limit of the low pumps of the laser diode, the laser diode which performs the conversion of the electrical-to-optical signal has the following nonlinear transfer function (Goune Chengui et al. 2015, 2018; Talla Mbé and Woafo 2018; Talla Mbé et al. 2019a):

$$P(t) = \begin{cases} 0 & for \quad I_{RF}(t) \le I_0 \\ \mu[I_{RF}(t) - I_0] & for \quad I_{RF}(t) > I_0, \end{cases} \tag{2}$$

The parameter $\mu = \eta_d h\nu$ is the laser conversion slope with η_d as the quantum efficiency, h the Planck constant, and ν the laser carrier frequency. The experimental value of the parameter μ is $\mu = 0.21\,\text{W/A}$. In Eq. (2), $I_0 = I_{th} - I_{pol}$. Taking into account the time-delay experienced by the optical signal during its flow inside the delay line, the voltage provided by the photodiode is related to such retarded optical signal as follows:

$$V_{\text{in}} = KSP(t - T_D), \tag{3}$$

where K is a dimensional factor standing for the overall losses (electrical and optical) in the feedback loop. Inserting Eq. (3) into Eq. (1), our simplified CN-OEO is described by the piecewise cubic-nonlinear integro-differential delayed equation [see Eq. (2) for $P(t - T_D)$]:

$$\begin{aligned} V_R + \frac{L}{R}\frac{dV_R}{dt} + \left[\frac{1}{c_1} - \frac{nV_T}{2rI_sc_2}\right]\frac{1}{R}\int_0^t V_R\,ds \\ + \frac{nV_TG^2}{6}\left[\frac{1}{2rI_sc_2R}\right]^3\left(\int_0^t V_R\,ds\right)^3 = GKSP(t - T_D). \end{aligned} \tag{4}$$

Then, considering $I_{RF}(t - T_D) = \frac{V_R(t-T_D)}{R_Z}$ and setting the dimensionless voltage $x = \frac{V_R(t)}{V_0}$, with V_0 a reference voltage ($V_0 = 1\,V$), Eq. (4) yields:

$$\begin{aligned} x + \frac{L}{R}\frac{dx}{dt} + \left[\frac{1}{c_1} - \frac{nV_T}{2rI_sc_2}\right]\frac{1}{R}\int_0^t x\,ds \\ + \frac{nV_TG^2V_0^2}{6}\left[\frac{1}{2rI_sc_2R}\right]^3\left(\int_0^t x\,ds\right)^3 = \frac{KSG}{R_Z}P\left[x(t - T_D) - \frac{R_ZI_0}{V_0}\right]. \end{aligned} \tag{5}$$

According to Eq. (5), the system is characterized by four timescales which are the time-delay T_D, the high cut-off time τ, the low cut-off time θ, and the nonlinear timescale ρ that are explicitly given as:

$$T_D = \frac{n_0 L}{c}, \tag{6}$$

$$\tau = \frac{L}{R}, \tag{7}$$

$$\theta = R[\frac{1}{c_1} - (nV_T/2rI_s c_2)]^{-1}, \tag{8}$$

$$\rho = \frac{nV_T G^2 V_0^2}{6}\left[\frac{1}{2rI_s c_2 R}\right]^3. \tag{9}$$

In Eq. (6), L and $n_0 = 1.5$ are respectively the length and the refraction index of the optical delay line, and c is the velocity of light in the vacuum. Therefore, Eq. (5) can be rewritten as:

$$x + \tau\frac{dx}{dt} + \frac{1}{\theta}\int_0^t x\,ds + \rho\left(\int_0^t x\,ds\right)^3 = \frac{KSG}{R_Z}P\left[x(t - T_D) - \frac{R_Z I_0}{V_0}\right]. \tag{10}$$

To facilitate the dynamical analysis, it is preferable to recast Eq. (10) under the form of a coupled delay differential equations. For this purpose, we introduce the new variable $y = \frac{1}{\tau}\int_0^t x\,ds$ and the dimensionless times $t' = \frac{t}{\tau}$, $\nu = \frac{T_D}{\tau}$ (the normalized time-delay). Equation (10) is therefore transformed into a piecewise slow–fast dynamical system with x as the fast variable while y is the slow variable:

$$\dot{y} = x \tag{11}$$

$$\dot{x} + x + \varepsilon y + \eta y^3 = \beta P(x_\nu - \alpha) = \begin{cases} 0 & if\ x_\nu - \alpha \le 0 \\ \beta(x_\nu - \alpha) & if\ x_\nu - \alpha > 0. \end{cases} \tag{12}$$

Here $x_\nu = x(t' - \nu)$ is the time-delayed variable, and the feedback gain $\beta = \frac{KSG\mu}{R_Z}$. The small quantity $\varepsilon = \frac{\tau}{\theta}$ is the cut-off times ratio, the parameter $\eta = \rho\tau^3$ stands for the cubic-nonlinear parameter, $\alpha = \frac{R_Z I_0}{V_0}$ is the bias parameter. In this article, except the tunable parameter G, other parameters are compatible with the experimental values taken as $L = 0.1$ mH, $r = 300\,\Omega$, $R = 1.62\,k\Omega$, $C_1 = 270\,pF$, $C_2 = 9.15$ nF, and $T_D = 3.29\,\mu$s.

3 Stability analysis

The fixed-point (x_{st}, y_{st}) of the set of Eqs. (11) and (12) obeys to the following:

$$x_{st} = 0 \tag{13}$$

$$y_{st}^3 + \frac{\varepsilon}{\eta} y_{st} = \begin{cases} 0 & if \ \ \alpha \geq 0 \\ \frac{-\alpha\beta}{\eta} & if \ \ \alpha < 0. \end{cases} \cdot \tag{14}$$

It appears from Eq. (14) that the solution critically depends on the sign of the bias parameter α.

3.1 Case of $\alpha \geq 0$

In this case, Eq. (14) becomes:

$$y_{st}^3 + \frac{\varepsilon}{\eta} y_{st} = 0. \tag{15}$$

There is a unique trivial fixed point $(x_{st}, y_{st}) = (0, 0)$ because $\frac{\varepsilon}{\eta}$ is a positive quantity. The stability of this trivial fixed point is determined by the value of the eigenvalue λ which satisfies the following second-order polynomial:

$$\lambda^2 + \lambda + \varepsilon = 0, \tag{16}$$

and is calculated as:

$$\lambda_{\pm} = \frac{-1 \pm \sqrt{1 - 4\varepsilon}}{2}. \tag{17}$$

The trivial fixed point (0, 0) is unconditionally stable since the cut-off time is known to be very small ($\varepsilon \ll 1$) in broadband OEO (in the present work, $\varepsilon = 9.7 \times 10^{-4}$). Therefore, no oscillation is expected regardless of the value of the feedback gain β.

3.2 Case of $\alpha < 0$

According to Eq. (14), the fixed point y_{st} is the root of the following third-order polynomial:

$$y_{st}^3 + \frac{\varepsilon}{\eta} y_{st} = \frac{-\alpha\beta}{\eta}, \tag{18}$$

which solutions are non-trivial if $\beta \neq 0$ and is unique since $\frac{\varepsilon}{\eta}$ is a positive quantity. Figure 2 shows that y_{st} grows with the feedback gain β. It can be noticed that the values of the fixed point parabolically grows with the feedback gain.

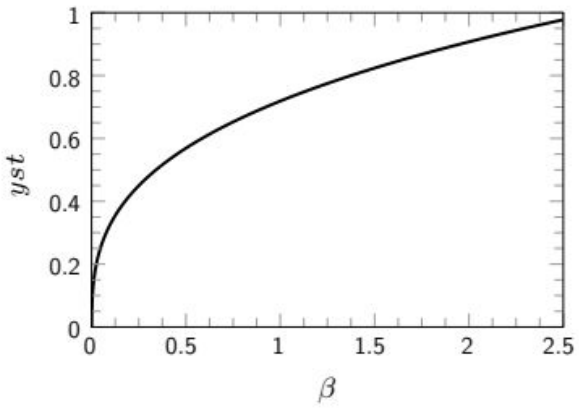

Fig. 2 Analytical plot of the fixed point y_{st} as a function of the feedback gain β ($\mu = 0.21$, and $\alpha = -0.12$) [see Eq. (18)]

The eigenvalues that determine the stability of the fixed point are solutions of the following transcendental equation:

$$\lambda = -1 - \left(\varepsilon + 3\eta y_{st}^2\right)\frac{1}{\lambda} + \beta e^{-\lambda\nu}. \tag{19}$$

Then, limit-cycle oscillation might occur through a Hopf bifurcation if the eigenvalues become pure imaginary values ($\lambda = \pm i\omega$), with ω being the frequency of the corresponding limit-cycle oscillation which satisfies the following transcendental equation:

$$-\omega^2 + i\omega + \left(\varepsilon + 3\eta y_{st}^2\right) = i\omega\beta \exp -i\omega\nu. \tag{20}$$

Separating the real and imaginary parts, Eq. (20) enables to obtain the following equations:

$$\omega \tan \omega\nu = -\omega^2 + \left(\varepsilon + 3\eta y_{st}^2\right) \tag{21}$$

$$\beta^2 = 1 + \left(\frac{-\omega^2 + \left(\varepsilon + 3\eta y_{st}^2\right)}{\omega}\right)^2 \tag{22}$$

These equations cannot be solved exactly; so, to compute the Hopf bifurcation point, some approximations need to be considered. That is for instance $\tan \omega\nu \simeq \omega\nu$ (Chembo et al. 2005) leads to the critical frequency:

$$\omega = \sqrt{\frac{(\varepsilon + 3\eta y_{st}^2)}{1+\nu}}. \tag{23}$$

Equation (23) clearly shows that the frequency of the limit-cycle increases with the cubic-nonlinear parameter η

of the system and decreases when the normalized time-delay ν of the system grows. It should be noted that the value of y_{st} is a function of the feedback gain [see Eq. (18) and its plot in Fig. 2]. Therefore, the variation of the feedback gain also affects the frequency of the limit-cycle oscillation. According to Fig. 2, the frequency will also increases if the feedback gain increases. These analytical results will be numerically confirm in the next section.

4 Nonlinear dynamics

The previous analytical analysis has highlighted the importance of the bias parameter α on the dynamics of the simplified CN-OEO. Indeed, it can cancel oscillations in the system for any value greater than or equal to zero. The plot of the bifurcation diagram of the variable x as a function of α gives the numerical confirmation of this analytical result (Fig. 3). Starting from negative values of the bias parameter α, it appears that the amplitude of oscillations decreases when the bias parameter α increases and vanishes from $\alpha = 0$ (Fig. 3).

For appropriate negative value of the bias parameter α ($\alpha = -0.12$), the bifurcation diagram in terms of the feedback gain β is displayed in Fig. 4a. It yields that the amplitude of this limit-cycle oscillations grows when β increases. This bifurcation diagram can be divided in three parts. The first part (I) corresponds to $\beta < 1$ where there are not

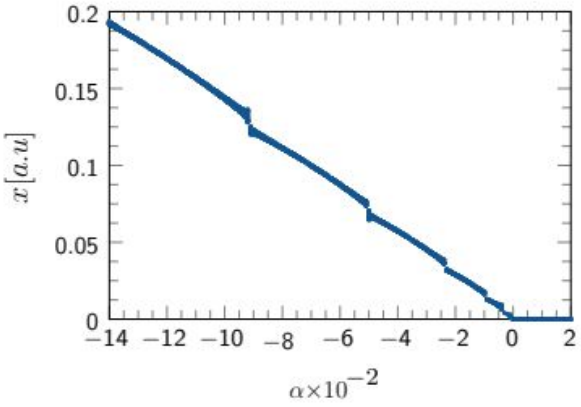

Fig. 3 Numerical plot of the bifurcation diagram for the variable x of the system as a function of α for $\nu = 53.14$ and $\beta = 1.08$

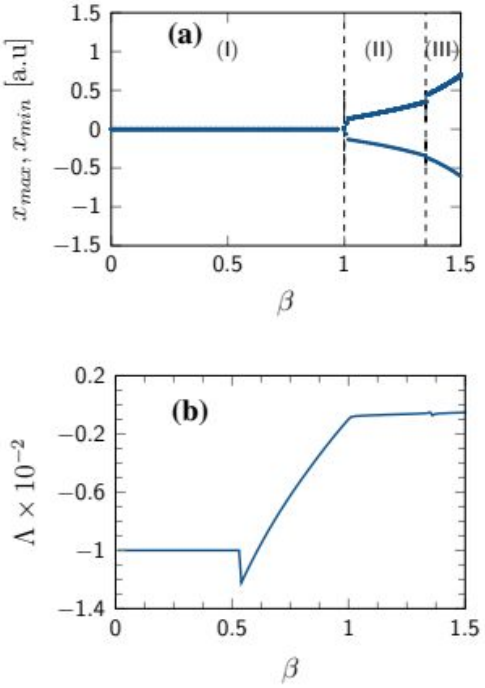

Fig. 4 **a** Numerical plot of the bifurcation diagram for the variable x. **b** Lyapunov exponent Λ of the system $\nu = 53.14$ and $\alpha = -0.12$

oscillations in the system; the fixed point is exponentially stable and there is no other attractor in the system. This numerical value of the Hopf point ($\beta \simeq 1$) matches with the analytical result of Eq. (22). The second part (II) correspond to $1 < \beta \leq 1.35$. In this part, one notes the limit-cycle oscillations whose amplitude increases. The third part (III) corresponds to $\beta \geq 1.35$. In this part, the amplitude of the limit-cycle oscillations continues to progressively increase. The second (II) and the third (III) parts are separated by an amplitude jump occurring at $\beta = 1.35$. Figure 5 shows the comparison of the signal for two neighboring values of the feedback gain β around the jump point [in particular for $\beta = 1.35$ (dashed) and $\beta = 1.36$ (line)]. The signal increases in both the amplitude and the frequency (at $\beta = 1.35$ the amplitude is 0.35 and the frequency is 0.184 GHz while at $\beta = 1.36$ the amplitude is 0.45 and the frequency is 0.216 GHz). There is also a phase shift between the two signals emitted before and after the jump point. The signal emitted when $\beta = 1.35$ is in phase-advance over the signal emitted when $\beta = 1.36$. The Lyapunov exponent of Fig. 4b is compatible with the bifurcation diagram of Fig. 4a. The Lyapunov exponent Λ is known to be a almost null quantity for

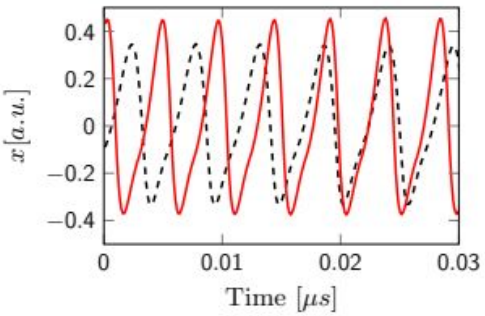

Fig. 5 Timetraces of the signal around the jump amplitude. The dashed line is the timetrace of the signal for $\beta = 1.35$ (i.e. just before the jump point), and the red one is the timetrace of the signal for $\beta = 1.36$ (i.e. just after the jump point)

periodic and quasi-periodic behaviors and strictly negative for fixed points. The Lyapunov exponent is defined as Goune Chengui et al. (2018), Talla Mbé et al. (2019b):

$$\Lambda = \lim \frac{1}{t} \ln \left[\frac{|\delta x(t)|}{|\delta x(t_0)|} \right], \tag{24}$$

with $\delta x(t)$ being a linear perturbation of the system.

To explore the slow–fast dynamics of the simplified CN-OEO, the phase portraits are analyzed. Indeed, near the threshold value of Hopf bifurcation (the second part of the bifurcation diagram), the system displays a quasi-sinusoidal oscillation as confirmed by the limit-cycle of Fig. 6a for $\beta = 1.08$. After the jump, for $\beta = 1.5$ (the third part of the bifurcation diagram), the phase portrait of the system magnifies the slow–fast limit-cycle oscillations (Fig. 6b).

To corroborate our previous results, the experimental analysis is carried out. In Fig. 7, we have displayed the numerical and experimental timetraces. For experimental analysis, the polarization voltage is set to $I_{th} - I_{pol} = 0.263\,\text{V}$. It can be seen that for low feedback gain, one obtains a quasi-sinusoidal oscillation after the Hopf bifurcation threshold (Fig. 7a, c). When the value of the feedback gain increases, it affects the dynamics of the system. In particular, the slow–fast oscillations recorded in this simplified CN-OEO result

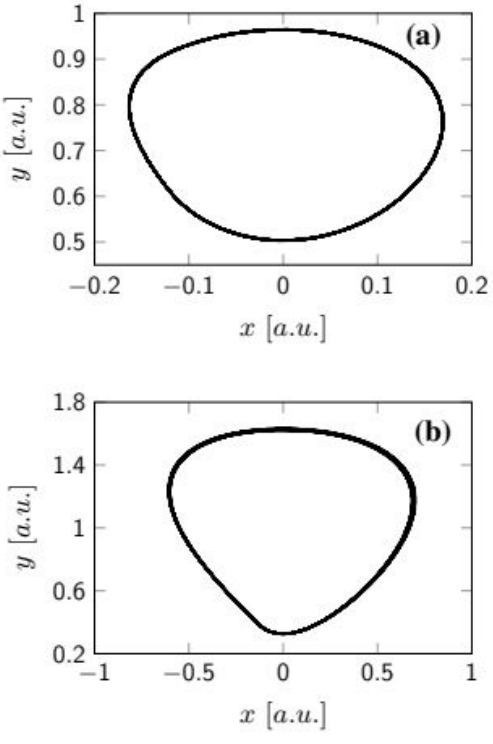

Fig. 6 Numerical simulations of the CN-OEO-LASER for $\nu = 53.14$ and $\alpha = -0.12$, when β is varied. **a** Is quasi sinusoidal oscillations for $\beta = 1.08$, and **b** is slow–fast oscillations for $\beta = 1.5$

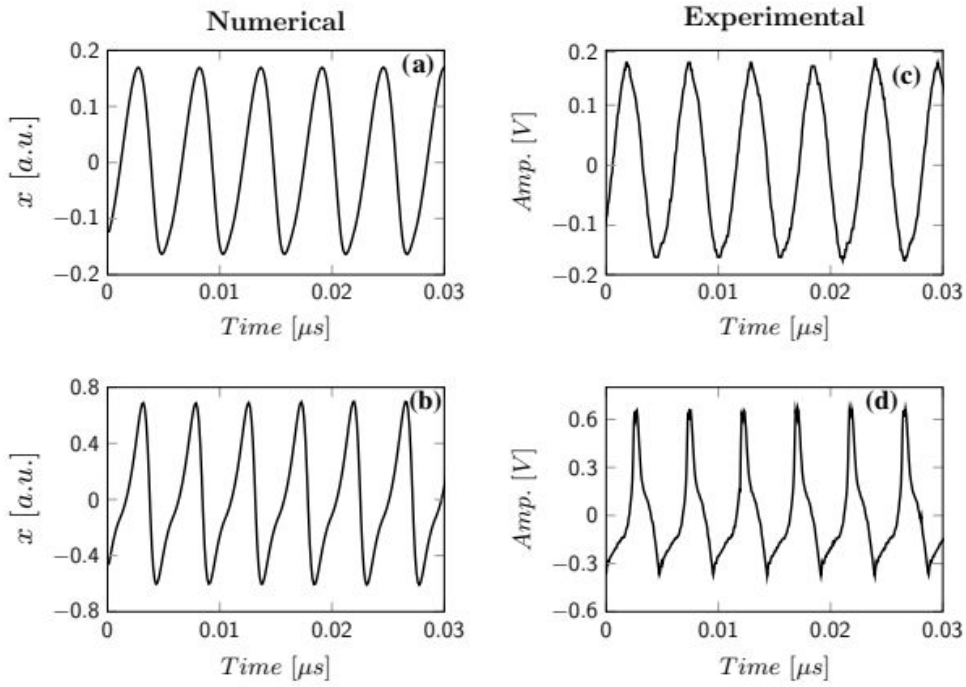

Fig. 7 Timetraces of the simplified CN-OEO. Left column [(**a**, **b**)]: corresponding numerical simulations from Eqs. (11) and (12) for $\nu = 53.14$ and $\alpha = -0.12$, when β is varied. **a** is x for $\beta = 1.08$ and **b** is x for $\beta = 1.5$. Right column [(**c**, **d**)] experimental measurements for $R = 2.5\,\mathrm{k\Omega}$, $r = 300\,\Omega$, $C_1 = 270\,\mathrm{pF}$, $C_2 = 9.15\,\mathrm{nF}$, $T_D = 3.28\,\mu\mathrm{s}$, and $V_{th} - V_{pol} = 1.314\,\mathrm{V}$

from alternate passages of accelerated trajectory and slow trajectory in the oscillation (Fig. 7b, d). Figure 7 also shows that the frequency of limit-cycle increases as the feedback gain increases (see Fig. 7a, b) as predicted by the analytical study [see Eq. (23)]. It is necessary to mention that other dynamics than limit-cycle oscillations were also recorded at large values of the feedback gain ($\beta > 1.75$). For instance, when β crosses the value of 1.75, the bifurcation diagram plotted from the set of Eqs. (11) and (12) presents a period-doubling route to Chaos as confirmed by the Lyapunov exponent (see Fig. 8a, b). But, the timetraces show a large difference between the experimental and the numerical results at those higher values of the feedback gain (see Fig. 9). Indeed, for the same value of the feedback gain, both numerical and experimental timetraces unveil chaotic motion but with a difference in the amplitude distribution. This is because, at large feedback gains, it could not be legitimate to consider that the output power of the laser diode $P(t)$ adiabatically follows the pump current $I(t)$ via the nonlinear function [see Eq. (2)]. Then, the internal dynamics of the laser diode (coupled rate equations for carrier and photon densities) should be considered (Tang and Liu 2001, 2003; Chen et al. 2018).

5 Conclusion

In this work, we have investigated an OEO with the laser diode and cubic-nonlinear band-pass filter (CNBPF) nonlinearities. After having proposed the experimental device, we have established the equations reflecting the dynamics of limit-cycle oscillations of the system. Moreover, the system oscillates only for appropriate negative value

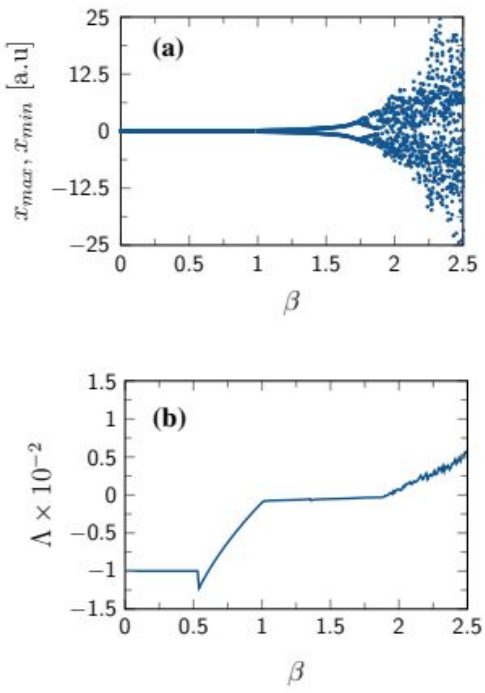

Fig. 8 Numerical plots of the bifurcation diagram (**a**) and the corresponding Lyapunov exponent (**b**). Both display a period-doubling route to chaos for large values of the feedback gain ($\beta > 1.75$)

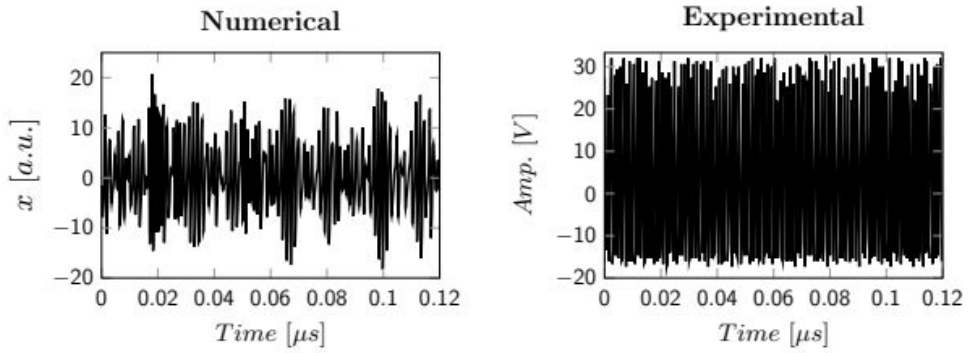

Fig. 9 Timetraces of the experimental and numerical results when the feedback gain become large ($\beta = 2.5$). Other parameters are the same as in Fig. 7

of the bias parameter α but it does not regardless any positive value of α. The theoretical analysis of these equations has allowed to realize that the frequency of the system grows with the cubic-nonlinear parameter of the system (η), the feedback gain (β), and decreases when the normalized time-delay (ν) of the system increases. The bifurcation curve has shown that for low values of the feedback gain, the simplified CN-OEO is dominated essentially by the limit-cycle oscillations. These dynamical phenomena (quasi-sinusoidal oscillation and slow–fast oscillation) that occurred have been experimentally proven and confirmed. But, due to the internal dynamics of the laser diode, a discrepancy occurs between the experimental and numerical records when the feedback gain becomes large. Our simplified CN-OEO is cheaper and constitutes a step towards photonic integrated circuits. Future work will address the phase noise performance of our system (Brian et al. 2021; Nguimdo et al. 2012).

Acknowledgements The authors would like to acknowledge Della Tamin (South Africa) for providing some experimental equipments.

References

Ai, J., Wang, L., Wang, J.: Secure communications of CAP-4 and OOK signals over MMF based on electro-optics chaos. Opt. Lett. **42**(18), 3662–3665 (2017)

Argyris, A., Syvridis, D., Larger, L., Annovazzi-Lodi, V., Colet, P., Fischer, I., Garcia-Ojalvo, J., Mirasso, C.R., Pesquera, L., Shore, K.A.: Chaos-based communication at high bit rates using commercial fibre-optic links. Nature **438**, 343–346 (2015)

Barron-Zambrano, J.H., Torres-Huitzil, C.: FPGA implementation of a configurable neuromorphic CPG-based locomotion controller. Neural. Netw. **45**, 50–61 (2013)

Brian, S., Romanelli, M., Bouhier, S., Frein, L., Alouini, M., Vallet, M.: Low phase noise direct-modulation optoelectronic oscillator. IEEE J. Lightw. Technol. (2021). https://doi.org/10.1109/JLT.2021.3111703

Broms, M., Kaper, T.J., Rotstein, H.G.: Introduction to focus issue: mixed mode oscillations: experiment, computation, and analysis. Chaos **18**(1), 015101 (2008)

Bruner, D., Soriano, M.C., Mirasso, C.R., Fischer, I.: Parallel photonic information processing at gigabyete per second data rates using transient states. Nat. Commun. **4**, 1364 (2013)

Callan, K.E., Illing, L., Gao, Z., Gauthier, D.J., Scholl, E.: Broadband chaos generated by an optoelectronic oscillator. Phys. Rev. Lett. **104**, 113901 (2010)

Chang, C.Y., Choi, D., Michael, A.L., Wishon, J., Merghem, K., Ramdane, A., Lelarge, F., Martinez, A., Citrin, D.S.: Tunable X-band optoelectronic oscillators on external-cavity semiconductor laser. IEEE J. Quantum Electron. **53**(3), 16 (2017)

Chang, C.Y., Choi, D., Michael, A.L., Wishon, J., Merghem, K., Ramdane, A., Lelarge, F., Martinez, A., Citrin, D.S.: A multi- GHz chaotic optoelectronic oscillator based on laser terminal voltage. Appl. Phys. Lett.**108**(19) Art. (191109) 27628–27638 (2016)

Chembo, Y.K., Brunner, D., Jacquot, M., Larger, L.: Optoelectronic oscillators with time-delayed feedback. Rev. Mod. Phys. **91**(3), 035006 (2019)

Chembo, Y.K., Larger, L., Bendoula, R., Colet, P.: Effects of gain and bandwidth on the multimode behavior of optoelectronic microwave oscillators. Opt. Express **16**(12), 9067–9072 (2008)

Chembo, Y.K., Colet, P., Gastaud, N.: Chaotic breathers in delayed electro-optical systems. Phys. Rev. Lett. **95**, 203903 (2005)

Chembo, Y.K.: Laser-based optoelectronic generation of narrowband microwave chaos for radar and radio-communication scrambling. Opt. Lett. **42**(17), 3431–3434 (2017)

Chen, G., Lu, D., Guo, L., Zhao, W., Huang, Y., Zhao, L.: Frequency-tunable OEO using a DFB laser at period-one oscillations with optoelectronic feedback. IEEE Photon. Tech. Lett. **30**(18), 1593–1596 (2018)

Chengui, G.R.G., Talla, A.F., Talla Mbé, J.H., Coillet, A., Saled, K., Larger, L., Woafo, P., Chembo, Y.K.: Theoretical and experimental study of slow-scale hopf limit-cycles in laser-based wideband optoelectronic oscillators. J. Opt. Soc. Am. B **31**(10), 2310–2316 (2014)

Dai, H., Chembo, Y.K.: Classification of IQ-modulated signals based on reservoir computing with narrowband optoelectronic oscillators. IEEE J. Quantum Electron. **57**(3), 1–8 (2021)

Desroches, M., Guckenheinmer, J., Krauskopf, B., Kuehn, C., Osinga, H.M., Wechselberger, M.: Mixed-mode oscillations with multiple times scales. SIAM Rev. **54**(2), 211–288 (2012)

Duhram, J., Moehlis, J.: Feedback control of canards. Chaos **18**, 015101 (2008)

Duport, F., Smerieri, A., Akrout, A., Haelterman, M., Massar, S.: Fully analogue photonic reservoir computer. Sci. Rep. **6**(1), 1–8 (2016)

Goune Chengui, G.R., Woafo, P., Chembo, Y.K.: The simplest laser-based optoelectronic oscillator: an experimental and theoretical study. J. Lightw. Technol. 0733–8724 (2015)

Goune Chengui, G.R., Talla Mbé, J.H., Talla, A.F., Woafo, P., Chembo, Y.K.: Dynamics of optoelectronic oscillators with electronic and laser nonlinearities. IEEE J. Quantum Electron. **54**(1), 1–7 (2018)

Ha, M., Chembo, Y.K.: Nonlinear dynamics of continuously tunable optoelectronic oscillators based on stimulated Brillouin amplification. Opt. Express **29**(10), 14630–14648 (2021)

Hao, T., Liu, Y., Tang, J., Cen, Q., Li, W., Zhu, N., Dai, Y., Capmany, J., Yao, J., Li, M.: Recent advances in optoelectronic oscillators. Adv. Photon. **2**(4), 044001 (2020)

Huack, T., Scheinder, F.W.: Mixed-mode and quasiperiodic oscillations in the peroxidase reaction. J. Chem. Phys. **97**, 391 (1993)

Huang, L., Deng, L., Fu, S., Tang, M., Cheng, M., Zhang, M., Liu, D.: Stable and compact dual-loop optoelectronic oscillator using self-polarization-stabilization technique and multicore fiber. J. Lightw. Technol. **36**(22), 5196–5202 (2018)

Jia, S., Yu, J., Wang, J., Wu, Q., Huang, G., Yang, E.: A novel optoelectronic oscillator based on wavelength multiplexing. J. Opt. Soc. Am. B. **13**(8), 1725–1735 (1996)

Jiang, X., Cheng, M., Luo, F., Deng, L., Fu, S., Ke, C., Zhang, M., Tang, M., Shum, P., Liu, D.: Electro-optic chaotic system based o the reverse-time chaos theory and a nonlinear hybrid feedback loop. Opt. Express **24**, 28804–28814 (2016)

Kamaha, J.S.D., Talla Mbé, J.H., Woafo, P.: Routes to chaos and characterization of limit-cycle oscillations in wideband time-delayed optoelectronic oscillators with nonlinear filters. J. Opt. Soc. Am. B., **37**(11), A75–A81 (2020)

Kim, J.M., Cho, D.: Optoelectronic oscillator stabilized to an intraloop Fabry–Perot cavity by a dual servo system. Opt. Express **18**(14), 14905–14912 (2010)

Kouayep, R.B., Talla, A.F., Talla Mbé, J.H., Woafo, P.: Bursting oscillations in Colpitts oscillator and application in otoelectronics for the generation of complex optical signals. Opt. Quantum Electron. **52**, 1–13 (2020)

Larger, L., Baylon-Fuentes, A., Martinenghi, R., Udaltsov, V.S., Chembo, Y.K., Jacquot, M.: High-speed photonic reservoir computing using a time-delay-base architecture: million words per second classification. Phys. Rev. X **7**, 011015 (2017)

Lelievre, O., Crozatier, V., Berger, P., Baili, G., Liopis, O., Dolfi, D., Nouchi, P., Goldfard, F., Bretenaker, F., Morvan, L., Pillet, G.: A model designing ultralow noise single-and dual-loop 10-GHz optoelectronique oscillators. J. Lightw. Technol. **35**(20), 4366–4374 (2017)

Li, W., Yao, J.: An optically tunable optoelectronic oscillator. J. Lightw. Technol. **28**(18), 2640–2645 (2010)

Ly, A., Auroux, V., Khayatzadeh, R., Gutierrez, N., Fernandez, A., Llopis, O.: Highly spectrally pure 90 GHz signal synthesis using a coupled optoelectronic oscillator. IEEE Photon. Technol. Lett. **30**(14), 1313–1316 (2018)

Maleki, L.: The optoelectronic oscillator. Nat. Photon **5**(12), 728–730 (2011)

Martinez-Llinas, J., Colet, P., Erneux, T.: Tuning the period of square-wave oscillations for delay-coupled optoelectronic systems. Phys. Rev. E Stat. Phys. Plasmas Fluids Relat. Interdiscip. Top. **89**, 042908 (2014)

Munnelly, P., Lingnau, B., Karow, M.M., Heindel, T., Kamp, M., Hofling, S., Ludge, K., Schneider, C., Reitzenstein, S.: On-chip optoelectronic feedback in a micropillar laser-detector assembly. Optica **4**(3), 303–306 (2017)

Murphy, T.E., Cohen, A.B., Ravoori, B., Schmitt, K.R., Setty, A.V., Sorrentino, F., Williams, C.R., Ott, E., Roy, R.: Complex dynamics and synchronization of delayed-feedback nonlinear oscillators. Philos. Trans. R. Soc. A Math. Phys. Eng. Sci. **368**, 343–366 (2010)

Neyer, A., Vogues, E.: Dynamics of electroopic bistable devices with delayed feedback. IEEE J. Quantum Electron. **104**(12), 2009–2015 (1982)

Nguewou-Hyousse, H., Chembo, Y.K.: Nonlinear dynamics of miniature optoelectronic oscillators based on whispering-gallery mode electrooptical modulators. Opt. Express **28**(21), 30656–30674 (2020)

Nguewou-Hyousse, H., Chembo, Y.K.: Stochastic analysis of miniature optoelectronic oscillators based on whispering-gallery mode electrooptical modulators. IEEE Photon. J. **13**(3), 3000110 (2021)

Nguimdo, R.M., Chembo, Y.K., Colet, P., Larger, L.: On the phase noise performance of nonlinear double-loop optoelectronic microwave oscillators. IEEE J. Quantum Electron. **48**(11), 1415–1423 (2012)

Nguimdo, R.M., Chembo, Y.K., Colet, P., Larger, L.: On the phase noise performance of nonlinear double-loop optoelectronic microwave oscillators. IEEE J. Quantum Electron. **48**(11), 1415–21423 (2012)

Nguimdo, R.M., Lavrov, R., Colet, P., Jacquot, M., Chembo, Y.K., Larger, L.: Effects of fiber dispertion on broadband chaos communication implemented by electro optic nonlinear delay phase dynamics. J. Lightw. Technol. **28**(18), 2688–2689 (2010)

Okasuga, O., Adles, E.J., Levy, E.C., Zhou, W., Carter, G.M., Menyuk, C.R., Hrowitz, M.: Spurious mode reduction in dual injection-locked opotoelectronic oscillators. Opt. Exp. **19**(7), 5839–5854 (2011)

Ozdur, I., Akbulut, M., Hoghooghi, N., Mandridis, D., Piracha, M.U., Delfyett, P.J.: Optoelectronic loop design with 1000 finesse Fabry–Perot etalon. IEEE Photon. Technol. Lett. **27**(2), 213–216 (2014)

Paquot, Y., Dupont, F., Smerieri, A., Dambre, J., Schrauwen, B., Haelterman, M., Massar, S.: Optoelectronic reservoir computing. Sci. Rep. **2**, 287 (2012)

Petrov, V., Scott, S.K., Showalter, K.: Mixed-mode oscillations in chemical systems. J. Chem. Phys. **97**(9), 6191–6198 (1992)

Qin, B.W., Chung, K.W., Algaba, A.: High-order study of the canard explosion in an aircraft ground dynamics model. Nonlinear Dyn. **100**, 1079–1090 (2020)

Qin, B.W., Kwok-Wai, C., Algaba, A., Rodríguez-Luis, A.J.: High-order analysis of canard explosion in Brusselator equations. Int. J. Bifurcation Chaos **30**(05), 2050078 (2020)

Qin, B.W., Kwok-Wai, C., Algaba, A., Rodríguez-Luis, A.J.: Asymptotic expansions for a degenerate canard explosion. Physica D Nonlinear Phenomena **418**, 132841 (2021)

Romeira, B., Javaloyes, J., Figueiredo, J.M.L., Ironside, C.N., Cantu, H.I., Kelly, A.E.: Delayed feedback dynamics of Liénard-type resonant tunneling-photo-detector optoelectronic oscillators. IEEE J. Quantum Electron. **49**(1), 31–42 (2013)

Saleh, K., Lin, G. Chembo, Y.K.: Effect of laser coupling and active stabilization on the phase noise performance of optoelectronic microwave oscillator based on whispering-gallery mode-oscillator resonators. IEEE photon. J. **7**(1), Art.(5500111) (2015)

Sekikawa, M., Inaba, N., Yoshinaga, T., Hikihara, T.: Period-doubling cascades of canards from the extended Bonhoeffer–Van der Pol oscillator. Phys. Lett. A **374**, 3745 (2010)

Shchepakina, E., Korotkova, O.: Canard explosion in chemical and optical systems. Discrete Continuous Dyn. Syst. **18**, 495–5512 (2013)

Shi, M., Yi, L., Wei, W., Hu, W.: Generation and phase noise analysis of a wide optoelectronic oscillator with ultra-high resolution based on stimulated Brillouin scattering. Opt. Express **5**(13), 16113–16124 (2018)

Soriano, M.C., Ortin, S., Larger, L., Mirasso, C.R., Fischer, I., Pesquera, L.: Optoelectronic reservoir computing: tackling noise-induced performance degradation. Opt. Express **21**(1), 12–20 (2013)

Talla Mbé, J.H., Atchoffo, N.W., Tchitnga, R., Woafo, P.: Dynamics of time-delayed optoelectronic oscillators with nonlinear amplifiers and its potential application to random numbers generation. IEEE J. Quantum Electron. **57**(5), 5000507 (2021)

Talla Mbé, J.H., Woafo, P., Fotsin, H.B.: Experimental direct modulation of a laser diode with a van der pol circuit and applications. Opt. Eng. **58**(6), 066114 (2019)

Talla, A.F., Marteninghi, R., Woafo, P., Chembo, Y.K.: Breather and pulse-package dynamics in multi-nonlinear electro-optical systems with delay feedback. IEEE Photon. J. **8**(4), 1–8 (2016)

Talla, A.F., Martinenghi, R., Talla. Mbé, J.H., Saleh, K., Lin, G., Chengui, G.R.G., Coillet, A., Woafo, P. Chembo, Y.K.: Analysis of phase locking in narrow-band optoelectronic oscillators with intermediate frequency. J. Quantum Electron. **51**(6), 1–8 (2015)

Talla Mbé, J.H., Talla, A. F., Chengui, G.R.G., Coillet, A., Larger, L., Woafo, P., Chembo, Y.K.: Mixed-mode oscillations in slow–fast delayed optoelectronic systems. Phys. Rev. E **91**(012902) Art (2015)

Talla Mbé, J.H., Woafo, P., Chembo, Y.K.: A normal form method for the determination of oscillations characteristics near the primary Hopf bifurcation in bandpass optoelectronic oscillators: Theory and experiment. Chaos, **29**(033104) Art (2019)

Talla Mbé, J.H., Woafo, P.: Modulation of distributed feedback (DBF) laser diode with an autonomous Chua's circuit: Theory and experiment. Opt. Laser Technol. **100**, 145–152 (2018)

Talla Mbé, J.H., Kamaha, J.S.D., Woafo, P., Chembo, Y.K. (2019) Dynamics of wideband time-delayed optoelectronic oscillators with nonlinear filters. IEEE J. Quantum Electron. **55**(4), 5000106 (2019)

Tang, S., Liu, J.M.: Chaotic pulsing and quasi-periodic route to chaos in a semiconductor laser with delayed opto-electronic feedback. IEEE J. Quantum Electron. **37**(3), 329–336 (2001)

Tang, S., Liu, J.M.: Chaos synchronization in semiconductor lasers with optoelectronic feedback. IEEE J. Quantum Electron. **39**(6), 708–715 (2003)

Uchida, A.: Optical communication with chaotic lasers: applications of nonlinear dynamics and synchronization. Wiley, New York (2012)

Vo, T., Bertram, R., Tabak, J., Wechselberger, M.: Mixed mode oscillations as a mechanism for pseudo-plateau bursting. J. Comput. Neurosci. **28**, 443 (2010)

Wang, S., Fang, N., Wang, L.: Signal recovery based on optoelectronic reservoir computing for high speed optical fiber communication system. Opt. Commun. **495**(15), 127082 (2021)

Weicker, L., Erneux, T.: Slow–fast dynamics of time-delayed electro-optic oscillator. Philos. Trans. Roy. Soc. A Math. Phys **371**(1999), 20120459 (2013)

Weicker, L., Erneux, T., Jacquot, M., Chembo, Y., Larger, L.: Crenelated fast oscillatory outputs of tow-delay electro-optic oscillator. Phys. Rev. E Stat Phys. Plasmas Fluids Relat. Top **85**, 026206 (2012)

Williams, C.R.S., Murphy, T.E., Roy, R., Sorrentino, F., Dahms, T., Scholl, E.: Experimental observations of group synchrony in a system of chaotic optoelectronic oscillators. Phys. Rev. Lett. **110**, 064104 (2013)

Wu, B., et al.: Magnetic field sensor based on dual- frequency optoelectronic oscillators using cascaded magnetostrictive alloy-fiber Bragg grating-Fabry Perot and fiber Bragg grating-Fabry Perot filters. Opt. Express **26**(21), 27628–27638 (2018)

Yang, J., Jin-Long, Y., Yao-Tian, W., Li-Tai, Z., En-Ze, Y.: An optical domain combined dual-loop optoelectronic oscillator. IEEE Photon. Technol. Lett. **19**(11), 807–809 (2007)

Yao, J.: Optoelectronic oscillator for high speed and high resolution optical sensing. J. lightw. Technol. **35**(16), 3489–3497 (2017)

Yao, X.S., Maleki: High frequency optical subcarrier generator. Electron. Lett. **19**(11), 1525–1526 (1994)

Yao, X.S., Maleki: Optoelectronic microwave oscillator. J. Opt. Soc. Am. B. **13**(8), 1725–1735 (1996)

Zhang, Y., Hou, D., Zhao, J.: Long-term frequency stabilization of an optoelectronic oscillator using phase-locked loop. J. Lightw. Technol. **32**(13), 2408–2414 (2014)

Zhou, P., Pan, S., Zhu, D., Guo, R., Zhang, F., Zhao, Y.: A compact optoelectronic oscillator based on an electroabsorption modulated laser. IEEE Photon. Technol. Lett. **26**(1), 86–88 (2014)

Zou, X., Xinkai, L., Li, W., Li, P.: Optoelectronic oscillators (OEOs) to sensing, measurement, and detection. IEEE J. Quantum Electron. **52**(1), 0601116 (2016)

Zou, F., Zou, L., Yang, B., Ma, Q., Zou, X., Zou, J., Chen, S., Milosevic, D., Cao, Z., Liu, H.: Optoelectronic oscillator for 5G wireless networks and beyond. J. Phys. D Appl. Phys. (2021). https://doi.org/10.1088/1361-6463/ac13f2

Research Article Vol. 37, No. 11 / November 2020 / Journal of the Optical Society of America B A75

Journal of the Optical Society of America B

OPTICAL PHYSICS

Routes to chaos and characterization of limit-cycle oscillations in wideband time-delayed optoelectronic oscillators with nonlinear filters

JULIETTE STEVIA DEUMI KAMAHA,[1] JIMMI HERVE TALLA MBÉ,[1,2,*] AND PAUL WOAFO[1]

[1]Laboratory of Modelling and Simulation in Engineering, Biomimetics and Prototypes, University of Yaoundé I, Department of Physics, P. O. Box 812, Yaoundé, Cameroon
[2]Laboratory of Condensed Matter, Electronics and Signal Processing, Department of Physics, University of Dschang, P. O. Box 67, Dschang, Cameroon
*Corresponding author: jhtallam@yahoo.fr

Received 30 April 2020; revised 13 June 2020; accepted 20 June 2020; posted 22 June 2020 (Doc. ID 396596); published 28 July 2020

In this paper, we show that the cubic nonlinear optoelectronic oscillator (CN-OEO) [IEEE J. Quantum Electron. 55, 5000106-1 (2019)] depicts the phenomena of amplitude jump and crenelated oscillations in its routes to chaos. The amplitude jump is characterized by a sudden variation of the frequency of the limit-cycle oscillations. Using the normal form of the system, we characterize the limit-cycle oscillations. The amplitude and the frequency of these limit-cycle oscillations are determined mathematically and analyzed in terms of system parameters such as the time delay and feedback gain. It is analytically confirmed that the CN-OEO displays limit-cycle oscillations whose frequencies remain greater than those of a standard optoelectronic oscillator (the one with a standard bandpass filter in the electrical path). Our experimental measurements are in good agreement with the analytical and numerical results.

https://doi.org/10.1364/JOSAB.396596

1. INTRODUCTION

Optoelectronic oscillators (OEOs) are time-delayed autonomous nonlinear hybrid oscillators made of an optical and electrical path [1–3]. Fundamentally, they have been widely studied [4–9] and have also inspired numerous applications in areas such as chaos communications [10–14], ultrastable microwave generation [15–20], neuromorphic computing [21–24], and measurement, sensing, and detections [25–29]. A comprehensive review of applications of these time-delayed oscillators was recently reported in [30]. To achieve some of these applications, novel architectures are required.

Some of these architectures are made by incorporating an electronic self-sustained oscillator such as a Van der Pol or Colpitts in the feedback loop to investigate complex dynamics like antimonotonicity and some bursting-like oscillations not encountered in the standard OEO [9,31,32]. Sometimes, however, the resulting OEO missed mathematical modeling due to the incorporation of such oscillators in the OEO loop [31,32]. Recently, a cubic nonlinear optoelectronic oscillator (CN-OEO) was proposed [33]. It is an OEO where the electrical path features a cubic nonlinear response, implemented using a nonlinear capacitor. The circuit implementation of the cubic nonlinear filter used to build the CN-OEO (as well as the mathematical modeling) is simple compared to those of the Van der Pol and Colpitts oscillators. Besides, the dynamics that emerged show that the CN-OEO is more versatile than the standard OEO since it offers the possibility to display breathers or not by tuning some parameters of the system. In the case where breathers are controlled, they are replaced by limit-cycle oscillations of higher frequency.

This present work addresses a deeper dynamical characterization of that CN-OEO in terms of key parameters such as the strength of the feedback gain, the time delay, the offset phase, and the cubic nonlinear term. For instance, we prove that the transition to chaos is through successive amplitude jump phenomena and crenelated oscillations. In addition, the dynamics of the system is dominated by the limit-cycle oscillations. These latter are also characterized using the normal form method of this time-delayed system as it was recently done for a standard OEO [34]. The normal form permits the derivation of the analytical expressions of the amplitude and the frequency.

This paper has five sections: Section 2 presents the system; Section 3 presents a bifurcation analysis of the CN-OEO; and Section 4 presents the normal form analysis that helps to study the properties of the system (amplitude, frequency). The paper ends with a conclusion in Section 5.

2. THE SYSTEM AND MODEL

The experimental setup of the CN-OEO is presented in Fig. 1 [33]. A polarized light of power P_{in} delivered by a telecommunications continuous-wave laser diode (with a wavelength equal $\lambda_L \simeq 1.55\,\mu\text{m}$) is modulated with a Mach–Zehnder modulator (MZM) whose half-wave voltages are $V_{\pi\text{RF}} = 3.8\,\text{V}$ and $V_{\pi\text{DC}} = 5\,\text{V}$. The modulated light is retarded by an optical delay line resulting in a time-delay equal to $T_D = 3.28\,\mu\text{s}$, before being converted to an electrical signal with a photodiode (PD) of responsivity $S = 4.75\,\text{V/mW}$. The electrical signal generated by the photodiode V_{in} passes through a cubic nonlinear bandpass filter (CNBPF) that outputs V_{out} and in turn is subjected to an amplification before being re-injected into the RF electrode of the MZM. It can be noticed that the CNBPF is made of a resistor R, a coil L, and a nonlinear capacitor NC. It is constructed with an operational amplifier U (type LF356), two capacitors $C_{1,2}$, one resistor r, and a mixed assembly of eight simple junction diodes (type IN400X) and whose characteristics are the thermal voltage $V_T = 25\,\text{mV}$ and an inverse saturation current $I_s = 5\,\mu\text{A}$ [Fig. 1(b)]. A picture of the whole experimental setup in the laboratory is displayed in Fig. 2.

Combining both Kirchhoff's laws and the general modeling of the wideband OEO, the whole system of Fig. 1 is ruled by the following integro-differential delayed equation [33]:

$$x + \tau\frac{dx}{dt'} + \frac{1}{\theta}\int_0^{t'} x(s)\mathrm{d}s + \frac{\eta}{\tau^3}\left(\int_0^{t'} x(s)\mathrm{d}s\right)^3 = \beta\cos^2[x(t'-T_D)+\phi], \tag{1}$$

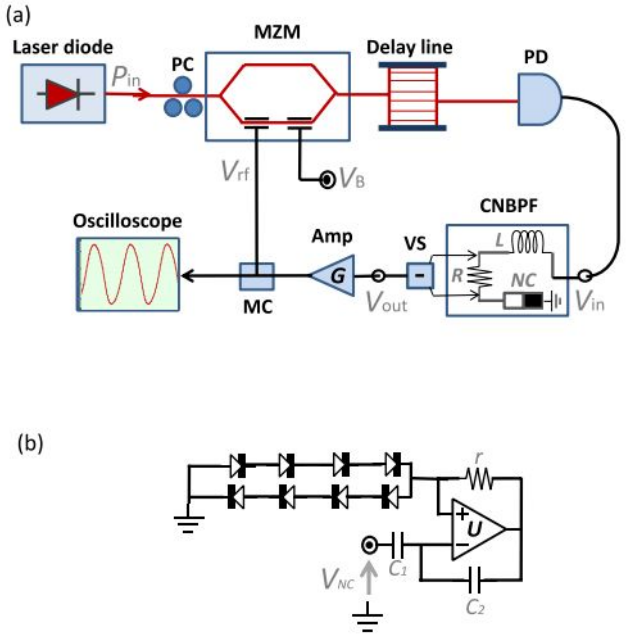

Fig. 1. (a) Experimental setup of cubic nonlinear optoelectronic oscillator [33]. (b) Inner structure of the nonlinear capacitor [35,36]. PC: polarization controller; MZM: Mach–Zehnder modulator; V_B is the offset phase control voltage; PD: photodiode; CNBPF: cubic nonlinear bandpass filter; VS: voltage subtractor; Amp: RF amplifier; MC: microwave coupler. $L = 0.1\,\text{mH}$, $r = 300\,\Omega$, $C_1 = 270\,\text{pF}$, and $C_2 = 9.15\,\text{nF}$.

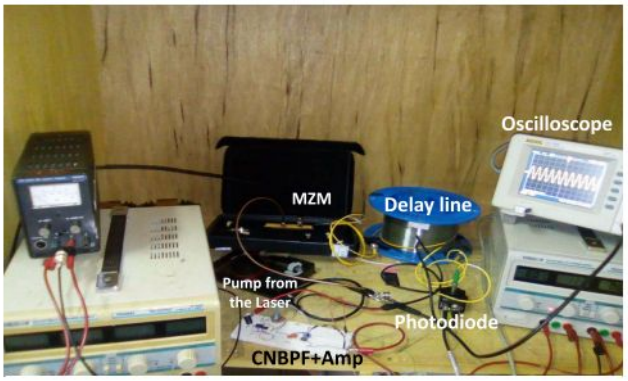

Fig. 2. Experimental device in the laboratory. One can identify the different components cited in the text. MZM: Mach–Zehnder modulator; CNBPF: cubic nonlinear bandpass filter; Amp: RF amplifier.

where $x = \frac{\pi V_{\text{out}}(t')}{2V_{\pi\text{RF}}}$ is the dimensionless dynamical variable of the system and t' is the time. $\theta = R[(\frac{1}{C_1}) - (\frac{nV_T}{2rI_sC_2})]^{-1}$ and $\tau = \frac{L}{R}$ are the high and low cutoff times, respectively. The additional timescale induced by the CNBPF is $\tau\sqrt[3]{1/\eta}$, with $\eta = \frac{nV_TV^2\pi\text{RF}}{[12(rRI_sC_2)^3(\pi G)^2]}\tau^3$ being the cubic nonlinear coefficient. $n = 4$ is the number of junction diodes in series. Other parameters are the normalized feedback gain $\beta = \frac{\pi\text{SGP}_{\text{in}}}{2V_{\pi\text{RF}}}$ and the offset phase $\phi = \pi V_B/2V_{\pi\text{DC}}$. Considering the following rescaling $\nu = \frac{T_D}{\tau}$, $x(t-\nu) = x_\nu$, $y = \frac{1}{\tau}\int_0^t x(s)\mathrm{d}s$, and $\epsilon = \frac{\tau}{\theta}$, Eq. (1) can be rewritten in the form of the flow as follows:

$$\dot{x} = -x - \epsilon y - \eta y^3 + \beta\cos^2[x_\nu + \phi], \tag{2}$$

$$\dot{y} = x, \tag{3}$$

where the "overdot" stands for the derivation according to the dimensionless time $t = \frac{t'}{\tau}$. In our previous work, it was shown that the fixed point $(x_{\text{st}}, y_{\text{st}})$ of the system is such that [33]

$$x_{\text{st}} = 0, \tag{4}$$

$$y_{\text{st}}^3 + \frac{\epsilon}{\eta}y_{\text{st}} = \frac{\beta}{\eta}\cos^2\phi. \tag{5}$$

The stability analysis of the fixed point shows that limit-cycle oscillation of frequency ω_H might occur through a Hopf bifurcation at γ_H [with $\gamma = \beta\sin(2\phi)$ being the effective feedback gain and $\gamma_H = \beta_H\sin(2\phi)$ its value at the Hopf bifurcation point] if and only if ω_H and γ_H fulfill the following transcendental equations:

$$1 + \gamma_H\cos\omega_H\nu = 0, \tag{6}$$

$$-\omega_H^2 + (\epsilon + 3\eta y_{\text{st}}^2) + \gamma_H\omega_H\sin\omega_H\nu = 0. \tag{7}$$

After some mathematical investigations, Eqs. (6) and (7) can be approximated with a third-order precision as

$$\omega_H = \sqrt{\frac{3}{2}\left[\frac{-1+\sqrt{1+\frac{4}{3}\nu(\epsilon+3\eta y_{\text{st}}^2)}}{\nu^2}\right]}, \tag{8}$$

$$\gamma_H = -1 - \frac{\omega_H^2 \nu^2}{2} + \frac{\omega_H^4 \nu^4}{24}. \quad (9)$$

This Hopf bifurcation point marks the beginning of oscillations in the system that evolve until the chaotic dynamics as it is developed in the next section (Section 3).

3. ROUTE TO CHAOS

The bifurcation diagrams of Figs. 3(a) and 3(b) effectively unveil a Hopf bifurcation at $|\gamma| \simeq 1$, as predicted by Eq. (9). The limit-cycle oscillation dominates until $|\gamma|$ is close to 2.57 [Figs. 4(a) and 4(d)]. Just above 2.57, chaos arises in the system,

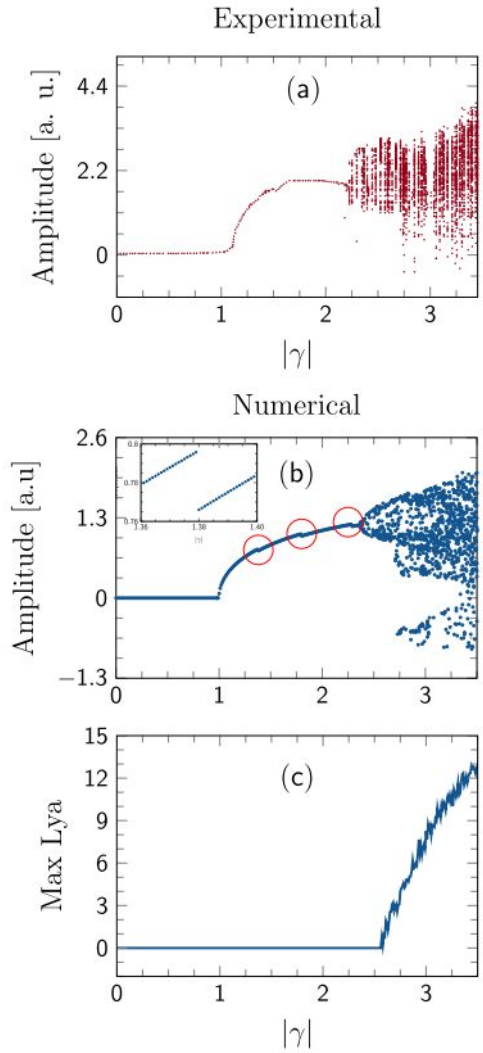

Fig. 3. (a) Point-by-point record of the experimental bifurcation diagram. The variation of γ is achieved by tuning the pump power P_{in} of the laser diode. (b) Numerical bifurcation diagram. It is important to mention that the "Amplitude" appearing in the vertical axis of (a) and (b) refers to the maximum peaks in a given time trace. (c) Corresponding maximum Lyapunov exponent. One can note the considerable agreement between the experimental and numerical curves. For an ameliorate matching, however, the exact contribution of each component of Fig. 1 in terms of attenuation/amplification and noise effects must be quantified. The value of η calculated using the experimental values of components is $\eta = 9.809 \times 10^{-5}$. $\phi = \frac{-\pi}{4}$.

as confirmed by the plot of the maximum Lyapunov exponent of Fig. 3(c), and which is defined as in [9,33]. A time trace of chaotic dynamics and the corresponding phase portrait are shown in Figs. 4(c) and 4(f). The transition from limit-cycle to chaos occurs exactly at $|\gamma| = 2.57$, and the system displays a crenelated oscillation [Figs. 4(b) and 4(e)]. This crenelated oscillation is similar to the one obtained by Weicker *et al.* with a standard OEO featuring a phase modulator in the nonlinear transfer function and two time delays in the feedback loop [37], and by Romeira *et al.* with an OEO comprising a phase modulator and a linearly chirped fiber Bragg grating [38]. The crenelated oscillation displays two types of dynamics: the slow dynamics characterized by square oscillations of the plateau and the fast dynamics representing the fast oscillations inside the plateau. It is also important to note that in the region of limit-cycle oscillations, the amplitude globally grows with the effective feedback gain. More precisely, it is a stepped bifurcation characterized by an amplitude jump phenomenon at some specific values of the effective feedback gain but not regularly spaced [$|\gamma| \simeq 1.379$, $|\gamma| \simeq 1.797$, and $|\gamma| \simeq 2.28$], as shown in the circled areas of Fig. 3(b).

The first region where the amplitude jump phenomenon occurs is highlighted in the inset of Fig. 3(b), which is the case for $|\gamma| \simeq 1.379$. As can be seen, around that region the amplitude first undergoes a progressive increase and suddenly decreases before starting to gradually increase again. On one side of the fall point, the periods of oscillations of the system for two neighboring values of $|\gamma|$ are very close. For instance, for two points taken before the fall point, we noticed that $T = 3.288 \times 10^{-7}$ s when $|\gamma| = 1.378$ and $T = 3.278 \times 10^{-7}$ s when $|\gamma| = 1.379$. After the jump, $T = 3 \times 10^{-7}$ s when $|\gamma| = 1.38$ and $T = 2.981 \times 10^{-7}$ s when $|\gamma| = 1.381$. One can immediately observe that the period globally decreases as the effective feedback gain increases. For very close values of the effective feedback gain, and at the neighborhood of the jump, there is an important variation of the period of oscillation compared to closer points at each size. Indeed, exactly at the fall point, when $\gamma = 1.379$, $T = 3.278 \times 10^{-7}$ s and when $|\gamma| = 1.38$, $T = 3 \times 10^{-7}$ s, the variation of the period in this interval gives $\Delta T = 2.78 \times 10^{-8}$ s for just a light change in the effective feedback gain equal to 0.001. Then, the amplitude drop is accompanied by a large variation of the period of limit-cycle oscillation. Moreover, this phenomenon unveils that two limit-cycle oscillations with the same amplitude can evolve with different periods. An example is the case of two limit-cycle oscillations (one obtained at $|\gamma| = 1.365$ and the other at $|\gamma| = 1.397$) which oscillate with the periods ($T = 3.27 \times 10^{-7}$ s and $T = 3.278 \times 10^{-7}$ s, respectively), but with same amplitude $x \simeq 0.782$. This behavior appears globally the same for other jump points apart from the fact that the variation of the periods are not the same; however, it gradually decreases as the effective feedback gain increases. Indeed, for the second and the third points of jump phenomenon $|\gamma| \simeq 1.797$ and $|\gamma| \simeq 2.28$, the variations are $\Delta T = 2.28 \times 10^{-8}$ s and $\Delta T = 1.98 \times 10^{-8}$ s, respectively.

From this bifurcation analysis, it is noticeable that two main dynamics are dominant in the CN-OEO: the limit cycle and chaos oscillations. The analytical analysis of chaos remains a great challenge; recently, however, it was demonstrated that the

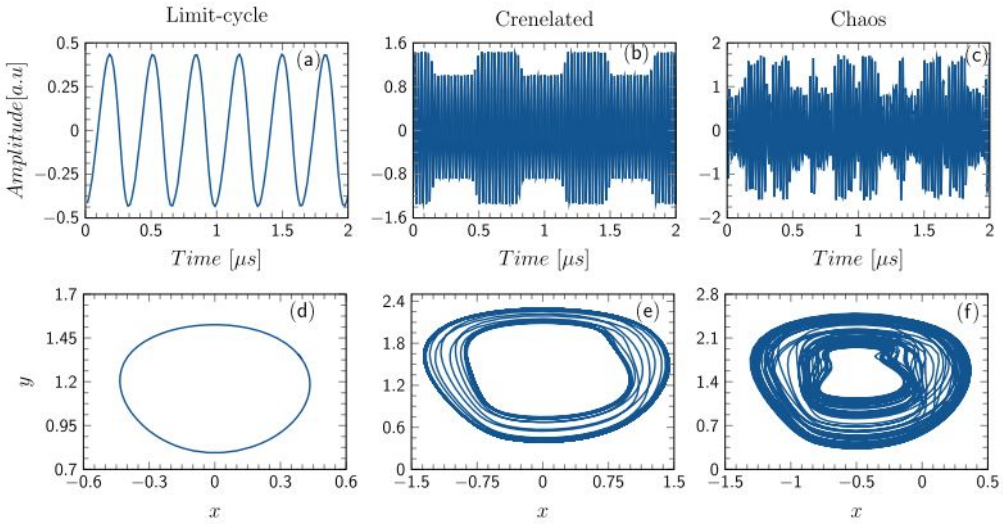

Fig. 4. Time traces and phase portraits of the system at different levels of the bifurcation diagram. (a) and (d) $|\gamma| = 1.1$; (b) and (e) $|\gamma| = 2.5$; and (c) and (f) $|\gamma| = 3.0$. $\eta = 9.809 \times 10^{-5}$ and $\phi = \frac{-\pi}{4}$.

limit cycle in inherent-infinite dimensional systems such as the standard OEO can be analytically characterized in terms of their amplitude and frequency using the method of the normal form [34]. In the next section, that method of the normal form will be applied to our CN-OEO (see Section 4).

4. CHARACTERIZATION OF LIMIT-CYCLE OSCILLATION

Several approaches have been proposed in the literature to compute the normal form of retarded systems including integral averaging, the Freehold alternative, the implicit function theorem, the multiple scales method, and the center manifold reduction [39]. In this paper, we chose the center manifold reduction method since it has been successfully used to characterize standard OEO [34] and other time-delayed systems [39–42]. It stipulates that the long-time dynamics of a system can be reduced to the dynamics on its center manifold. Also, it is a rigorous mathematical technique that makes this reduction possible, at least near the Hopf bifurcation point [43].

After performing several mathematical investigations with respect to the techniques and hypothesis regarding the theory of the center manifold reduction method, it can be proven that the complex normal form of Eqs. (2) and (3) is (see Appendix A)

$$\dot{z} = i\omega_H z - \delta \bar{b}\mu z - 3\eta \bar{b} z^2 \bar{z} + \bar{b}\gamma_H \mu^2 \bar{\mu} \times [2 - 4i\omega_H \gamma_H \alpha^2 \Gamma e^{-2i\omega_H \nu}] z^2 \bar{z}, \tag{10}$$

where $\delta = \gamma - \gamma_H$ is the relative effective feedback gain. The reader should consult Appendix A for expressions of other coefficients appearing in Eq. (10), notably b, μ, α, and Γ. The "overline" stands for the complex conjugation. In the first approximation, the variable z is related to the complex amplitude of limit-cycle oscillation by $z(t) = A(t)e^{i\omega_H t}$ which, replaced in Eq. (10) leads to the complex normal form of the amplitude,

$$\dot{A} = -\delta \Lambda_1 A + \Lambda_2 A^2 \bar{A}, \tag{11}$$

where the coefficients Λ_1 and Λ_2 have the expressions

$$\Lambda_1 = \frac{i\omega_H e^{-i\omega_H \nu}}{1 + 2i\omega_H + \gamma_H(1 - i\omega_H \nu)e^{-i\omega_H \nu}}, \tag{12}$$

$$\Lambda_2 = 2\gamma_H \omega_H^2 \Lambda_1 [1 - 2i\omega_H \gamma_H \alpha^2 \Gamma e^{-2i\omega_H \nu}] - 3\eta \Lambda_1 / \mu. \tag{13}$$

It is remarkable that only Λ_2 explicitly depends on the cubic nonlinear coefficient η. Equation (11) is a complex equation whose solution can be approximated in the form of $A = a(t)e^{i\varphi(t)}$ that will allow us to study the evolution of the amplitude and the frequency around the Hopf bifurcation point. Replacing A in Eq. (11) yields

$$\dot{a} = -\delta \Lambda_{1r} a + \Lambda_{2r} a^3, \tag{14}$$

$$\dot{\varphi} = -\delta \Lambda_{1i} + \Lambda_{2i} a^2, \tag{15}$$

with Λ_{1r} and Λ_{1i} being the real and the imaginary parts of Λ_1, respectively. Similarly, Λ_{2r} and Λ_{2i} also are the real and the imaginary parts of Λ_2, respectively.

The equilibrium points of Eq. (14) are

$$a_{st_0} = 0, \tag{16}$$

$$a_{st_1} = \sqrt{\frac{\delta \Lambda_{1r}}{\Lambda_{2r}}}, \tag{17}$$

$$a_{st_2} = -\sqrt{\frac{\delta \Lambda_{1r}}{\Lambda_{2r}}}, \tag{18}$$

which are defined if and only if $\Lambda_{2r} \neq 0$ and $\frac{\delta \Lambda_{1r}}{\Lambda_{2r}} > 0$. The stability condition of the trivial (a_{st_0}) and the nontrivial ($a_{st_{1,2}}$) states depends on the sign of the multiplicities,

$$\lambda_{st_0} = -\delta \Lambda_{1r}, \tag{19}$$

and

$$\lambda_{st_{1,2}} = 2\delta\Lambda_{1r}, \tag{20}$$

respectively. According to Eq. (15), the dynamics of the phase is directly related to the one of the amplitude. The phase is defined for amplitudes different from zero. Indeed, for $a = a_{st0} = 0$, $A(t) = 0$ and $z(t) = 0$. There are no oscillations in the system. For $a = a_{st_{1,2}}$, the solution of Eq. (15) yields

$$\varphi = \delta k t + \varphi_0, \tag{21}$$

where φ_0 is the reference phase that is arbitrarily set to zero if needed and $k = (\Lambda_{1r}\Lambda_{2i} - \Lambda_{1i}\Lambda_{2r})/\Lambda_{2r}$ being a coefficient. The stability of the phase is satisfied if $k = 0$, which corresponds to $\Lambda_{1r}\Lambda_{2i} = \Lambda_{1i}\Lambda_{2r}$.

Beyond the Hopf bifurcation point, the system undergoes the limit-cycle oscillations. From what precedes, it can be demonstrated that the amplitude and the frequency of such limit-cycle oscillations can be explicitly defined as a function of the relative effective feedback gain $\delta \equiv \gamma - \gamma_H$ following

$$a = 2\omega_H\sqrt{(\gamma - \gamma_H)\frac{\Lambda_{1r}}{\Lambda_{2r}}}, \tag{22}$$

$$\omega_{\text{eff}} = \omega_H + (\gamma - \gamma_H)\frac{\Lambda_{1r}\Lambda_{2i} - \Lambda_{1i}\Lambda_{2r}}{\Lambda_{2r}}. \tag{23}$$

Hence, the cubic nonlinear coefficient affects both the amplitude and the frequency [see Eq. (13)]. Figure (5) shows the variation of the amplitude when the gain is increased beyond the Hopf bifurcation point. Besides, Fig. (6) shows the variations of the effective frequency of oscillation as a function of the normalized time delay. Qualitatively, the variation in both figures is similar to those observed with the standard OEO [34]. The amplitude scales as $\sqrt{|\delta|}$ beyond the Hopf bifurcation point with the proportionality factor equal to $2\omega_H\sqrt{\frac{\Lambda_{1r}}{\Lambda_{2r}}}$ and is a function of all the time constants of the oscillator, including the cubic nonlinear coefficient. However, the frequency asymptotically decreases with the time delay. Furthermore, Fig. (6) depicts that for the same value of a time delay, and the CN-OEO evolves with limit-cycle oscillations whose frequencies are higher compared to those of the standard OEO. These results are consistent with the prediction of [33].

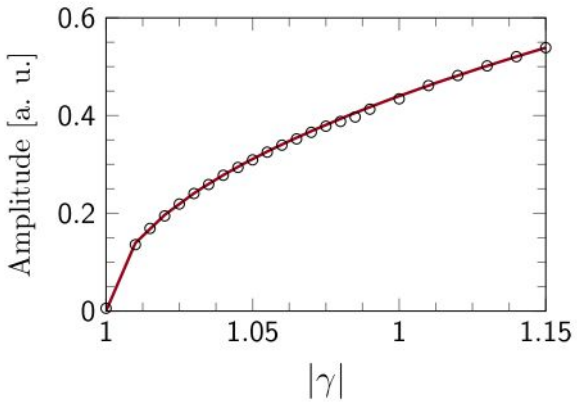

Fig. 5. Variation of the amplitude versus the effective feedback gain $|\gamma|$. The analytical curve (solid line) is obtained from Eq. (22), while the numerical curve (black circles) is plotted using Eqs. (2) and (3). $\phi = -\frac{\pi}{4}$ and $\eta = 1.49 \times 10^{-4}$.

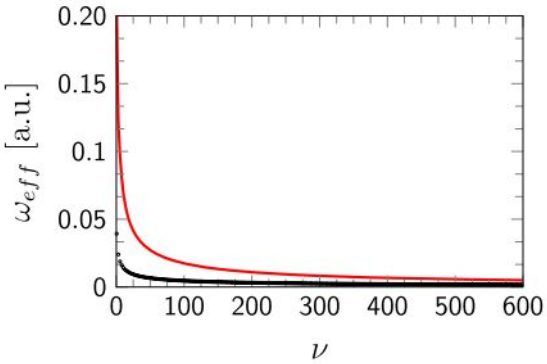

Fig. 6. Evolution of the effective frequency as a function of the normalized time delay ν. For the solid line (upper curve), $\eta = 1.49 \times 10^{-4} \neq 0$; for the dotted line (bottom curve), $\eta = 0$. $\phi = -\frac{\pi}{4}$ and $\delta = -0.02$.

5. CONCLUSION

In conclusion, we have investigated the bifurcation scenario of a CN-OEO and analyzed the characteristics of the limit-cycle oscillations in terms of some parameters of the system such as the time delay, the strength of the feedback gain, and the cubic nonlinear coefficient. As the bifurcation is concerned, the dynamics of the CN-OEO is essentially dominated by the limit-cycle oscillation and chaos. The transition between them is through crenelated oscillation. Like other slow–fast dynamics such as bursting, breathers, and spikes, these crenelated-oscillations might find applications in biology, bioengineering of artificial organs, and neuromorphic computing as suggested in [31,38,44,45]. Moreover, the limit-cycle oscillations undergo small amplitude jumps that are observed at specific points during the progression of the system toward chaos. These amplitude jumps are characterized by a sudden decrease in the period of oscillation. The characterization of the limit-cycle oscillation by the use of the normal form reduction has permitted the derivation of the analytical expressions of both their amplitude and frequency. We have demonstrated that they evolve similarly to a standard OEO. The amplitude grows with the effective feedback gain, while the frequency decreases with the normalized time delay. However, the standard OEO evolves with a lower frequency of oscillation at the primary Hopf bifurcation compared to the CN-OEO even in the asymptotic case of large delays ($\nu > 500$). It can be envisaged to apply the technique of the normal form reduction to crenelated oscillation as a second bifurcation. Our future works will deal with the application of this work to other simple architectures of OEO and the synchronization of several CN-OEOs.

APPENDIX A

We present the steps of the calculation of the normal form of the CN-OEO [see Eq. (10)] through the center manifold reduction method. The technique has been inspired from [39–42] and the

steps of calculations that follow are based on the similar work carried out on the standard OEO [34].

Before the Hopf bifurcation point, the dynamics of the system is ruled by the trivial steady state of the variable $x_{st} = 0$, as shown in Fig. (3). Moreover, around that Hopf bifurcation point, the relative gain $\delta = \gamma - \gamma_H = (\beta - \beta_H)\sin 2\phi$ is considered as a small parameter ($\delta \ll 1$). Therefore, in the neighborhood of the Hopf bifurcation point, a Taylor expansion around x_{st} and δ can be carried out so that Eqs. (2) and (3) transform into a linear ($\mathcal{L}X + \mathcal{R}X_\nu$) and nonlinear ($\mathcal{F}(X_\nu)$) part as

$$\dot{X} = \mathcal{L}X + \mathcal{R}X_\nu + \mathcal{F}(X_\nu), \tag{A1}$$

with $X = \begin{pmatrix} x \\ y \end{pmatrix}$ being the vector matrix of the variable of the system.

$$\mathcal{L} = \begin{bmatrix} -1 & -\epsilon \\ 1 & 0 \end{bmatrix} \tag{A2}$$

and

$$\mathcal{R} = \begin{bmatrix} -\gamma_H & 0 \\ 0 & 0 \end{bmatrix} \tag{A3}$$

are the 2×2 matrices. $\mathcal{F}$ is a column vector defined as

$$\mathcal{F}(X_\nu) = \begin{pmatrix} -\delta x_\nu - \eta y^3 - \alpha\gamma_H x_\nu^2 + \frac{2}{3}\gamma_H x_\nu^3 \\ 0 \end{pmatrix}. \tag{A4}$$

In Eq. (A4), $\alpha = [\tan(2\phi)]^{-1}$. Since Eq. (A1) is a delay-differential equation, computing this equation requires consideration of the time intervals in the past ($[-\nu, 0]$) and after the time origin ($[0, +\infty[$). Let us refer to σ as the time within the interval $[-\nu, 0]$ and maintain the notation of time t within $[0, +\infty[$. Then, Eq. (A1) can be written as a step equation,

$$\frac{dX_{t(\sigma)}}{dt} = \mathcal{A}X_{t(\sigma)} + \mathcal{G}(X_{t(\sigma)}), \tag{A5}$$

where $X_{t(\sigma)} = X(t + \sigma)$ is a portion of the solution trajectory in the recent past, and $\mathcal{A}$ is the linear operator with pure imaginary eigenvalue $i\omega_H$ of the Hopf bifurcation point. $\mathcal{A}$ transforms a center subspace function $p(\sigma)$ as follows:

$$\mathcal{A}p(\sigma) = i\omega_H p(\sigma) = \begin{cases} \frac{dp(\sigma)}{d\sigma} & \text{for } -\nu \le \sigma \le 0 \\ \mathcal{L}p(0) + \mathcal{R}p(-\nu) & \text{for } \sigma = 0. \end{cases} \tag{A6}$$

It is known that when $i\omega_H$ is an eigenvalue of the Hopf bifurcation, its complex conjugate $-i\omega_H$ also is an eigenvalue. Thus, to consider both eigenvalues, we define the adjoint operator of $\mathcal{A}$, called $\mathcal{A}^*$, which also acts on another subspace function $q(\sigma)$ as

$$\mathcal{A}^* q(\sigma) = -i\omega_H q(\sigma) = \begin{cases} -\frac{dq(\sigma)}{d\sigma} & \text{for } 0 \le \sigma \le \nu \\ \mathcal{L}^* q(0) + \mathcal{R}^* q(\nu) & \text{for } \sigma = 0, \end{cases} \tag{A7}$$

where $\mathcal{L}^*$ and $\mathcal{R}^*$ are the adjoints of the operators $\mathcal{L}$ and $\mathcal{R}$, respectively. In Eq. (A5), the expression of the vector $\mathcal{G}$ is

$$\mathcal{G} = \begin{cases} 0 & \text{for } -\nu \le \sigma \le 0 \\ \mathcal{F} & \text{for } \sigma = 0. \end{cases} \tag{A8}$$

The center manifold reduction theory requires that the subspace functions $p(\sigma)$ and $q(\sigma)$ satisfy the inner product,

$$\langle q, p\rangle = \bar{q}(0)p(0) + \int_{-\nu}^{0} \bar{q}(\xi + \nu) R_H^* p(\xi) d\xi, \tag{A9}$$

where the "overline" stands for the complex conjugation. Since $X_t(\sigma)$ must be finite, it is necessary to introduce a normalization condition, such that $\langle q, p\rangle = 1$ and $\langle q, \bar{p}\rangle = 0$. These inner products lead to the solutions of Eqs. (A6) and (A7), respectively:

$$p(\sigma) = \begin{pmatrix} i\omega_H\sigma \\ 1 \end{pmatrix} e^{i\omega_H\sigma}, \tag{A10}$$

$$q(\sigma) = b \begin{pmatrix} 1 \\ -i\epsilon/\omega_H \end{pmatrix} e^{i\omega_H\sigma}, \tag{A11}$$

where b is a complex-valued parameter defined as

$$b = [1 - 2i\omega_H + \gamma_H(1 + i\omega_H\nu)e^{i\omega_H\sigma}]^{-1}. \tag{A12}$$

The next step is to use the center subspace to decompose the trajectory $X_t(\sigma)$ into two components: the first one $\mathfrak{y}(t)p(\sigma) + \bar{\mathfrak{y}}(t)\bar{p}(\sigma)$ lying on the center subspace; the second one $u_t(\sigma)$ transverse to that center subspace is the infinite-dimensional component and satisfies $\langle p, u\rangle = 0$ and $\langle \bar{p}, u\rangle = 0$; hence,

$$X_t(\sigma) = \mathfrak{y}(t)p(\sigma) + \bar{\mathfrak{y}}(t)\bar{p}(\sigma) + u_t(\sigma). \tag{A13}$$

Substituting this last equation into Eq. (A5) and using the inner products yield that $\mathfrak{y}(t)$ satisfies the following first-order differential equation:

$$\begin{aligned} \dot{\mathfrak{y}}(t) = {} & i\omega_H\mathfrak{y} - \delta\bar{b}\mu\mathfrak{y} - 3\eta b\mathfrak{y}^2\bar{\mathfrak{y}} - \bar{b}\gamma_H\alpha(\mu\mathfrak{y} + \bar{\mu}\bar{\mathfrak{y}})^2 \\ & - 2i\bar{b}(\gamma_H\alpha\mu)^2\bar{\mu}\left[\frac{\bar{b}}{\omega_H}\mu - 7\frac{b}{3\omega_H}\bar{\mu} + 2\omega_H\Gamma e^{-2i\omega_H\nu}\right]\mathfrak{y}^2\bar{\mathfrak{y}} \\ & + 2\bar{b}\gamma_H\mu^2\bar{\mu}\mathfrak{y}^2\bar{\mathfrak{y}} + \text{NRT}. \end{aligned} \tag{A14}$$

The term NRT represents the nonresonant terms of the equation and the "overdot" refers to the differentiation with respect to time. The complex coefficients μ and Γ are explicitly given by

$$\mu = i\omega_H e^{-i\omega_H\nu}, \tag{A15}$$

$$\Gamma = [4\omega_H^2 - \epsilon - 2i\omega_H(1 + \gamma_H e^{-2i\omega_H\nu})]^{-1}. \tag{A16}$$

Now introducing the near-identity transformation

$$\mathfrak{y}(t) = z + k_{11}z^2 + k_{12}z\bar{z} + k_{13}\bar{z}^2 \tag{A17}$$

into Eq. (A14) and eliminating the secular terms yields

$$k_{11} = \frac{i\bar{b}\gamma_H\alpha}{\omega}\mu^2, \tag{A18}$$

$$k_{12} = \frac{-2i\bar{b}\gamma_H\alpha}{\omega}\mu\bar{\mu}, \tag{A19}$$

$$k_{13} = \frac{-i\bar{b}\gamma_H\alpha}{3\omega}\bar{\mu}^2. \tag{A20}$$

The nonsecular terms that remain constitute the complex normal form of the system and are given by

$$\dot{z} = i\omega_H z - \delta\bar{b}\lambda z - 3\eta\bar{b}z^2\bar{z} + \bar{b}\gamma_H\mu^2\bar{\mu} \times [2 - 4i\omega_H\gamma_H\alpha^2\Gamma e^{-2i\omega_H\nu}]z^2\bar{z}. \tag{A21}$$

Acknowledgment. The authors thank Yanne K. Chembo for fruitful discussions.

Disclosures. The authors declare that there are no conflicts of interest related to this paper.

REFERENCES

1. X. S. Yao and L. Maleki, "Optoelectronic microwave oscillator," J. Opt. Soc. Am. B **13**, 1725–1735 (1996).
2. A. Neyer and E. Voges, "Dynamics of electrooptic bistable devices with delayed feedback," IEEE J. Quantum Electron. **18**, 2009–2015 (1982).
3. L. Maleki, "The optoelectronic oscillator," Nat. Photonics **5**, 728–730 (2011).
4. M. Peil, M. Jacquot, Y. K. Chembo, L. Larger, and T. Erneux, "Routes to chaos and multiple time scale dynamics in broadband bandpass nonlinear delay electro-optic oscillators," Phys. Rev. E **79**, 026208 (2009).
5. G. R. G. Chengui, A. F. Talla, J. H. Talla Mbé, A. Coillet, K. Saleh, L. Larger, P. Woafo, and Y. K. Chembo, "Theoretical and experimental study of slow-scale Hopf limit-cycles in laser-based wideband optoelectronic oscillators," J. Opt. Soc. Am. B **31**, 2310–2316 (2014).
6. J. H. Talla Mbé, A. F. Talla, G. R. G. Chengui, A. Coillet, L. Larger, P. Woafo, and Y. K. Chembo, "Mixed-mode oscillations in slow-fast delayed optoelectronic systems," Phys. Rev. E. **91**, 012902 (2015).
7. A. F. Talla, R. Martinenghi, G. R. G. Chengui, J. H. Talla Mbé, K. Saleh, A. Coillet, G. Lin, P. Woafo, and Y. K. Chembo, "Analysis of phase-locking in narrow-band optoelectronic oscillators with intermediate frequency," IEEE J. Quantum Electron. **51**, 5000108 (2015).
8. B. Romeira, J. Javaloyes, J. M. L. Figueiredo, C. N. Ironside, H. Cantu, I, and A. E. Kelly, "Delayed feedback dynamics of Liénard-type resonant tunneling-photo-detector optoelectronic oscillators," IEEE J. Quantum Electron. **49**, 31–42 (2013).
9. G. R. G. Chengui, J. H. Talla Mbé, A. F. Talla, P. Woafo, and Y. K. Chembo, "Dynamics of optoelectronic oscillators with electronic and laser nonlinearities," IEEE J. Quantum Electron. **54**, 5000207 (2018).
10. A. Argyris, D. Syvridis, L. Larger, V. Annovazzi-Lodi, P. Colet, I. Fischer, J. Garcia-Ojalvo, C. R. Mirasso, L. Pesquera, and K. A. Shore, "Chaos-based communications at high bit rates using commercial fibre-optic links," Nature **438**, 343–346 (2005).
11. J. Ai, L. Wang, and J. Wang, "Secure communications of CAP-4 and OOK signals over MMF based on electro-optic chaos," Opt. Lett. **42**, 3662–3665 (2017).
12. J. Oden, R. Lavrov, Y. K. Chembo, and L. Larger, "Multi-Gbit/s optical phase chaos communications using a time-delayed optoelectronic oscillator with a three-wave interferometer nonlinearity," Chaos **27**, 114311 (2017).
13. R. M. Nguimdo, R. Lavrov, P. Colet, M. Jacquot, Y. K. Chembo, and L. Larger, "Effect of fiber dispersion on broadband chaos communications implemented by electro-optic nonlinear delay phase dynamics," J. Lightwave Technol. **28**, 2688–2696 (2010).
14. Y. K. Chembo, "Laser-based optoelectronic generation of narrowband microwave chaos for radars and radio-communication scrambling," Opt. Lett. **42**, 3431–3434 (2017).
15. T. Hao, Q. Cen, Y. Dai, J. Tang, W. Li, J. Yao, N. Zhu, and M. Li, "Breaking the limitation of mode building time in an optoelectronic oscillator," Nat. Commun **9**, 1839 (2018).
16. I. Ozdur, M. Akbulut, N. Hoghooghi, D. Mandridis, M. U. Piracha, and P. J. Delfyett, "Optoelectronic loop design with 1000 finesse Fabry–Perot etalon," Opt. Lett. **35**, 799–801 (2010).
17. R. M. Nguimdo, Y. K. Chembo, P. Colet, and L. Larger, "On the phase noise performance of nonlinear double-loop optoelectronic microwave oscillators," IEEE J. Quantum Electron. **48**, 1415–1423 (2012).
18. S. Jia, J. Yu, J. Wang, W. Wang, and Q. Wu, "A novel optoelectronic oscillator based on wavelength multiplexing," IEEE Photon. Technol. Lett. **27**, 213–216 (2014).
19. K. Saleh, R. Henriet, S. Diallo, G. Lin, R. Martinenghi, I. V. Balakireva, P. Salzenstein, A. Coillet, and Y. K. Chembo, "Phase noise performance comparison between optoelectronic oscillators based on optical delay lines and whispering gallery mode resonators," Opt. Express **22**, 32158–32173 (2014).
20. J. Zhang and J. Yao, "Parity-time-symmetric optoelectronic oscillator," Sci. Adv. **4**, eaar6782 (2018).
21. L. Appeltant, M. C. Soriano, G. Van der Sande, J. Danckaert, S. Massar, J. Dambre, B. Schrauwen, C. R. Mirasso, and I. Fischer, "Information processing using a single dynamical node as complex system," Nat. Commun. **2**, 1–6 (2011).
22. D. Brunner, M. C. Soriano, C. R. Mirasso, and I. Fischer, "Parallel photonic information processing at gigabyte per second data rates using transient states," Nat. Commun. **4**, 1364 (2013).
23. F. Duport, A. Smerieri, A. Akrout, M. Haelterman, and S. Massar, "Fully analogue photonic reservoir computer," Sci. Rep. **6**, 22381 (2016).
24. L. Larger, A. Baylon-Fuentes, R. Martinenghi, V. S. Udaltsov, Y. K. Chembo, and M. Jacquot, "High-speed photonic reservoir computing using a time-delay-based architecture: million words per second classification," Phys. Rev. X **7**, 011015 (2017).
25. F. Kong, B. Romeira, J. Zhang, W. Li, and J. A. Yao, "A dual-wavelength fiber ring laser incorporating an injection-coupled optoelectronic oscillator and its application to transverse load sensing," IEEE J. Lightwave Technol. **32**, 1784–1793 (2014).
26. X. Zou, X. Liu, W. Li, P. Li, W. Pan, L. Yan, and L. Shao, "Optoelectronic oscillators (OEOs) to sensing, measurement, and detection," IEEE J. Quantum Electron. **52**, 0601116 (2016).
27. J. Yao, "Optoelectronic oscillators for high speed and high resolution optical sensing," IEEE J. Lightwave Technol. **35**, 3489–3497 (2017).
28. B. Wu, M. Wang, Y. Dong, Y. Tang, H. Mu, H. Li, B. Yin, F. Yan, and Z. Han, "Magnetic field sensor based on a dual-frequency optoelectronic oscillator using cascaded magnetostrictive alloy-fiber Bragg grating-Fabry Perot and fiber Bragg grating-Fabry Perot filters," Opt. Express **26**, 27628–27638 (2018).
29. Z. Zhu, M. Merklein, D.-Y. Choi, K. Vu, P. Ma, S. J. Madden, and B. J. Eggleton, "Highly sensitive, broadband microwave frequency identification using a chip-based Brillouin optoelectronic oscillator," Opt. Express **27**, 12855–12868 (2019).
30. Y. K. Chembo, D. Bunner, M. Jacquot, and L. Larger, "Optoelectronic oscillators with time-delayed feedback," Rev. Mod. Phys. **91**, 035006 (2019).
31. A. F. Talla, R. Martinenghi, P. Woafo, and Y. K. Chembo, "Breather and pulse-package dynamics in multinonlinear electrooptical systems with delayed feedback," IEEE Photon. J. **8**, 7803608 (2016).
32. R. M. Kouayep, A. F. Talla, J. H. Talla Mbé, and P. Woafo, "Bursting oscillations in Colpitts oscillator and application in optoelectronics for the generation of complex optical signals," Opt. Quantum Electron. **52**, 291 (2020).
33. J. H. Talla Mbé, J. S. D. Kamaha, P. Woafo, and Y. K. Chembo, "Dynamics of wideband time-delayed optoelectronic oscillators with nonlinear filters," IEEE J. Quantum Electron. **55**, 5000106 (2019).

34. J. H. Talla Mbé, P. Woafo, and Y. K. Chembo, "A normal form method for the determination of oscillations characteristics near the primary Hopf bifurcation in bandpass optoelectronic oscillators: theory and experiment," Chaos **29**, 033104 (2019).
35. H. Fatoorehchi, H. Abolghasemi, and R. Zarghami, "Analytical approximate solutions for a general nonlinear resistor-nonlinear capacitor circuit model," Appl. Math. Model. **39**, 6021–6031 (2015).
36. C. A. K. Kwuimy and P. Woafo, "Experimental realization and simulations a self-sustained macro electromechanical system," Mech. Res. Commun. **37**, 106–110 (2010).
37. L. Weicker, T. Erneux, M. Jacquot, Y. Chembo, and L. Larger, "Crenelated fast oscillatory outputs of a two delay electro-optic oscillator," Phys. Rev. E **85**, 026206 (2012).
38. B. Romeira, F. Kong, W. Li, J. M. L. Figueiredo, J. Javaloyes, and J. Yao, "Broadband chaotic signals and breather oscillations in an optoelectronic oscillator incorporating a microwave photonic filter," IEEE J. Lightwave Technol. **32**, 3933–3942 (2014).
39. A. H. Nayfeh, *The Method of Normal Forms* (Wiley, 2011).
40. Y. Tian and P. Yu, "An explicit recursive formula for computing the normal forms associated with semisimple cases," Commun. Nonlinear Sci. Numer. Simul. **19**, 2294–2308 (2014).
41. Y. Zheng and Z. Wang, "Delayed Hopf bifurcation in time-delayed slow-fast systems," Sci. China Technol. Sci. **53**, 656–663 (2010).
42. L. Illing and D. J. Gauthier, "Hopf bifurcations in time-delay systems with band-limited feedback," Physica D **210**, 180–202 (2005).
43. J. Carr and R. G. Muncaster, "The application of centre manifolds to amplitude expansions," J. Differ. Equ. **50**, 260–279 (1983).
44. E. M. Izhikevich, "Neural excitability, spiking and bursting," Int. J. Bif. Chaos **10**, 1171–1266 (2000).
45. J. Jerrelind and A. Stensson, "Nonlinear dynamics of parts in engineering systems," Chaos Solitons Fract. **11**, 2413–2428 (2000).

Dynamics of Wideband Time-Delayed Optoelectronic Oscillators With Nonlinear Filters

Jimmi H. Talla Mbé, Juliette S. D. Kamaha, *Student Member, IEEE*, Yanne K. Chembo, *Senior Member, IEEE*, and Paul Woafo

***Abstract*— We present a theoretical and experimental study of an optoelectronic oscillator featuring a cubic-nonlinear filter in the feedback loop. In this architecture, the nonlinearity introduces an additional timescale that leads to the emergence of complex behavior and multiscale dynamics, ultimately leading to chaos as the gain is increased. A complete bifurcation analysis is performed and successfully compared to experimental measurements. We expect this class of systems to emulate novel functionalities for analog signal processing based on time-delayed optoelectronic oscillators.**

***Index Terms*— Optoelectronic devices, nonlinear oscillators.**

I. Introduction

OPTOELECTRONIC oscillators have been in recent years the focus of active scientific research from the fundamental viewpoint [1]–[8], as well as from the technological perspective [9], [10]. These systems have found various applications such as ultra-stable microwave generation [11]–[19], chaos communications and systems [20]–[23], neuromorphic computing [24]–[26], sensing [27]–[29], signal processing [2], [30], [31], among other technological aims [32]–[34]. Recent developments have demonstrated the possibility to implement these oscillators on-chip [35]–[38].

The dynamics of OEOs strongly depends on the filtering properties of the feedback loop in the electric path. For example, the first-order low-pass filtering dynamics of the original Ikeda model is known today to be quite different from the one of OEOs featuring bandpass filters [9], [10], and even in the bandpass case, the dynamics of the OEO critically depends on the wideband [1] or narrowband [39] nature of the filter. In general, the electric branch is considered to be linear. However, nonlinear electrical response is a possibility and has already emerged as an ideal benchmark to investigate the complex dynamical states in OEOs, such as anti-monotonicity, spikes, pulse packages, and bursting [40], [41].

In this article, we consider an OEO where the electric branch features a cubic-nonlinear response, implemented using a nonlinear capacitor made of simple junction diodes. Nonlinear capacitors are important components in electronic systems, from both the fundamental and technological points of view. They are used in snubber circuits for power electronics, can operate at high frequencies. They can also be used to implement nonlinear resistors and inductances. For these reasons, they are commonly used as a source of nonlinearity in several physical systems [42]–[45]. In our oscillator, the nonlinear capacitor is used to introduce an additional integral term so that the resulting OEO model is presented as a novel extension of the broad bandpass Ikeda-like equation. The system can display attractors such as fixed points, limit-cycles, and chaos, and is therefore compatible with all the related applications. It is also possible to control mixed-mode oscillations which in return favored a quadrupled-frequency limit-cycle oscillations. Adding a nonlinear element in the electric branch is also a natural pathway to emulate complex coherent phenomena in coupled networks of OEOs (such as cluster synchronization, for example [46], [47])

The article is organized as follows. In the next section, we present the experimental system and propose a time-delayed model to investigate its complex dynamical behavior. The stability analysis of this equation is performed in Sec. III, while the nonlinear dynamics of the system is explored in Sec. IV. The last section concludes the article.

II. System and Model

The experimental set-up of the cubic-nonlinear optoelectronic oscillator (CN-OEO) is presented in Fig. 1a. The main elements are the following. A telecommunication continuous-wave laser diode with wavelength $\lambda_L \simeq 1550$ nm and power P_{in} seeds a Mach-Zehnder modulator (MZM) characterized by a radio-frequency (RF) and direct-current (DC) half-wave voltages $V_{\pi_{RF}} = 3.8$ V and $V_{\pi_{DC}} = 5$ V, respectively.

Manuscript received March 16, 2019; revised May 11, 2019; accepted May 27, 2019. Date of publication June 4, 2019; date of current version June 18, 2019. The work of J. H. Talla Mbé was supported by the African-German Network of Excellence in Science (AGNES). The work of Y. K. Chembo was supported by the University of Maryland. *(Corresponding author: Jimmi H. Talla Mbé.)*

J. H. Talla Mbé is with the Laboratory of Condensed Matter, Electronics and Signal Processing, Department of Physics, University of Dschang, Dschang, Cameroon, and also with the Laboratory of Modelling and Simulation in Engineering, Biomimetics and Prototypes, Department of Physics, University of Yaoundé I, Yaounde, Cameroon (e-mail: jhtallam@yahoo.fr).

J. S. D. Kamaha is with the Laboratory of Modelling and Simulation in Engineering, Biomimetics and Prototypes, Department of Physics, University of Yaoundé I, Yaounde, Cameroon.

Y. K. Chembo is with the Department of Electrical and Computer Engineering, Institute for Research in Electronics and Applied Physics, University of Maryland, College Park, MD 20742 USA.

P. Woafo is with the Laboratory of Modelling and Simulation in Engineering, Biomimetics and Prototypes, Department of Physics, University of Yaoundé I, Yaounde, Cameroon, and also with the Applied Physics Research Group, Vrije Universiteit Brussel, 1050 Brussels, Belgium.

Color versions of one or more of the figures in this paper are available online at http://ieeexplore.ieee.org.

Digital Object Identifier 10.1109/JQE.2019.2920694

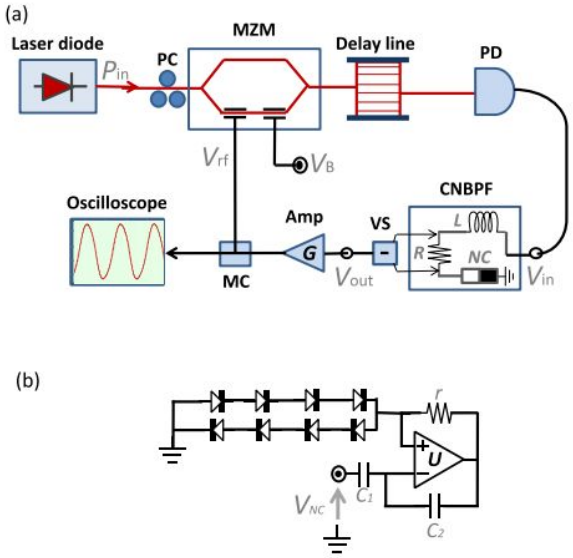

Fig. 1. (Color online) (a) Experimental set-up and (b) Nonlinear Capacitor (NC). V_B is the offset phase control voltage; PC: Polarization Controller; MZM: Mach-Zehnder Modulator; PD: Photodiode; CNBPF: Cubic-Nonlinear Band-Pass Filter; VS: Voltage Subtractor; Amp: RF amplifier; MC: Microwave Coupler.

The modulated light at the exit of the MZM is delayed by an optical delay line of delay T_D, and is then converted into an electrical voltage $V_{\rm in}$ by a photodiode with a conversion factor $S = 4.75$ V/mW. The voltage $V_{\rm in}$ is filtered with a cubic-nonlinear band-pass filter (CNBPF) made of a coil L, a resistor R and a nonlinear capacitor NC. The output voltage $V_{\rm out}$ of the CNBPF is the voltage difference probed across the resistor R: it is amplified using a radio-frequency amplifier with gain G before being re-injected into the RF electrode of the MZM. The inner structure of the nonlinear capacitor is depicted in Fig. 1b [42], [43]. It is implemented using an operational amplifier U (type LF356), two capacitors $C_{1,2}$, one resistor r, and a mixed assembly of eight simple junction diodes (type IN400X). These junction diodes are characterized by their thermal voltage $V_T = 25$ mV, inverse saturation current $I_s = 5$ μA, and number of junction diodes in series $n = 4$.

The application of Kirchhoff laws permits to evaluate the voltage across such a nonlinear capacitor which is a cubic-polynomial of the charge

$$q = \frac{1}{R}\int_0^t V_{\rm out}(s)\,ds \tag{1}$$

of the series capacitor, and yields the relationship [42]:

$$V_{\rm NC}(t) = \frac{1}{R}\left(\frac{1}{C_1} - \frac{nV_T}{2rI_sC_2}\right)\int_0^t V_{\rm out}(l)dl + \frac{nV_T}{48(rRI_sC_2)^3}\left(\int_0^t V_{\rm out}(s)\,ds\right)^3, \tag{2}$$

where t is the time. Then, the output voltage $V_{\rm out}(t)$ of the CNBPF is related to the input $V_{\rm in}(t)$ by:

$$V_{\rm in}(t) = \frac{L}{R}\frac{dV_{\rm out}(t)}{dt} + V_{\rm out}(t) + V_{\rm NC}(t). \tag{3}$$

Using Eqs. (2) and (3), and the usual closure relationships of broad bandpass optoelectronic oscillators [1], the system presented in Fig. 1a obeys the following integro-differential delayed equation:

$$x + \tau\frac{dx}{dt} + \frac{1}{\theta}\int_0^t x(s)\,ds + \eta\left(\int_0^t x(s)\,ds\right)^3 = \beta\{\cos^2[x(t-T_D)+\phi]\}, \tag{4}$$

where $x = \pi V_{\rm out}(t)/2V_{\pi\rm RF}$ is the dimensionless dynamical variable of the system. According to Eq. (4), the cubic-nonlinear band-pass filter is characterized by three time scales which are the high cut-off time τ, the low cut-off time θ, and the nonlinearity timescale $\sqrt[3]{1/\eta}$ that are explicitly defined via

$$\tau = L/R \tag{5}$$

$$\theta = R\left[(1/C_1) - (nV_T/2rI_sC_2)\right]^{-1} \tag{6}$$

$$\eta = nV_TV_{\pi\rm RF}^2/\left[12(rRI_sC_2)^3(\pi G)^2\right]. \tag{7}$$

Therefore, adding the delay T_D transforms our CN-OEO into a four-timescales OEO. The other parameters are the normalized loop-gain $\beta = \pi\kappa SGP_{\rm in}/2\ V_{\pi\rm RF}$ and the offset phase $\phi = \pi V_{\rm B}/2V_{\pi\rm DC}$. Throughout this article, except the tunable parameters G and $P_{\rm in}$, the values of other parameters are kept compatible with the experimental set-up. They are set to $L = 0.1$ mH, $R = 2.5$ kΩ, $r = 300$ Ω, $C_1 = 270$ pF, $C_2 = 9.15$ nF, and $T_D = 3.29$ μs.

In order to facilitate the dynamical analysis, it is preferable to recast Eq. (4) under the form of a flow of first-order coupled delay differential equations. For this purpose, we introduce the new variable

$$y = -\frac{1}{\theta}\int_0^t x(s)\,ds \tag{8}$$

and the dimensionless time $\nu = t/\theta$. Equation (4) is then transformed into a slow-fast system with x as the fast variable while y is the slow variable [4]:

$$\varepsilon\frac{dx}{d\nu} = -x + y + \rho y^3 + \beta\cos^2[x_\sigma + \phi] \tag{9}$$

$$\frac{dy}{d\nu} = -x. \tag{10}$$

The small quantity $\varepsilon = \tau/\theta = 9.7\times10^{-4}$ is the cut-off times ratio, $\sigma = T_D/\theta = 8\times10^{-2}$ represents the normalized delay so that $x_\sigma = x(\nu-\sigma)$ being the time-delayed variable. The parameter $\rho = \eta\theta^3 = 6.4\times10^4$ stands for the cubic-nonlinear parameter.

III. Stability Analysis

The first step for the analysis of the cubic-nonlinear OEO is the study of its stability. Indeed, the equilibrium point of the set of Eqs. (9) and (10) is (x_0, y_0), with $x_0 = 0$ and y_0 being the real root of the third-order polynomial

$$\rho y_0^3 + y_0 + \beta\cos^2\phi = 0, \tag{11}$$

which is nontrivial if β or ϕ is different from 0 or $\pi/2$ (mod $[2\pi]$), respectively. It is important to mention that y_0 is real and unique since ρ and β are positive quantities. The

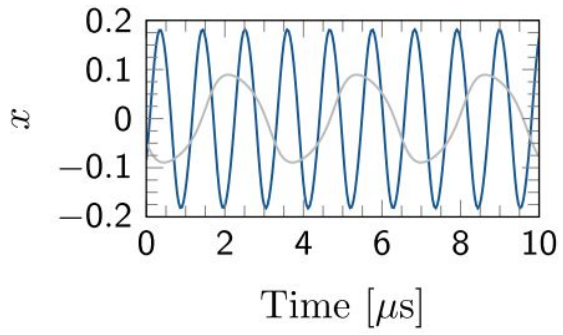

Fig. 2. (Color online) Timetraces of the amplitude of the cubic-nonlinear OEO (blue or black) versus the standard OEO (grey). $|\gamma| = 1.01$ and $\phi = -\pi/4$. A noticeable effect of the nonlinearity is to increase the frequency of the limit-cycle induced by the primary Hopf bifurcation.

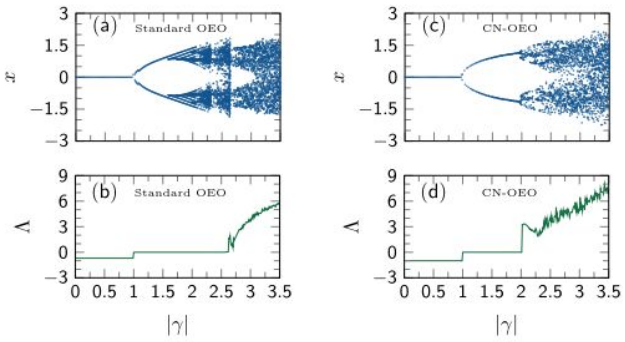

Fig. 3. (Color online) Bifurcation diagrams [(a) and (c)] depicting the routes to chaos and the largest Lyapunov exponents Λ [(b) and (d)]. (a) and (b): Standard OEO [i.e. without cubic-term in Eq. (9)]; the route to chaos is through breathers that are revealed by the multiple lines in the bifurcation diagram. (c) and (d): CN-OEO; here the route to chaos is directly through the Hopf bifurcation, and one can note that the multiple lines have disappeared.

stability of that equilibrium point can be investigated through the eigenvalues equation

$$\lambda^2 + \frac{1}{\varepsilon}\left(1 + \gamma\, e^{-\lambda\sigma}\right)\lambda + \frac{1}{\varepsilon}\left(1 + 3\rho y_0^2\right) = 0, \tag{12}$$

where $\gamma = \beta \sin(2\phi)$ is the effective normalized gain. Limit-cycle oscillation might occur through a Hopf bifurcation if the eigenvalues become pure imaginary values ($\lambda = \pm i\omega$), with ω being the frequency of the corresponding limit-cycle which satisfies the following transcendental equation

$$\varepsilon\omega^2 + \omega\, \tan(\omega\sigma) - \left(1 + 3\rho y_0^2\right) = 0, \tag{13}$$

while the effective normalized gain γ rather satisfies

$$\gamma\, \cos(\omega\sigma) = -1. \tag{14}$$

In the limit of small delay (small σ), the solutions of Eqs. (13) and (14) approximated as

$$\omega = \omega_{\text{sd}}\sqrt{1 + 3\rho y_0^2}, \tag{15}$$

$$\gamma = -1 + \frac{1}{2}\left(\frac{1 + 3\rho y_0^2}{\varepsilon + \sigma}\sigma^2\right). \tag{16}$$

Here,

$$\omega_{\text{sd}} = 1/\sqrt{\varepsilon + \sigma} \tag{17}$$

represents the frequency of the limit-cycle for the standard OEO, that is the one with a linear band-pass filter that does not feature the cubic-term in Eq. (4).

IV. Nonlinear Dynamics

From Eqs. (15) and (17), it clearly appears that the frequency of the limit-cycle oscillations of our CN-OEO is greater than the one displayed by a standard OEO for the same values of parameters. For instance, near the Hopf bifurcation, and taking the case of $|\gamma| = 1.01$ and $\phi = -\pi/4$, the frequency increasing factor $\sqrt{1 + 3\rho y_0^2} \sim 4$. Exactly, Fig. 2 validates the increase of the frequency of the CN-OEO, as well as its amplitude, comparatively to the standard OEO. That increase of frequency dwells for all values of the gain.

On the contrary, the threshold of the effective normalized gain is not considerably affected by the cubic-nonlinear term since $\gamma \simeq -1$ as witnessed by the bifurcation diagram of Fig. 3, showing the evolution of the amplitude as the effective normalized gain increases. Comparatively to the standard OEO, one can note that with the CN-OEO, only fixed point, limit-cycles, and chaos are preserved. Indeed, for the CN-OEO, when $|\gamma| < 1$, the fixed point $x_0 = 0$ dominates the dynamics of the system. From $|\gamma| = 1$, limit-cycle oscillations occur through a Hopf bifurcation and remain dominant for a large range of $|\gamma|$. When $|\gamma|$ is further increased, the limit-cycle disappears to give place to chaos. These transitions are emphasized by the corresponding largest Lyapunov exponent (Fig. 3) defined as

$$\Lambda = \lim_{t\to+\infty} \frac{1}{t} \ln\left[\frac{|\delta x(t)|}{|\delta x(t_0)|}\right], \tag{18}$$

with $\delta x(t)$ being a linear perturbation of the system [41]. The Lyapunov exponent Λ is known to be a positive quantity for chaotic behavior and negative or zero otherwise. It is shown from these figures that the bifurcation diagram and the largest Lyapunov exponent indicate the same window of dynamical behaviors for the chosen parameters.

The timetraces at different levels of the bifurcation diagram of the CN-OEO reveals that close to the Hopf bifurcation, the system displays harmonic oscillations (Figs. 4a and b). But, as $|\gamma|$ increases, harmonic oscillations are replaced by relaxation limit-cycles demonstrating the alternation between the slow and the fast transitions as the time evolves (Figs. 4c and d). For very large values of $|\gamma|$ timetraces of Figs. 4e and f illustrate the chaotic behavior of the system.

From the bifurcation diagrams (see Figs. 3a and c), it is noticeable that for the chosen parameters, mixed-mode oscillations also known as breathers are missing in our CN-OEO [1], [4]. The theory of breathers in OEO has been investigated through the geometric singular perturbation theory (see [48] and Refs. therein) and it is well known that the standard wide-band OEO displays breathers while following the route to chaos [4] (see Figs. 3a and b). To gain insight into their effect in our system, it is necessary to analyze the case where only the cubic-term is canceled in Eq. (4). The result presented in Fig. 5a testifies the presence of breathers which are manifested by damped oscillations around the attractive

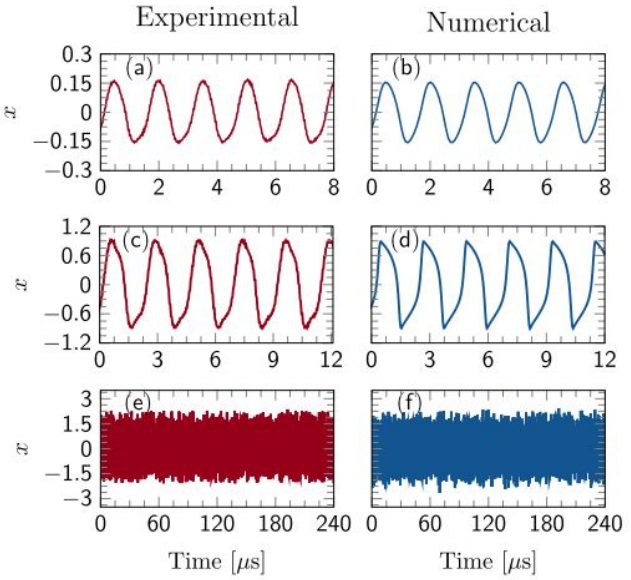

Fig. 4. (Color online) Experimental and numerical timetraces demonstrating the dynamical evolutions of the system as the gain increases with $\phi = -\pi/4$. From top to bottom, P_{in} is set to 6.51 mW, 7 mW, and 7.8 mW for the experimental timetraces, and β is set to 1.1, 1.9, and 3 for the theoretical ones.

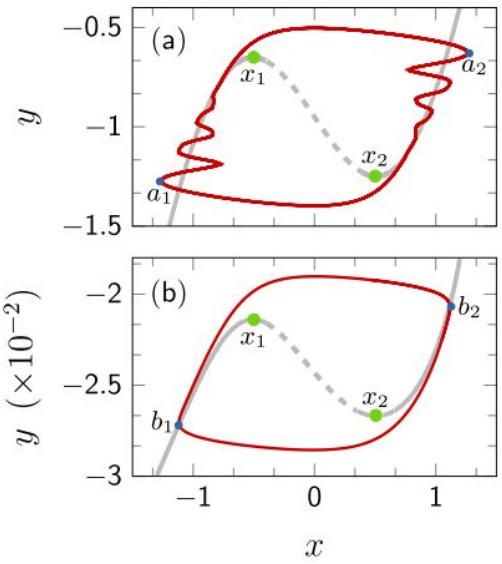

Fig. 5. (Color online) Projections in the $(x–y)$ plane of the trajectories (solid red (or black)) of: (a) the standard OEO and (b) the cubic-nonlinear OEO. The timetrace of Fig. 5b is given in Fig. 4d. The dashed and solid greys are the instable and stable branches of the invariant critical manifold, respectively. The invariant critical manifolds are plotted for $\sigma \to 0$ [4]. In both figures, $|\gamma| = 1.9$ and $\phi = -\pi/4$.

branches of the invariant critical manifold of the system, while they do not occur when the cubic-term is considered (Fig. 5b).

Indeed, the invariant critical manifolds are those static S-shaped curves of Figs. 5a and b defined in the $(x–y)$ plane by setting $\varepsilon dx/dv = 0$ in Eq. (9); That is:

$$\rho y^3 + y = x - \beta\{\cos^2[x_\sigma + \phi]\}. \tag{19}$$

Each invariant critical manifold is characterized by two fold points x_1 and x_2 which are solutions of $dy/dx = 0$, yielding

$$x_1 = -\frac{\pi}{2} + \frac{1}{2}\arcsin\left(\frac{1}{\beta}\right) - \phi, \tag{20}$$

$$x_2 = -\frac{1}{2}\arcsin\left(\frac{1}{\beta}\right) - \phi. \tag{21}$$

These critical points are marked with large dots and subdivide each invariant critical manifold into three branches, two of which are attractive (solid lines) and one is repulsive (dotted line) (see Fig. 5).

The slow-fast oscillations recorded in OEO result from alternate passages of its trajectory from one attractive branch to another and is characterized by a typical acceleration when this trajectory enters the zone of the repulsive branch. Indeed, a point of the trajectory taken near the fold point is accelerated by the repulsive branch towards the other attractive branch which is not attached to that fold point. The influence of the repulsive branch on the trajectory ceases when the "speed" reaches approaches zero $(dx/dv \to 0)$. In the phase plane, this translates to $dx/dy = 0$ with $\sigma \neq 0$, and corresponds to the points a_1 and a_2 of Fig. 5a, and b_1 and b_2 of Fig. 5b. We refer to them as the first notches, and the position of these first notches is crucial for the appearance of breathers. If the first notch (for example a_1) is quite far from the attractive branch, the attraction imposed by the branch on the trajectory is manifested through damped oscillations, which give rise to other notches (see Fig. 5a). In the time domain, this phenomenology is known as breathers. On the contrary, if the first notch (for example b_1) is located very close to the attractive branch, then the trajectory asymptotically converges to this branch while evolving towards the fold static point (for example x_1) where the acceleration of the repulsive branch takes the relay, and the cycle starts again. In that case, the system will not display breathers, and in this regard, the dynamics of this system significantly differs from the multiscale oscillations that can be observed in other architectures of OEOs (see for example [1], [49]–[51]).

V. Conclusion

In conclusion, we have demonstrated an OEO with a cubic-nonlinear electrical part. The limit-cycles generated with the device are of higher frequency and amplitude compared to the standard OEO. Our system can be operated either in narrow-band or wide-band configuration. It can display or not breathers by tuning some parameters for applications where they have to be either enhanced or avoided. This result shows that our CN-OEO is more versatile than the standard one. Our work also offers a more general overview of the origin of breathers in the wide-band OEO. We found that that their appearance depends on how far the first notch is from an attractive branch of the invariant critical manifold. Further investigations will explore concrete applications of these CN-OEOs in the context of information processing.

References

[1] Y. C. Kouomou, P. Colet, L. Larger, and N. Gastaud, "Chaotic breathers in delayed electro-optical systems," *Phys. Rev. Lett.*, vol. 95, Nov. 2005, Art. no. 203903.

[2] B. Romeira, J. Javaloyes, J. M. L. Figueiredo, C. N. Ironside, H. I. Cantu, and A. E. Kelly, "Delayed feedback dynamics of Liénard-type resonant tunneling-photo-detector optoelectronic oscillators," *IEEE J. Quantum Electron.*, vol. 49, no. 1, pp. 31–42, Jan. 2013.

[3] G. R. G. Chengui *et al.*, "Theoretical and experimental study of slow-scale Hopf limit-cycles in laser-based wideband optoelectronic oscillators," *J. Opt. Soc. Amer. B, Opt. Phys.*, vol. 31, no. 10, pp. 2310–2316, 2014.

[4] J. H. T. Mbé *et al.*, "Mixed-mode oscillations in slow-fast delayed optoelectronic systems," *Phys. Rev. E, Stat. Phys. Plasmas Fluids Relat. Interdiscip. Top.*, vol. 91, Jan. 2015, Art. no. 012902.

[5] A. M. Hagerstrom, T. E. Murphy, and R. Roy, "Harvesting entropy and quantifying the transition from noise to chaos in a photon-counting feedback loop," *Proc. Nat. Acad. Sci. USA*, vol. 112, no. 30, pp. 9258–9263, 2015.

[6] P. Munnelly *et al.*, "On-chip optoelectronic feedback in a micropillar laser-detector assembly," *Optica*, vol. 4, no. 3, pp. 303–306, 2017.

[7] J. D. Hart, Y. Zhang, R. Roy, and A. E. Motter, "Topological control of synchronization patterns: Trading symmetry for stability," *Phys. Rev. Lett.*, vol. 122, Feb. 2019, Art. no. 058301.

[8] J. H. T. Mbé, P. Woafo, and Y. K. Chembo, "A normal form method for the determination of oscillations characteristics near the primary Hopf bifurcation in bandpass optoelectronic oscillators: Theory and experiment," *Chaos*, vol. 29, Feb. 2019, Art. no. 033104.

[9] T. E. Murphy *et al.*, "Complex dynamics and synchronization of delayed-feedback nonlinear oscillators," *Philos. Trans. Roy. Soc. A, Math. Phys. Eng. Sci.*, vol. 368, pp. 343–366, Jan. 2010.

[10] L. Larger, "Complexity in electro-optic delay dynamics: Modelling, design and applications," *Philos. Trans. Roy. Soc. A, Math. Phys. Eng. Sci.*, vol. 371, Sep. 2013, Art. no. 20120464.

[11] X. S. Yao and L. Maleki, "High frequency optical subcarrier generator," *Electron. Lett.*, vol. 30, no. 18, pp. 1525–1526, 1994.

[12] X. S. Yao and L. Maleki, "Optoelectronic microwave oscillator," *J. Opt. Soc. Amer. B, Opt. Phys.*, vol. 13, no. 8, pp. 1725–1735, 1996.

[13] O. Okusaga *et al.*, "Spurious mode reduction in dual injection-locked optoelectronic oscillators," *Opt. Express*, vol. 19, no. 7, pp. 5839–5854, 2011.

[14] O. Okusaga, J. P. Cahill, A. Docherty, C. R. Menyuk, W. Zhou, and G. M. Carter, "Suppression of Rayleigh-scattering-induced noise in OEOs," *Opt. Express*, vol. 21, no. 19, pp. 22255–22262, 2013.

[15] R. M. Nguimdo, Y. K. Chembo, P. Colet, and L. Larger, "On the phase noise performance of nonlinear double-loop optoelectronic microwave oscillators," *IEEE J. Quantum Electron.*, vol. 48, no. 11, pp. 1415–1423, Nov. 2012.

[16] Y. Zhang, D. Hou, and J. Zhao, "Long-term frequency stabilization of an optoelectronic oscillator using phase-locked loop," *J. Lightw. Technol.*, vol. 32, no. 13, pp. 2408–2414, Jul. 1, 2014.

[17] K. Saleh, G. Lin, and Y. K. Chembo, "Effect of laser coupling and active stabilization on the phase noise performance of optoelectronic microwave oscillators based on whispering-gallery-mode resonators," *IEEE Photon. J.*, vol. 7, no. 1, Feb. 2015, Art. no. 5500111.

[18] O. Lelièvre *et al.*, "A model for designing ultralow noise single- and dual-loop 10-GHz optoelectronic oscillators," *J. Lightw. Technol.*, vol. 35, no. 20, pp. 4366–4374, Oct. 15, 2017.

[19] A. Ly, V. Auroux, R. Khayatzadeh, N. Gutierrez, A. Fernandez, and O. Llopis, "Highly spectrally pure 90-GHz signal synthesis using a coupled optoelectronic oscillator," *IEEE Photon. Technol. Lett.*, vol. 30, no. 14, pp. 1313–1316, Jul. 15, 2018.

[20] A. Argyris *et al.*, "Chaos-based communications at high bit rates using commercial fibre-optic links," *Nature*, vol. 438, pp. 343–346, Nov. 2005.

[21] A. B. Cohen, B. Ravoori, T. E. Murphy, and R. Roy, "Using synchronization for prediction of high-dimensional chaotic dynamics," *Phys. Rev. Lett.*, vol. 101, Oct. 2008, Art. no. 154102.

[22] R. M. Nguimdo, R. Lavrov, P. Colet, M. Jacquot, Y. K. Chembo, and L. Larger, "Effect of fiber dispersion on broadband chaos communications implemented by electro-optic nonlinear delay phase dynamics," *J. Lightw. Technol.*, vol. 28, no. 18, pp. 2688–2696, Sep. 15, 2010.

[23] J. Ai, L. Wang, and J. Wang, "Secure communications of CAP-4 and OOK signals over MMF based on electro-optic chaos," *Opt. Lett.*, vol. 42, no. 18, pp. 3662–3665, 2017.

[24] Y. Paquot *et al.*, "Optoelectronic reservoir computing," *Sci. Rep.*, vol. 2, Feb. 2012, Art. no. 287.

[25] M. C. Soriano *et al.*, "Optoelectronic reservoir computing: Tackling noise-induced performance degradation," *Opt. Express*, vol. 21, no. 1, pp. 12–20, 2013.

[26] L. Larger, A. Baylón-Fuentes, R. Martinenghi, V. S. Udaltsov, Y. K. Chembo, and M. Jacquot, "High-speed photonic reservoir computing using a time-delay-based architecture: Million words per second classification," *Phys. Rev. X*, vol. 7, Feb. 2017, Art. no. 011015.

[27] X. Zou *et al.*, "Optoelectronic oscillators (OEOs) to sensing, measurement, and detection," *IEEE J. Quantum Electron.*, vol. 52, no. 1, Jan. 2016, Art. no. 0601116.

[28] J. Yao, "Optoelectronic oscillators for high speed and high resolution optical sensing," *J. Lightw. Technol.*, vol. 35, no. 16, pp. 3489–3497, Aug. 15, 2017.

[29] B. Wu *et al.*, "Magnetic field sensor based on a dual-frequency optoelectronic oscillator using cascaded magnetostrictive alloy-fiber Bragg grating-Fabry Perot and fiber Bragg grating-Fabry Perot filters," *Opt. Express*, vol. 26, no. 21, pp. 27628–27638, 2018.

[30] D. Zhu, S. Liu, D. Ben, and S. Pan, "Frequency-quadrupling optoelectronic oscillator for multichannel upconversion," *IEEE Photon. Technol. Lett.*, vol. 25, no. 5, pp. 426–429, Mar. 1, 2013.

[31] P. Zhou, F. Zhang, and S. Pan, "Generation of linear frequency-modulated waveforms by a frequency-sweeping optoelectronic oscillator," *J. Lightw. Technol.*, vol. 36, no. 18, pp. 3927–3934, Sep. 15, 2018.

[32] C. Y. Chang *et al.*, "A multi-GHz chaotic optoelectronic oscillator based on laser terminal voltage," *Appl. Phys. Lett.*, vol. 108, no. 19, 2016, Art. no. 191109.

[33] L. Huang *et al.*, "Stable and compact dual-loop optoelectronic oscillator using self-polarization-stabilization technique and multicore fiber," *J. Lightw. Technol.*, vol. 36, no. 22, pp. 5196–5202, Nov. 15, 2018.

[34] M. Shi, L. Yi, W. Wei, and W. Hu, "Generation and phase noise analysis of a wide optoelectronic oscillator with ultra-high resolution based on stimulated Brillouin scattering," *Opt. Express*, vol. 26, no. 13, pp. 16113–16124, 2018.

[35] L. Maleki, "The optoelectronic oscillator," *Nature Photon.*, vol. 5, no. 12, pp. 728–730, 2011.

[36] P. Zhou, S. Pan, D. Zhu, R. Guo, F. Zhang, and Y. Zhao, "A compact optoelectronic oscillator based on an electroabsorption modulated laser," *IEEE Photon. Technol. Lett.*, vol. 26, no. 1, pp. 86–88, Jan. 1, 2014.

[37] G. R. G. Chengui, P. Woafo, and Y. K. Chembo, "The simplest laser-based optoelectronic oscillator: An experimental and theoretical study," *J. Lightw. Technol.*, vol. 34, no. 3, pp. 873–878, Feb. 1, 2016.

[38] J. Tang *et al.*, "Integrated optoelectronic oscillator," *Opt. Express*, vol. 26, no. 9, pp. 12257–12265, 2018.

[39] Y. K. Chembo, L. Larger, R. Bendoula, and P. Colet, "Effects of gain and bandwidth on the multimode behavior of optoelectronic microwave oscillators," *Opt. Express*, vol. 16, no. 12, pp. 9067–9072, 2008.

[40] A. F. Talla, R. Martinenghi, P. Woafo, and Y. K. Chembo, "Breather and pulse-package dynamics in multinonlinear electrooptical systems with delayed feedback," *IEEE Photon. J.*, vol. 8, no. 4, Aug. 2016, Art. no. 7803608.

[41] G. R. G. Chengui, J. H. T. Mbé, A. F. Talla, P. Woafo, and Y. K. Chembo, "Dynamics of optoelectronic oscillators with electronic and laser nonlinearities," *IEEE J. Quantum Electron.*, vol. 54, no. 1, Feb. 2018, Art. no. 5000207.

[42] H. Fatoorehchi, H. Abolghasemi, and R. Zarghami, "Analytical approximate solutions for a general nonlinear resistor–nonlinear capacitor circuit model," *Appl. Math. Model.*, vol. 39, no. 19, pp. 6021–6031, 2015.

[43] C. A. K. Kwuimy and P. Woafo, "Experimental realization and simulations a self-sustained macro electromechanical system," *Mech. Res. Commun.*, vol. 37, pp. 106–110, Jan. 2010.

[44] G. Fregien and J. D. Van Wyk, "Nonlinear capacitors in snubber circuits for GTO thyristors," *IEEE Trans. Power Electron.*, vol. 7, no. 2, pp. 425–429, Apr. 1992.

[45] C. Hayashi, *Nonlinear Oscillations in Physical Systems*. New York, NY, USA: McGraw-Hill, 1964.

[46] Y. C. Kouomou and P. Woafo, "Transitions from spatiotemporal chaos to cluster and complete synchronization states in a shift-invariant set of coupled nonlinear oscillators," *Phys. Rev. E, Stat. Phys. Plasmas Fluids Relat. Interdiscip. Top.*, vol. 67, Apr. 2003, Art. no. 046205.

[47] Y. C. Kouomou and P. Woafo, "Cluster synchronization in coupled chaotic semiconductor lasers and application to switching in chaos-secured communication networks," *Opt. Commun.*, vol. 223, nos. 4–6, pp. 283–293, Aug. 2003.

[48] M. Desroches, J. Guckenheimer, B. Krauskopf, C. Kuehn, H. M. Osinga, and M. Wechselberger, "Mixed-mode oscillations with multiple time scales," *SIAM Rev.*, vol. 54, no. 2, pp. 211–288, 2012.

[49] L. Weicker, T. Erneux, M. Jacquot, Y. Chembo, and L. Larger, "Crenelated fast oscillatory outputs of a two-delay electro-optic oscillator," *Phys. Rev. E, Stat. Phys. Plasmas Fluids Relat. Interdiscip. Top.*, vol. 85, no. 2, 2012, Art. no. 026206.
[50] L. Weicker *et al.*, "Strongly asymmetric square waves in a time-delayed system," *Phys. Rev. E, Stat. Phys. Plasmas Fluids Relat. Interdiscip. Top.*, vol. 86, Nov. 2012, Art. no. 055201.
[51] L. Weicker *et al.*, "Slow–fast dynamics of a time-delayed electro-optic oscillator," *Philos. Trans. Roy. Soc. A, Math. Phys. Eng. Sci.*, vol. 371, Sep. 2013, Art. no. 20120459.

Jimmi H. Talla Mbé received the Ph.D. degree in physics from the University of Yaoundé I, Cameroon, in 2012. In 2012, he was a Post-Doctoral Fellow with the Franche-Comté Electronique, Mécanique, Thermique et Optique—Sciences et Technologies (FEMTO-ST) Institute, Besançon, France. He is currently Assistant Professor with the University of Dschang, Dschang, Cameroon. He is also with the University of Yaoundé I, Yaoundé, Cameroon. His research interests include nonlinear dynamics, optoelectronics, photonics, optomechanics, and optical metrology. He is a fellow of the Cameroon Academy of Young Scientists (CAYS). He received the African-German Network of Excellence in Science (AGNES) for Young Scientists in 2012. He is an Advisor of the IEEE-Cameroon Student Chapter.

Juliette S. D. Kamaha received the M.S. degree in physics from the University of Yaoundé I, Cameroon, in 2016, where she is currently pursuing the Ph.D. degree. She is investigating the multiscale nonlinear dynamics of novel architectures of optoelectronic oscillators and their applications.

Yanne K. Chembo (SM'12) received the Ph.D. degree in nonlinear dynamics from the University of Yaoundé I, Cameroon, in 2005, and the Ph.D. degree in photonics from the University of the Balearic Islands, Palma de Mallorca, Spain, in 2006. In 2007 and 2008, he was a Post-Doctoral Fellow with the FEMTO-ST Institute, Besançon, France. In 2009, he was a NASA Postdoctoral Program (NPP) Fellow with the Quantum Science and Technology Group, Jet Propulsion Laboratory, Caltech, Pasadena, USA. From 2010 to 2016, he has been a Research Scientist with the Centre National de la Recherche Scientifique (CNRS), France, with affiliation to the FEMTO-ST Institute, where he founded and led the Microwave Photonics Group. In 2017, he joined the International GeorgiaTech-CNRS Research Laboratory, Atlanta, USA, where he became the CNRS Research Director in 2018. In 2019, he joined the Institute for Research in Electronics and Applied Physics (IREAP), University of Maryland, where he is heading the Photonic Systems Laboratory. He has coauthored more than 90 articles in refereed international journals, and more than 60 international refereed proceedings. His research interests involve microwave photonics, optoelectronics, and the applied nonlinear, stochastic, and quantum dynamics of complex photonic systems. He is a fellow of SPIE. He is an Associate Editor for the OSA journal *Optics Express*.

Paul Woafo received the Ph.D. degree in physics from the University of Yaoundé in 1992, and the Doctorat d'Etat degree in physics in 1997. He is currently a Full Professor with the University of Yaoundé I, and heads the Laboratory of Modelling and Simulation in Engineering, Biomimetics and Prototypes (LAMSEBP). He is also an External Member of the Applied Physics Group, Vrije Universiteit Brussel, Belgium. He is also the Dean of the College of Mathematics and Physical Sciences, Cameroon Academy of Sciences. He is also a Senior Associate of the International Center for Theoretical Physics. He has published more than 200 refereed articles in international journals. His research interests involve the nonlinear and stochastic dynamics in optoelectronics, electromechanics and biological systems. He is a Founding Member and the Former President of the Cameroonian Physical Society (CPS). He was a member of the International Union of Pure and Applied Physics (IUPAP) Commission for Statistical Physics (C3), and received the TWAS Prize for Young Scientists in 2004. He is a Georg Forster Fellow of the Humboldt Foundation, Germany. He is the Vice President of the African Physical Society (AfPS).